Molecular Beam Epitaxy Synthesis and Nanoscale Characterization of Topological Insulator Thin Films and Their Interface With High-temperature Superconductors

Bryan Rachmilowitz

July 6, 2022

A Dissertation Submitted
To
The Department of Physics
In Partial Fulfillment of the Requirements
For the Degree of
Doctor of Philosophy
In the Subject of
Physics

Boston College
Morrissey College of Arts and Sciences
Graduate School

© Copyright 2022 - Bryan Rachmilowitz

Molecular Beam Epitaxy Synthesis and Nanoscale Characterization of Topological Insulator Thin Films and Their Interface With High-temperature Superconductors

Bryan Rachmilowitz

Thesis Advisor: Ilija Zeljkovic, Ph.D.

Abstract

The discovery of topological phases has ushered in an era of new materials with exotic electronic properties; one particular area of excitement is realizing and studying topologically superconducting systems. These topological superconductors are theorized to host exotic excitations that can be applied towards making fault tolerant quantum computations. One way to achieve this is depositing thin films of topological insulators onto superconducting substrates. Molecular beam epitaxy offers precise control for fabricating thin film heterostructures down to the single layer limits. In this thesis I will present my work on the synthesis of thin film topological insulators grown epitaxially on both an iron based superconductor $FeTe_{0.55}Se_{0.45}$ as well as a cuprate superconductor $Bi_2Sr_2CaCu_2O_{x+8}$. Additionally I will cover the scanning tunneling microscopy/spectroscopy characterization of the emergent phenomena on the surface as well as at the interface of these heterostructures. This work presents a viable platform for exploring the emergence of superconductivity in topologically insulating materials, as well as demonstrates the importance of a clean interface.

Table of Contents

List of Figures

Dedicated to my niece and nephews Amelia, Isaac and Alec

Acknowledgements

It's been almost exactly seven years since I joined Boston College as a graduate student and though I've worked very hard none of this dissertation would be possible if it had not been for the support of so many people that have been in my life. To start, I would like to thank my advisor Ilija Zeljkovic. I cannot stress enough how exceptional of an advisor and person he is. I feel so lucky that I was able to work with someone who not only is an exceptional researcher but also someone who is kind and compassionate. It's not an easy task to balance both graduate school and life, but having an advisor who asks "How are you?" before "How's the experiment?" made it so much better. The next person I would like to acknowledge is Paul Dee, not only for teaching me how to machine but also for all the early morning therapy sessions. Paul will always be a true friend and I am incredibly grateful for his support and encouragement. I would like to also thank all the members of the Zeljkovic lab, in particular He Zhao and Zheng Ren for working so well with me during the early years of joining the lab. I would also like to thank the junior members of the lab Alexander LaFleur, Hong Li and Shrinkhala Sharma for helping foster such a friendly and collaborative environment and Wilber Alfara Castro for being such a fantastic mentee. I also owe my gratitude to my thesis committee members Professors Ken Burch, Fazel Tafti and Ying Ran for their patience and willingness to be on my committee. I would like to also thank the office staff of the department Jane Carter, Nancy Chevry and Scott Bortolotto as I know for a fact that other departments don't have such awesome people in these roles. Lastly I would like to thank my graduate student colleagues, in particular Faranak Bahrami for showing me what it's like to have a sister.

Besides all the wonderful people at Boston College, I'd like to also acknowledge my family and friends. Thank you to my mother and father Cindy and Norman Rachmilowitz for all their love and support throughout graduate school and for always encouraging me to do what I enjoy. Thank you to my brother Michael and my sister in-law Ikumi for making me an uncle. Amelia, Isaac and Alec provided so much needed joy over these past few years and I'm looking forward to seeing them grow up. I would also like to thank my grandparents Barbara and Ken Schwarz for their love and support and for all the fun political conversations we get to have. Last but most certainly not least I would like to thank my very good friend Graham Moore and his mother Joanne Cipolla Moore. Thank you Graham for being a true friend who stood the test of time, I am looking forward to the many collaborations we are bound to work on in life. Lastly thank you so much Joanne for being a mother figure for me here in Boston, I don't think there's a more caring soul on this planet and Earth is lucky to have you.

Chapter 1 - Topological Materials

1.1 Introduction and Scope

Condensed matter physics aims to understand the fundamental laws that govern the behavior of solids and liquids. One of the most intriguing phenomena in condensed matter is when a material undergoes a phase transition. When most people think of a phase solids, liquids and gasses come to mind as well as plasma in some instances. In actuality, there are a plethora of rich and exotic phases for example superconductors and all the various magnetic orderings. For much of this century these phase transitions were understood through the lens of broken symmetry developed by Landau [1, 2] who built off mathematician Emmy Neother's famous theorem that related conservation laws to an associated continuous symmetry [3]. A simple example of a symmetry breaking phase transition is when a liquid freezes into a solid crystal. In the liquid phase the particles can exist anywhere inside the container that confines it, therefore the liquid has continuous translational symmetry. When the liquid freezes the atoms take on discrete lattice positions, and thus the continuous translational symmetry is broken during this phase transition. This framework has been used to describe many of the more complex phase transitions in condensed matter as well, such as the superconducting phase transition. When a material cools down enough to form Cooper pairs and becomes superconducting, the electromagnetic gauge symmetry is broken. This broken symmetry framework dominated our understanding of most phase transitions until Klaus von Klitzing's electrical transport measurements in 1980 sparked a revolution in our understanding of phase transitions. Von Klitzing applied a magnetic field to a MOSFET device at low temperature and measured its Hall resistance. He found that it was surprisingly quantized in integer multiples of $\frac{\hbar}{e}$ where $\hbar$ is Planck's constant and e is the elementary charge of an electron [4]. The precise quantization of the Hall resistance alone was a striking enough, but von Klitzing also noted how robust this quantum Hall all state was. He noticed how the geometry of the device did not affect this quantization [4]. Von Klitzing had discovered the integer quantum Hall effect. For specific values of the magnetic field different quantum Hall states were observed, but there was not any obvious broken symmetry that distinguished these quantum Hall phases from each

other. This was one of the first experimental results that showed that the broken symmetry framework was incomplete and there was more that needed to be understood. Around the same time theoretical physicists were applying the mathematical concept of topology to 2-D superconducting systems [5]. The mathematical field of topology studies geometric properties that remain unaffected by smooth and continues deformations. A common example of this is that a smooth ball and a donut are topologically different because you cannot change one into the other unless you pierce a hole in it. While a donut and a coffee cup are the same because you can smoothly deform them back and forth (Figure 1.1.1).

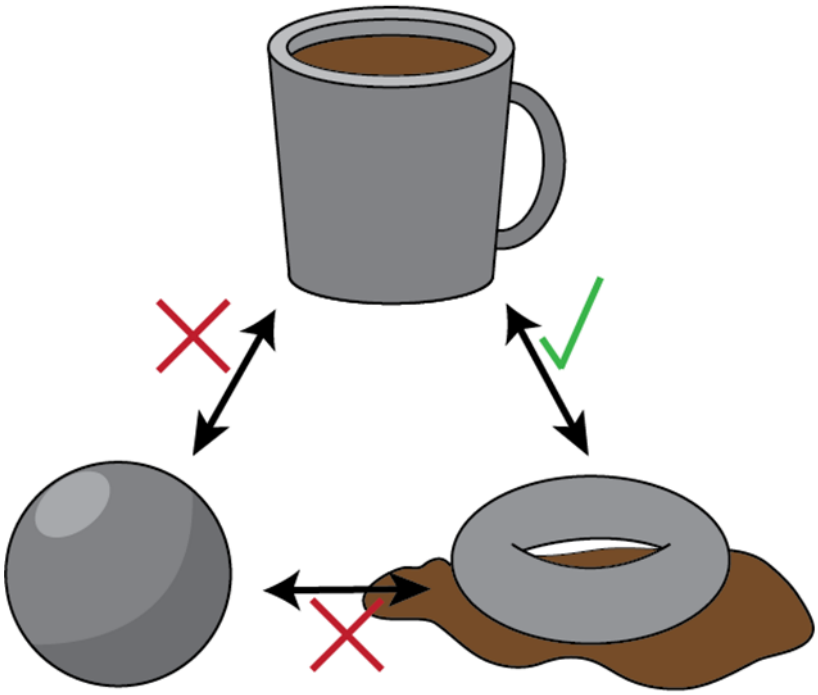

Figure 1.1.1: A common schematic showing that a coffee cup and donut have the same topology while a donut and smooth sphere do not.

Despite the coffee cup losing its ability to hold liquid the amount of holes remains unchanged and therefore we would say the two objects are topologically equivalent (Figure 1.1.1). Though the mathematical field of topology can trace its roots back to the end of the nineteenth century it remained largely out of the collective physics conscience until the 1970s and 1980s. In the early 1970s Michael Kosterlitz and David Thouless along with Soviet physicist Vadim Berezinskii, were using topology to model superconducting phase transitions [6, 5]. Only a couple years after von Klitzing's experimental discovery of the integer quantum Hall effect David Thouless in 1982 was able to describe his observation using topology similar to his earlier work. He was able to theoretically describe the quantization of the

Hall conductance observed in von Klitzing's transport measurements, and showed that the different quantum Hall states had different topology [7]. This sparked a revolution in discoveries and predictions and topological phase transitions were at the center. One of these such predictions came from Duncan Haldane in 1988 where he showed that it was theoretically possible to have a quantum Hall state in some time-reversal symmetry breaking systems in the absence of a magnetic field [8]. Though it was theoretically shown it was not apparent what sort of system could exhibit this behavior. It took another couple of decades until 2006 when Bernevig and Zheng theorizes that in systems with strong spin orbit coupling and strain you should be able measure a quantum Hall state [9]. Most importantly they predicted it should be observable using strained zinc-blend semiconductors [9]. Only one year later it was experimentally realized in a thin layer of $HgTe$ sandwiched between two $CdTe$ layers [10]. This marked the discovery of a true topological insulator (TI), a system that has conducting edges but an insulating bulk in the absence of a magnetic field. This sparked several theoretical and experimental discoveries most notably the use of alloying to make the first 3D TI [11] and the discovery of the first single crystal Z_2 TI [12, 13, 14]. Other topological insulator phases were also discovered such as the topological crystalline insulator (TCI) whose surface states are protected by the symmetry of the lattice [15, 16]. Until fairly recently our understanding of phase transitions was missing a key a part, that being topology. It was clear how impactful the theoretical understanding of topological phase transitions was, rightfully earning Thouless, Kosterlitz and Haldane the 2016 Nobel prize in physics. I doubt von Klitzing could have predicted how impactful his simple transport measurements would become, and the multitude of experimental and theoretical discoveries that would follow as a result.

The 2010's have been filled with numerous predictions and discoveries of different materials that have topological properties. Most interesting and relevant to this dissertation was the prediction of Liang Fu and Charlie Kane. They theorized that when a topological insulator is brought in proximity to an s-wave superconductor, the superconducting proximity effect gives rise to $p_x + ip_y$ type superconductivity on the surface of the TI [17]. When a magnetic field is applied to this system, a new type of quasiparticle known as a Majorana bound state could emerge located in the core of magnetic vortices [17]. The discovery of the topological crystalline insulator birthed a similar theory that predicated superconducting TCIs could be a new type of topological superconductivity different than that of proximitized Z_2 TIs. These superconducting TCIs could host multiple Majorana bound states inside single vortex cores [18], as well hosting tunable Andreev bound states [19]. Efforts in achieving topological superconductivity through the use of the superconducting proximity effect has mostly employed the use of low-T_c superconductors such as $NbSe_2$ [20, 21, 22, 23, 24] and elemental ones [25, 26]. While the efforts to induce superconductivity with high-T_c superconductor $Bi_2Sr_2CaCu_2O_{8+x}$ has had conflicting results [27, 24, 28, 29].

This dissertation is focussed on my efforts to realize and study topological superconductivity, in a few different heterostructures using high-T_c superconducting substrates. Chapter 2 will introduce the two main experimental techniques used during my Ph.D., the first and foremost being molecular beam epitaxy and the second being scanning tunneling microscopy/spectroscopy. In chapter 3, I will introduce the laboratory equipment in Professor Ilija Zeljkovic's lab and how the sample substrate's studied in this dissertation were prepared. Chapter 4 will go over the use of an iron based superconductor for realizing topological superconductivity in both a TI Bi_2Te_3 and TCI $SnTe$. In chapter 5, I will cover my efforts to use $Bi_2Sr_2CaCu_2O_{8+x}$ to also induce superconductivity in TI Bi_2Te_3 and offer a reasonable explanation for the gap like features observed around the Fermi energy.

Chapter 2 - Experimental Techniques

2.1 Basic Principle of Molecular Beam Epitaxy

Molecular beam epitaxy (MBE) is a technique that allows one to synthesize single crystal thin films in a highly controllable fashion. Early work on MBE was done by German scientist Günther in 1958 [30] where he heated up elements inside a vacuum chamber until they became gaseous and condensed onto a substrate. The MBE process was further developed by Davey and Pankey who demonstrated the layer by layer growth mode for growing high quality $GaAs$ films [31]. Cho and Arthur developed what most closely resembles a modern MBE system utilizing an electron gun to monitor the film growth in real time [32]. The name molecular beam epitaxy is self-explanatory. The goal is to create beams of molecules that condense epitaxially which just means in a layer by layer growth. Figure 2.1.1 shows a diagram of the outside of an MBE chamber.

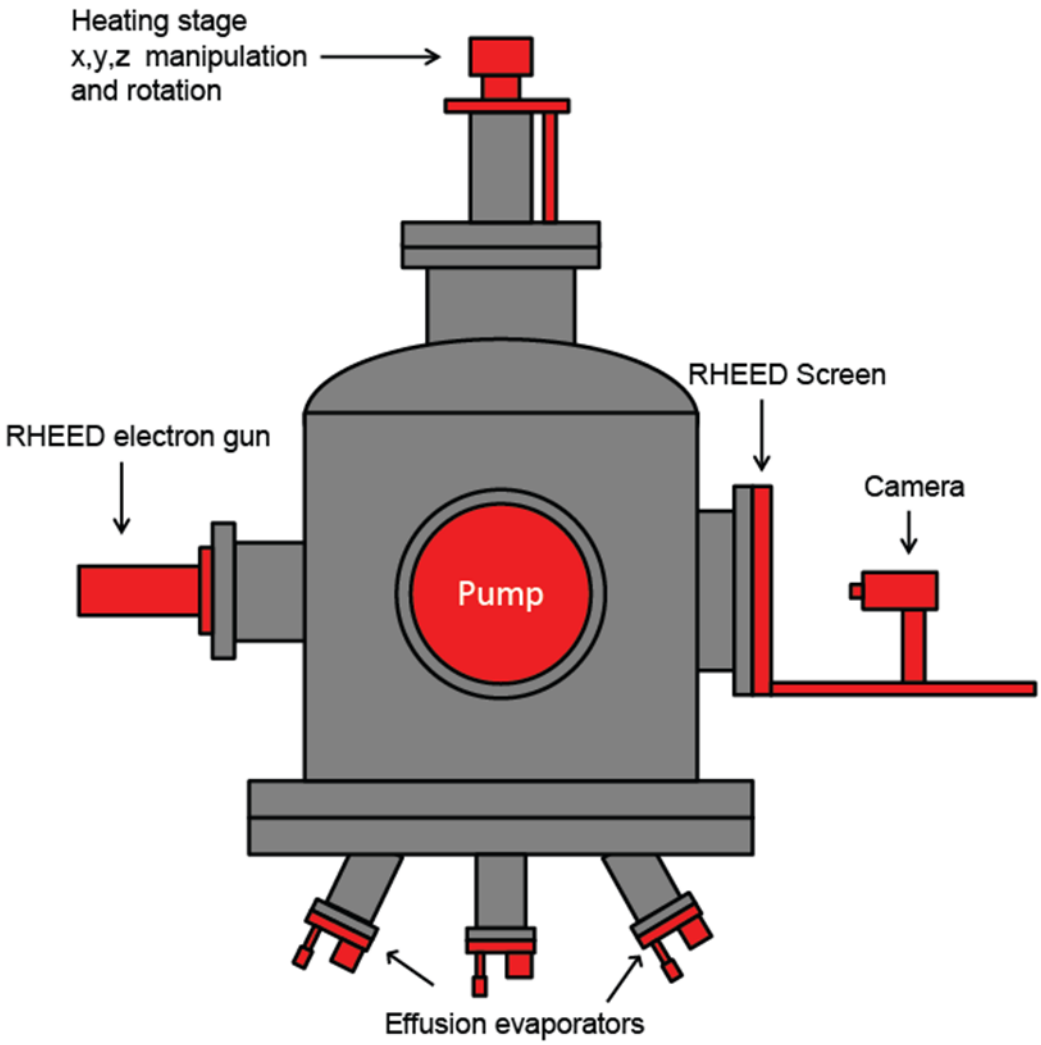

Figure 2.1.1: Cartoon diagram showing the various components that make up a molecular beam epitaxy system

An MBE system needs to technically only have three main parts to function. The first is some sort of pump, typically a turbo molecular pump that is backed by a rotary vane roughing pump, without this ultra-high vacuum conditions would not be possible. The second pinnacle part is the effusion cells. These are what heat up the materials one wishes to evaporate. The last part is the substrate heater, without this one could not tune the growth conditions to grow the desired films. Besides these an MBE is also typically equipt with a reflection high energy electron diffraction (RHEED) system, a quartz crystal growth monitor (not pictured) as well as a way to manipulate the position of the substrate heater and rotate it. Figure 2.1.2 gives a diagram of the inside of a typical MBE system.

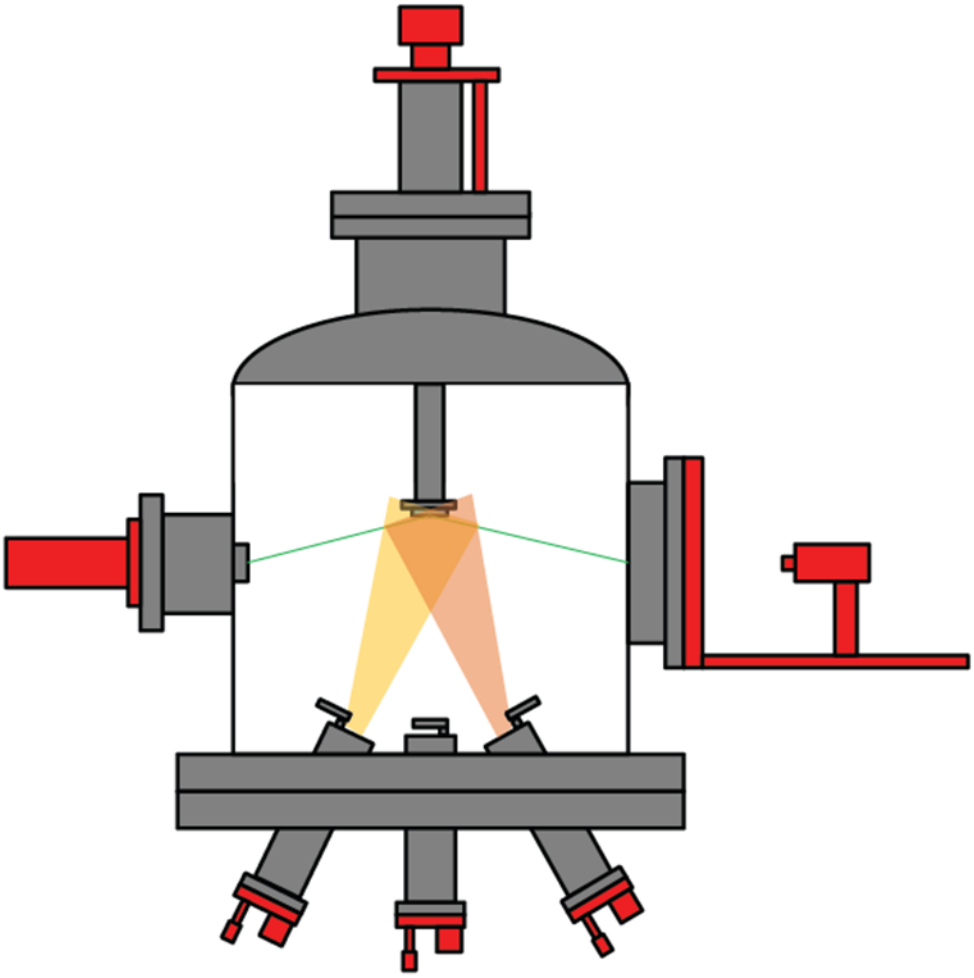

Figure 2.1.2: Cartoon diagram showing inside a typical MBE system and how the thermal evaporators, substrate heater and RHEED system are aligned with respect to each other

Inside the MBE the effusion cells are pointed directly at the substrate heater positioned above them. They have shutters that can be used to block the beams until one wants to start deposition. A RHEED system is used to monitor the growth in real time. It works by reflecting a high energy beam of electrons off the sample surface onto a florescent screen at a low angle. This resulting diffraction pattern is monitored in real time by a camera and viewed on a computer (Figure 2.1.3). Since electrons are charged they don't penetrate very far into the sample and thus the diffraction pattern comes from just the top most layers.

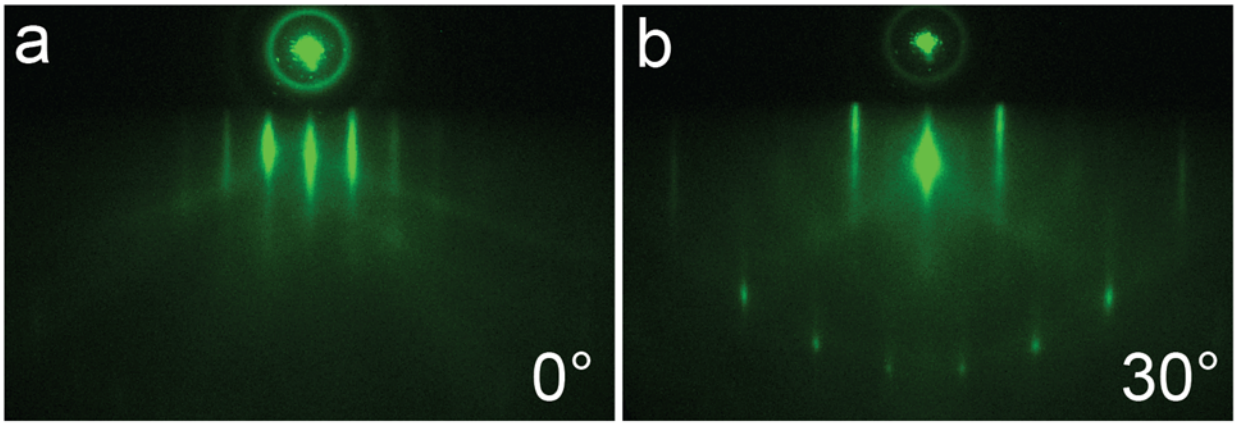

Figure 2.1.3: Example of RHEED images taken of a crystal with a hexagonal crystal lattice, showing the two high symmetry directions (a) 0° and (b) 30°.

When the electron beam is aligned with the direction of the crystal lattice a RHEED pattern comprised of streaks will appear. The distance between these streaks corresponds to the periodicity of the films lattice along that direction. This is best illustrated in the diagram below that shows the high symmetry directions for both a square and hexagonal lattice (Figure 2.1.4).

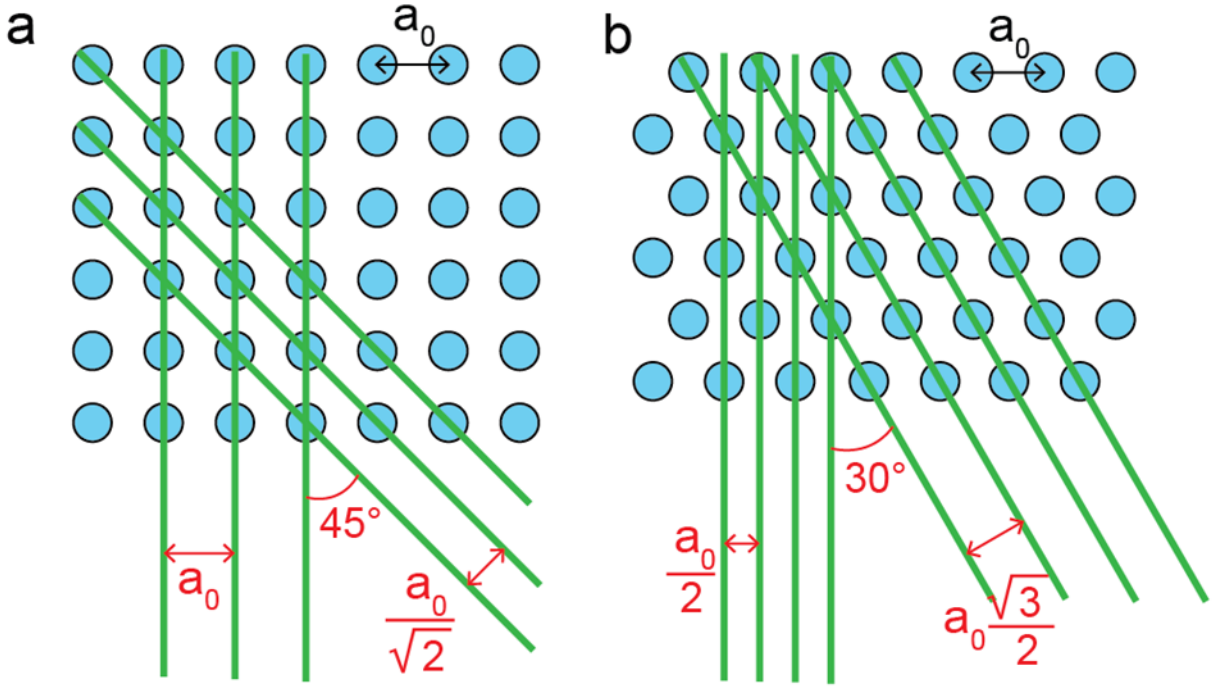

Figure 2.1.4: Diagram explaining what lattice spacings the high symmetry directions in RHEED correspond to (a) square lattices and (b) hexagonal lattices.

When the film has a cubic crystal structure and it grows in the 001 direction, the atoms are arranged in a square lattice on the surface (Figure 2.1.4 a). The two high symmetry directions are orientated 45° with respect to each other. One of the spacings corresponds to lattice constant while the other is half the body diagonal of the square lattice. In the case where one's surface has hexagonal symmetry (Figure 2.1.4 b) there are two high symmetry directions that are 30° apart, and are proportional by $\sqrt{3}$. The proportionality of these spacing can tell much about the crystal structure of the film one is growing.

2.2 Introduction to Scanning Tunneling Microscopy

While working at IBM's research facility in Zürich Switzerland in 1982 physicists Gerd Binnig and Heinrich Rohrer invented the scanning tunneling microscope earning them the 1986 Nobel prize in physics. Abbreviated STM colloquially, this technique exploits the phenomena of quantum tunneling to extract not only structural information on the atomic scale but electronic information as well [33]. Forty years after its invention the STM still remains one of the most useful experimental techniques today.

When two materials are brought within close proximity to one another but remain separated by a thin insulating layer there is a finite probability for electrons to tunnel across this barrier. In an STM the two materials being tunnelled between are the STM's tip and the material you are interested in studying. Vacuum, or in some cases air acts as the insulating barrier. The prototypical STM uses an atomically sharp metallic tip that sits inside a piezoelectric scanner tube. Figure 2.2.1 below illustrates the conventional STM's setup.

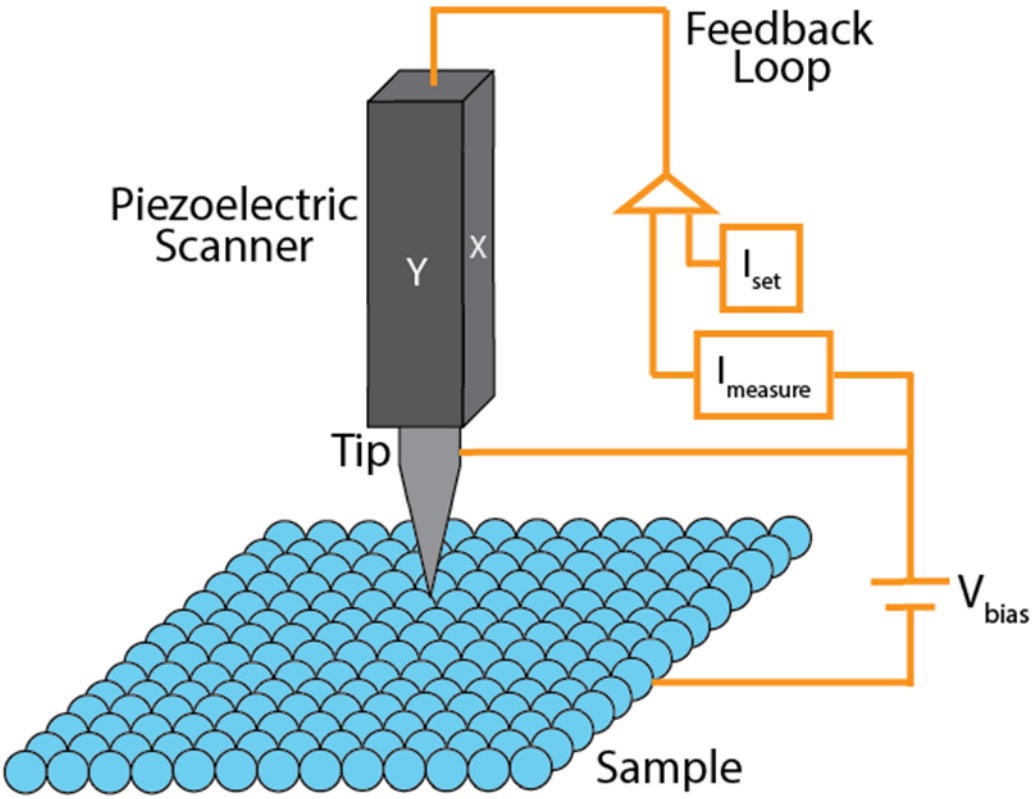

Figure 2.2.1: Schematic diagram of the STM tip-sample junction electrical setup.

The piezoelectric effect is a phenomenon where some materials generate a small electric response when it is stretched or squeezed. This property also works in reverse allowing you to strain the material by applying a voltage across it. This enables the STM tip to move across the sample laterally as well as adjust its vertical position with subatomic precision. The STM tip and sample are connected with a bias line, which allows the electrons to tunnel between different occupied and unoccupied states of the sample and tip (Figure 2.2.2). Lastly the tunneling junction circuit contains a feedback loop which is used for taking different types of STM measurements (Figure 2.2.1).

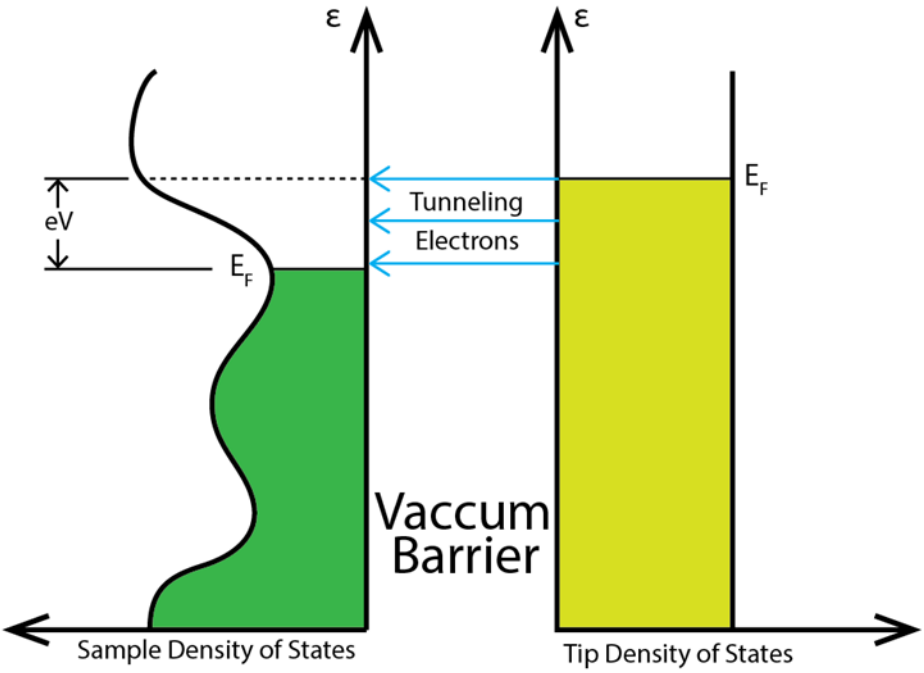

Figure 2.2.2: Diagram showing the quantum tunneling from the tips occupied states to the unoccupied state of the sample, STM tip materials typically have a very flat density of states.

The tunneling current caused by the electrons moving from sample to tip and vice versa can be expressed mathematically by:

$$i_{sample\to tip} = -\frac{4\pi e}{\hbar}\left|M\right|^2\left[\rho_s\left(\varepsilon\right)\cdot f\left(\varepsilon\right)\right]\cdot\left[\rho_t\left(\varepsilon - eV\right)\cdot\left[1 - f\left(\varepsilon - eV\right)\right]\right]$$

$$i_{tip\to sample} = -\frac{4\pi e}{\hbar}\left|M\right|^2\left[\rho_t\left(\varepsilon - eV\right)\cdot f\left(\varepsilon - eV\right)\right]\cdot\left[\rho_s\left(\varepsilon\right)\cdot\left[1 - f\left(\varepsilon\right)\right]\right]$$

Where e is the magnitude of an elementary charge of an electron, $\hbar$ is Planck's constant. The matrix element $|M|^2$ can be obtained using the WKB approximation. The sample and tip density of states is represented by $\rho_s(\varepsilon)$ and $\rho_t(\varepsilon)$ respectively, and $f(\varepsilon)$ is the Fermi distribution:

$$f\left(\varepsilon\right) = \frac{1}{1 + e^{\frac{\varepsilon}{k_B T}}}$$

Adding the tip to sample and sample to tip current contributions together and then integrating over all the energies gives us an expression for the total current:

$$I = -\frac{4\pi e}{\hbar}\int_{-\infty}^{\infty}\left|M\right|^2\rho_s\left(\varepsilon\right)\rho_t\left(\varepsilon - eV\right)\left[f\left(\varepsilon\right)\cdot\left[1 - f\left(\varepsilon - eV\right)\right]\right] - f\left(\varepsilon - eV\right)\cdot\left[1 - f\left(\varepsilon\right)\right]d\varepsilon$$

This expression for the total current as it stands is quite complicated and full of variables. One particular complicating factor comes from the finite temperature effects necessitating the Fermi distribution inside the integral. Most STMs perform measurements at cryogenic temperatures of 4.2 degrees Kelvin or lower. Because of this the Fermi distribution term is approximately one from our Fermi energy up until our applied bias voltage. While outside this range the Fermi distribution term vanishes simplifying our expression for the tunneling current to:

$$I \approx -\frac{4\pi e}{\hbar}\int_0^{eV} |M|^2 \, \rho_s(\varepsilon)\, \rho_t(\varepsilon - eV)\, d\varepsilon$$

Another condition that can further simplify this expression is the material choice for the STM's tip. Two popular choices for STM tips are tungsten and platinum–iridium because they are "boring" metals. The reason we refer to these as boring is because they have a very flat density of states that does not vary much as a function of energy. The convenience of the tip's density of states being constant means it only has a scaling effect and any variance in the tunneling current comes purely from the sample. This further simplifies our tunneling current to:

$$I \approx -\frac{4\pi e}{\hbar}\rho_t \int_0^{eV} |M|^2 \, \rho_s(\varepsilon)\, d\varepsilon$$

Next, as mentioned above the WKB approximation can be used to approximate the matrix element $|M|^2$. This is because the vacuum barrier that separates the tip and the sample can be treated as a simple square well with a bumpy bottom. Using the WKB approximation we get the matrix element is:

$$|M|^2 \approx e^{-2\frac{s}{\hbar}\sqrt{sm\varphi}}$$

Here m is the mass of an electron, s is the vacuum barrier's width and φ is the local barrier height and is a combination of the tip and sample's work function [34]. Additionally this matrix element is approximately energy independent [35] and can thus be pulled out of the integral as well giving us:

$$I \approx -\frac{4\pi e}{\hbar}\rho_t e^{-2\frac{s}{\hbar}\sqrt{sm\varphi}} \int_0^{eV} \rho_s(\varepsilon)\, d\varepsilon$$

Due to strict laboratory conditions the STM's tunneling current only depends on the density of states of the sample.

The most common type of scan and the one most people are aware of is the topograph. The name scanning tunneling microscope implies that it can be used to image things on small scales. This is

done by applying a fixed bias voltage as well as a reference current (I_{set}) . The tip and sample are connected to a feedback loop (Figure 2.1.1) that adjusts the height of the tip in order to maintain a constant measured current. As the tip moves across the sample in the xy-plane the change in the z position traces out variations on the sample's surface. Figure 3a illustrates the path the tip takes as it moves across the sample, the piezo scanner is sensitive enough to move the tip closer to the sample between atoms in order to maintain a constant current.

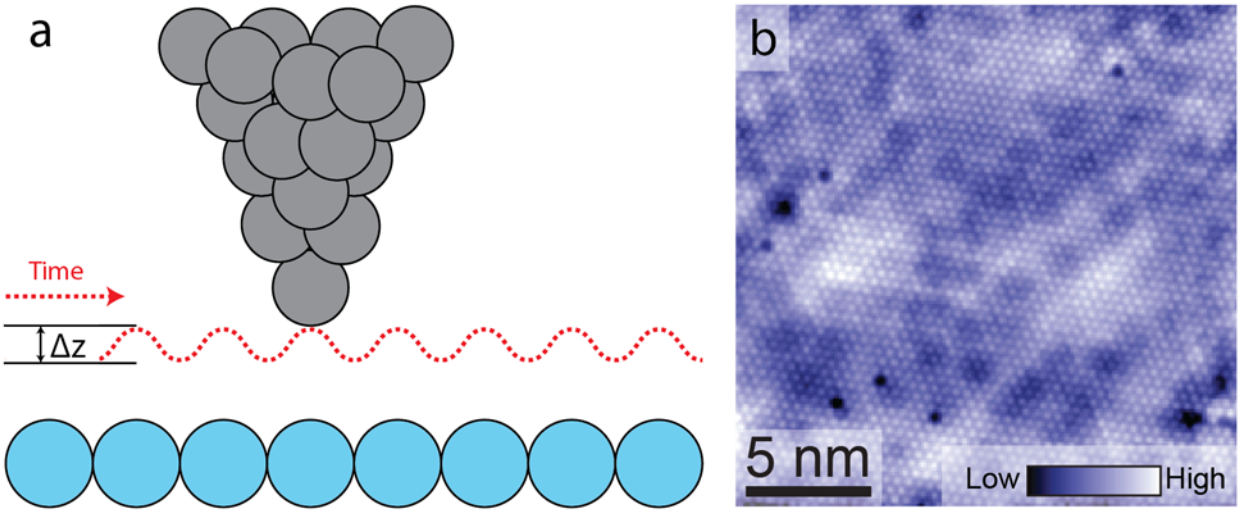

Figure 2.2.3: (a) Cartoon diagram showing how the STM tip adjusts its height in order to maintain a constant current between the sample and tip; the red dotted line is the path it will trace out. (b) Example of an STM topograph.

It should be noted that since we use the current to effectively map out the surface corrugations and since the current depends on the density of states of the sample, these topographs inevitably contain electronic information as well. Figure 2.2.3 b shows an example topograph with atomic resolution. Though the sample is flat enough to see atoms, the variations in brightness are due to the locally varying density of states.

As mentioned in the previous paragraph STM maps do not just contain structural information but electronic information as well. Recall from our equation for the tunneling current:

$$I \approx -\frac{4\pi e}{\hbar}\rho_t \left|M\right|^2 \int_0^{eV} \rho_s\left(\varepsilon\right) d\varepsilon$$

If we switch off our feedback loop this will fix the STM tip height a constant distance from the

sample. This in turn makes all the terms outside of our integral constant. Therefore, the tunneling current is directly proportional to the integral of the density of states of the sample:

$$I \propto \int_0^{eV} \rho_s(\varepsilon)\, d\varepsilon$$

While the feedback loop is switched off, we use a lock-in amplifier to modulate the applied bias voltage by a few millivolts. The lock-in applies this small modulation voltage (dV) and measures the small changes in current (dI). This effectively takes a numerical derivative of our tunneling current and is directly proportional to the local density of states of our sample.

$$\frac{dI}{dV} \propto \rho_s(eV)$$

This allows us to not only map out the geometric properties of the sample but directly probe and measure the density of states at a fixed energy. This fixed energy density of states map is aptly called a dI/dV map. An example of one is shown in figure 2.2.4 a.

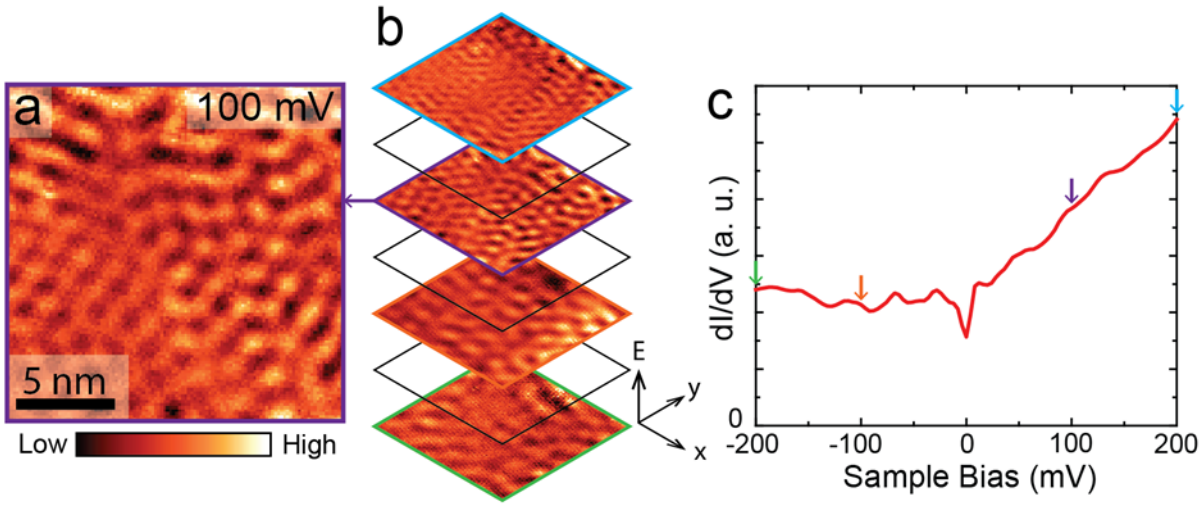

Figure 2.2.4: (a) Example of a STM dI/dV map taken at a single energy and (b) example of a DoS map that consists of multiple dI/dV maps taken at different energies. (c) Shows an example of an average spectra obtained from a DoS map, the colored arrows denote the positions of the dI/dV maps in (b).

In our topographic maps the color scale gives us predominantly structural information, while for a dI/dV map the color scale gives us mostly electronic information. While in theory a perfectly flat homogeneous crystal should not have a locally varying density of states real materials have impurities

that electrons can scatter off of.

The dI/dV map is best thought of as a slice or photo of how the density of states varies locally at a particular energy. If we change our applied bias voltage we can take another map and see how the density of states changes with energy. We can do this for several energies stacking the 2D map to make a 3D data structure we call these maps density of states map or DOS-maps for short (Figure 2.2.4 b). Furthermore we can average over a region of the sample and get a picture of our average spectrum (Figure 2.2.4 c).

By this point, it should be apparent that STM is more than just a microscopy technique but is also an extremely powerful spectroscopic technique as well. Though one drawback that STM has is that it normally cannot measure the electron dispersion directly in a way that momentum resolved techniques such as ARPES (angle resolved photo emission spectroscopy) can. The way STM gets around this is by utilizing quasi particle imaging (QPI). As mentioned before, due to impurities in real materials, electrons on the surface scatter and create local variance in the density of states. In fact these are actually standing wave patterns created by the electrons elastically scattering and interfering with themselves. Fourier transforming the dI/dV maps allows one to pick out the dominant wave vectors at a specific energy (Figure 2.2.5 a).

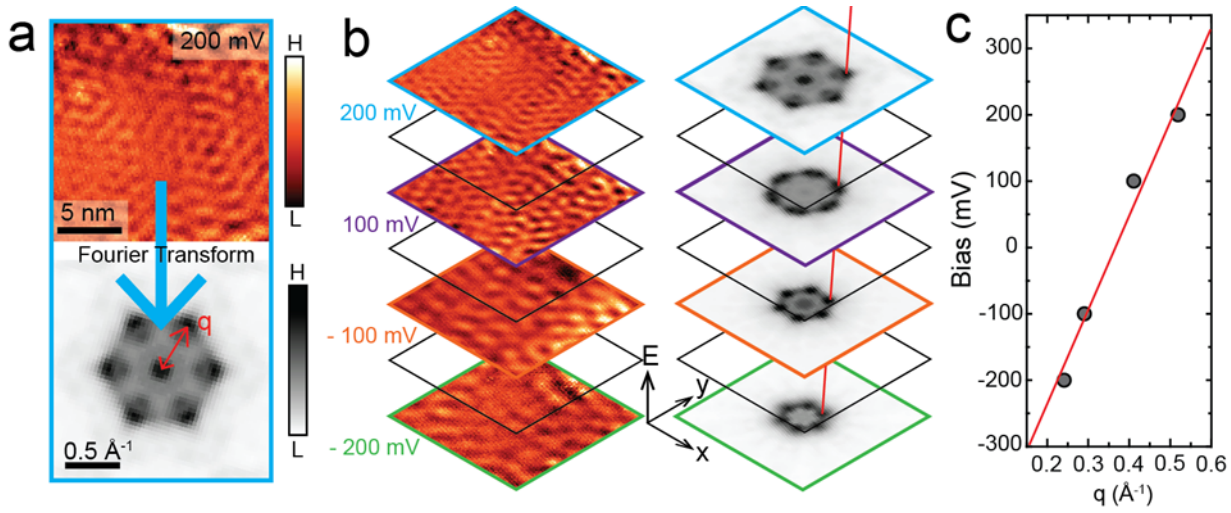

Figure 2.2.5: (a) Example of a dI/dV map and its 6-fold symmetries Fourier transform q in red denotes the length of the scattering vector. (b) Example of a Fourier transformed DoS map showing how the length of the scattering vector varies with sample bias (red line). (c) QPI dispersion extracted from the scattering vector lengths in (b).

Doing this for a collection of dI/dV maps (Figure 2.2.5 b) allows you to directly measure the electron dispersion (Figure 2.2.5 c). This technique was pioneered by Jenny Hoffman in the early 2000's [36] and has been widely used by the STM community to electronically characterize various materials. APRES measures the momentum of electrons that are ejected from the sample. Because of this ARRPES cannot measure the unoccupied states beyond the Fermi level. STM on the other hand is able to bias the sample and tunnel into the unoccupied states, allowing one to map the electron dispersion beyond the Fermi level.

Chapter 3 - Experimental Equipment

3.1 Home Built Molecular Beam Epitaxy

When I joined the lab of Professor Ilija Zeljkovic, he had recently joined Boston College's faculty. As someone who greatly enjoys building things, I was excited to be able to help build the lab from the ground up. I was primarily tasked with building and designing our home built MBE system, to interface with a commercial Unisoku STM system that we planned to purchase. In this section I will describe in detail the MBE system I built, the commercial STM that was used to characterize my samples as well as the vacuum suitcase that allowed for uncontaminated sample transfers.

The primary system I used during my Ph.D. studies was our home built MBE system pictured below (Figure 3.1.1). The main MBE chamber is connected to a load lock separated by an ultra-high vacuum gate valve, the load lock has its own turbo pump allowing us to maintain vacuum better than 5×10^{-9} mbar at all times.

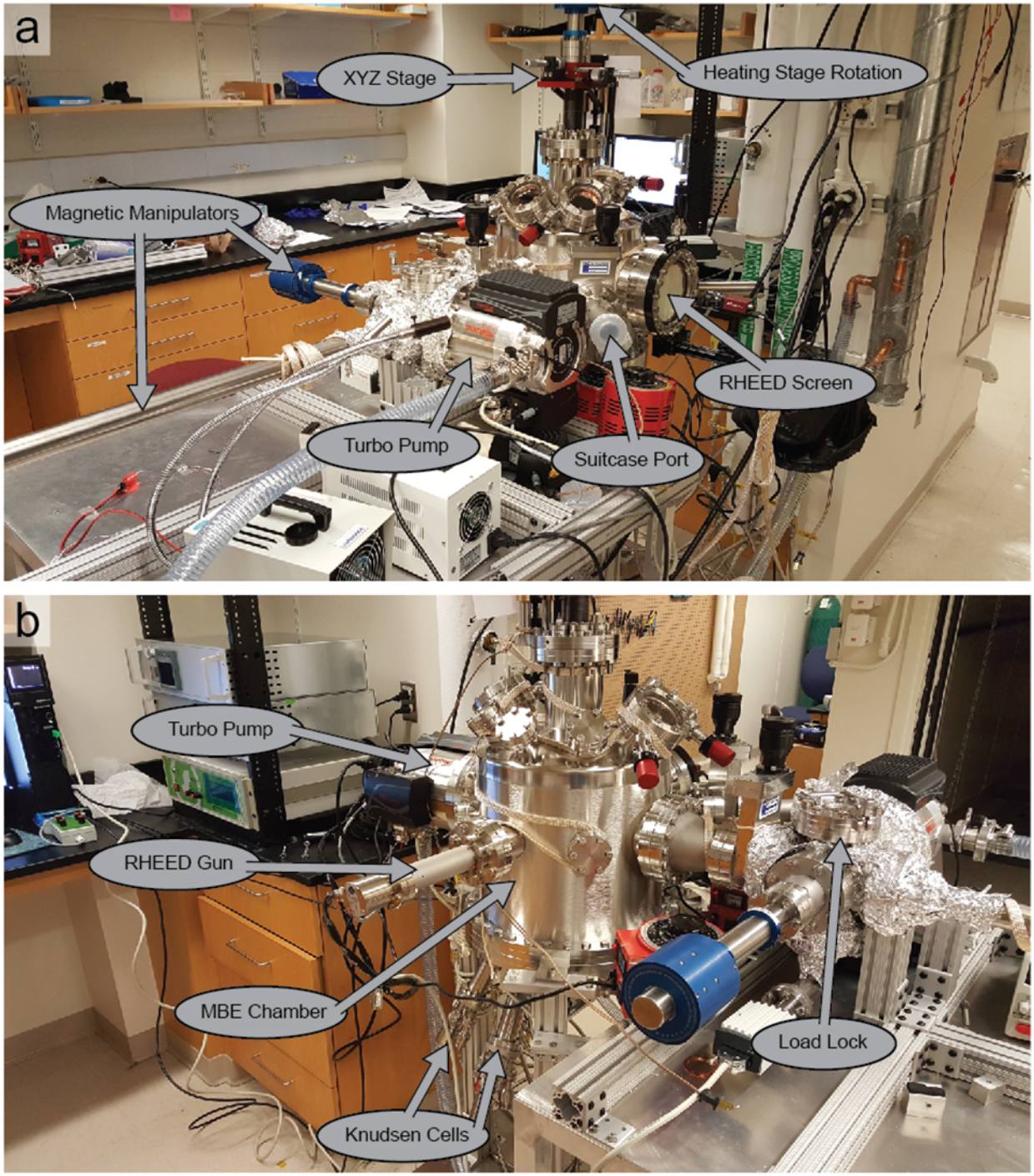

Figure 3.1.1: (a,b) Photos of the homebuilt MBE system used in the Zeljkovic lab

Magnetic manipulators allow us to transfer the sample from the load locks storage to the heating stage located at the center of the MBE chamber. The heating stage is mounted to a xyz-stage and rotation arm so the sample position can be adjusted. The effusion evaporators known as Knudsen cells (named after Martin Knudsen their inventor) are located at the bottom of the chamber with a line of sight to the substrate heater. A RHEED gun and screen are located opposite to one another in order

to monitor the sample growth quality in real time. Lastly an extra port with a gate valve is added so we can interface it with a vacuum suitcase that I will elaborate on later.

The goal in building this MBE was to be able to interface it with a commercial Unisoku USM1300 STM. In order to make this possible we designed the MBE to use the same "unisoku" style sample holder (Figure 3.1.2) as our STM. These sample holders are designed with three electrically isolated wings made of titanium and molybdenum. Two of the wings are connected in series by a tungsten filament between them. This allows us to run a current through the filament heating up the whole sample holder much like a light bulb. The third wing connects to the top plate where the sample is mounted; this wing is used to bias the sample while it is inside the STM.

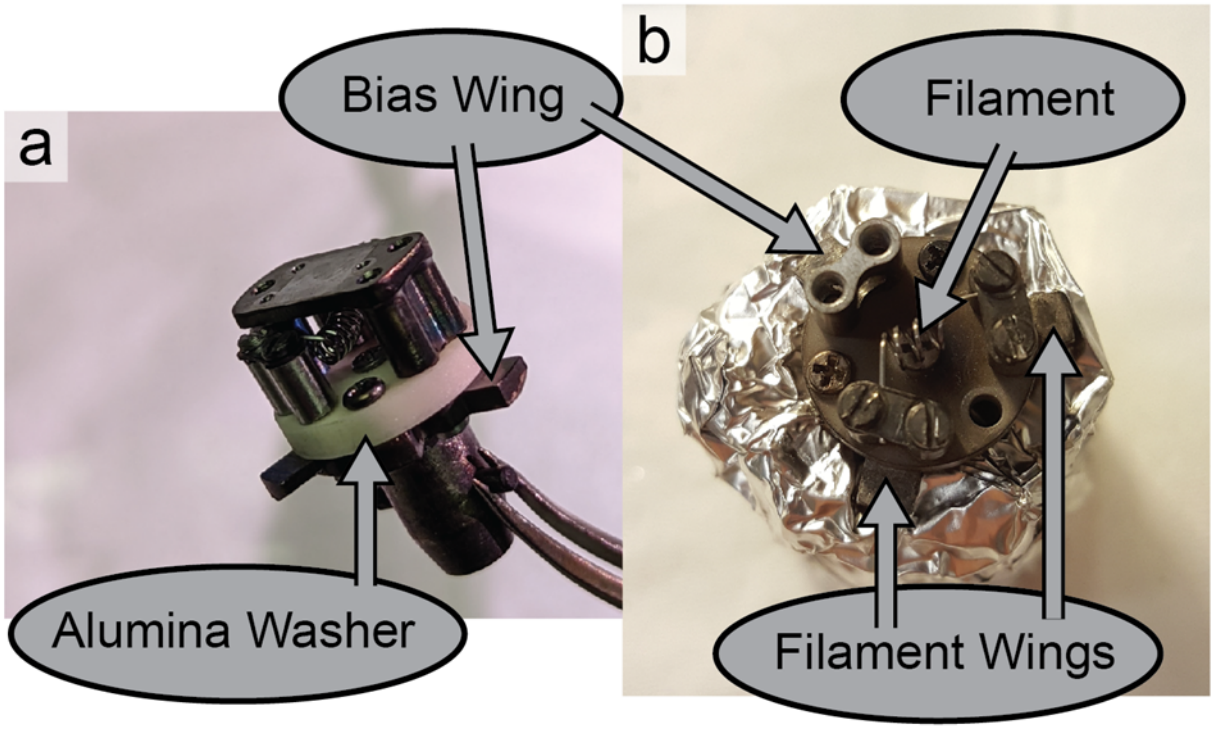

Figure 3.1.2: (a,b) Photos of the unisoku style sample holder showing how the filament wire is connected to two of the wings.

At first we built a heating stage in house in our machine shop. And although it worked for some time, we later decided to purchase and modify an off the shelf heating stage directly from Unisoku. Once the load-lock has reached sufficient vacuum pressures the sample holder is moved into the main MBE chamber where the wings of the sample holder slot underneath the electrically isolated spring of

the heating stage (Figure 3.1.3 a). There is a knob on the side that allows one to tilt the sample so it is facing down toward the Knudsen cells (Figure 3.1.3 b). The "half-moons" allow one to maintain electrical contact when moving it between the exchange position and the growth position (Figure 3.1.3 c).

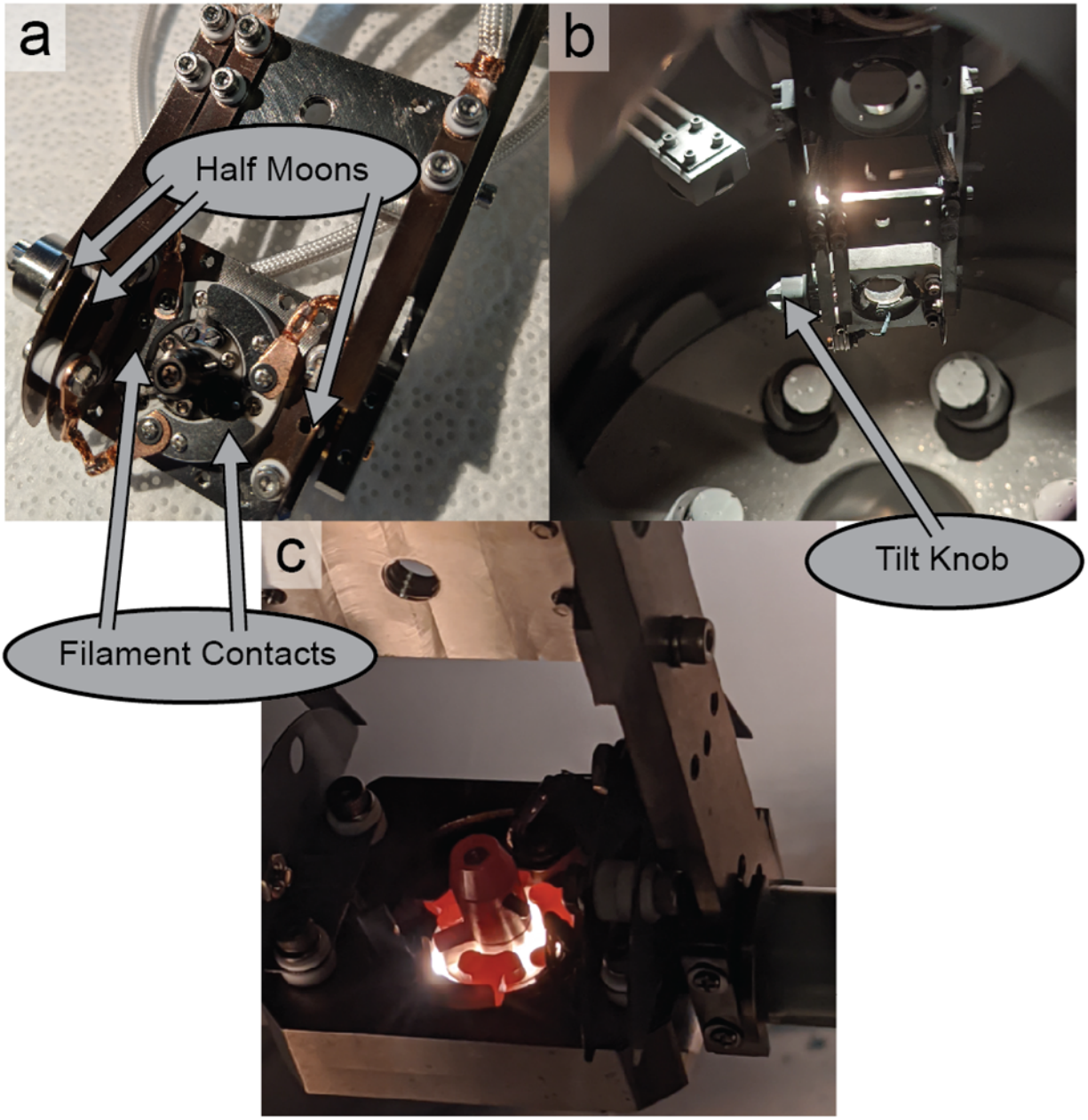

Figure 3.1.3: (a-c) Photos of the MBE's unisoku style heating stage, showing (a) how the filament makes electrical contact with the heating stage springs and (b) how it is tilted to face down at the evaporators. (c) Shows an example of sample holder glowing from being heated up to high temperatures.

In order to calibrate the sample holders, we use a separate heating stage that is located in our load-lock. Instead of a substrate being glued to the top plate, we spot weld a k-type thermocouple. This allows us to measure the surface temperature of our sample holders as a function of applied current. Typically 2.3 A corresponds to around 250 °C and increases fairly linearly from there at a rate of about 13 °C per 0.1 A.

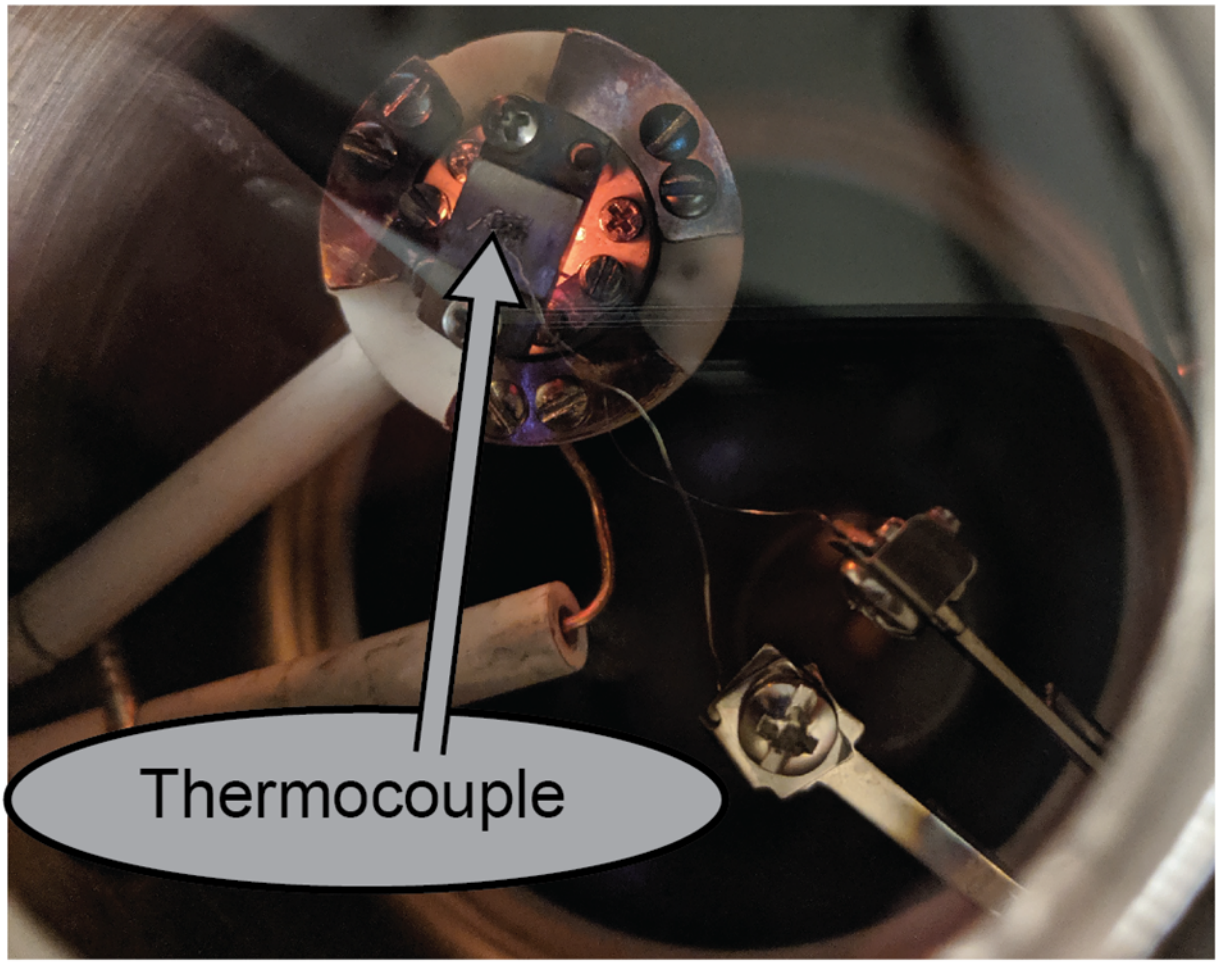

Figure 3.1.4: Photo of the calibration stage inside the load lock of the MBE, showing the K-type thermocouple stop welded to the top of the sample plate.

The calibration is very consistent between different filaments typically only being off by a couple degrees at most, I attribute this to all the filaments I fabricate being very close in size and shape.

3.2 Substrate Preparation

For preparing the sample holder with a substrate for MBE growth there are two kinds of single crystals one might use. The first being cleavable single crystals (Figure 3.2.1 a), these materials consist of 2D layers that are weakly van der Waals bonded together. The second kind are polished single crystal substrates (Figure 3.2.1 b). Typically these are purchased from companies that specialize in making single crystal substrates.

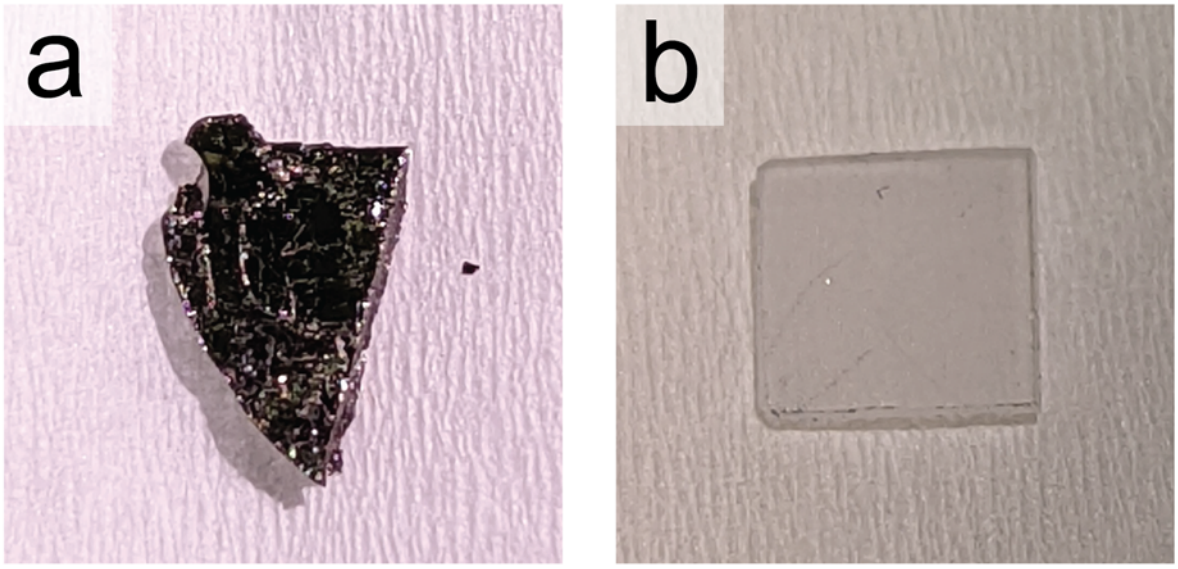

Figure 3.2.1: (a) An example of $Fe(Te, Se)$ substrate that can be cleaved, and (b) an example of a Al_2O_3 substrate that has one side polished.

The majority of the work presented in this thesis was done using cleavable substrates. To prepare these for growth we start by applying a small amount of two part silver epoxy to the center of our top plate (Figure 3.2.2 b), next I would find an oversize crystal and press it gently into the epoxy (Figure 3.2.2 c). The whole sample holder is then heated up to ~150 °C to cure the epoxy and bond it to the sample holder.

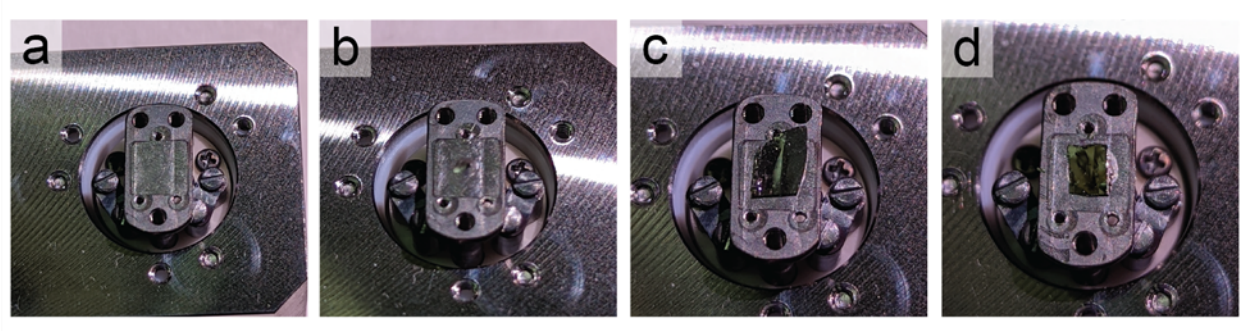

Figure 3.2.2: (a-d) The first series of steps for preparing a cleavable single crystals, (a) sample holder top plate with nothing on it, the holes are used for other types of a mounting. (b) Example of the amount of silver epoxy used, (c) epoxying down an oversized piece and (d) trimming it after curing.

After the epoxy has been cured and the sample holder has cooled back down I then trim the sides of the sample with a razor blade (Figure 3.2.2 d). I do this by cutting straight down with a fresh razor blade and then scrapping away the cut piece in a single action. I've found that this step ensures that extra epoxy does not get on the edge of the sample which could lead to a failed cleave. After the sample is sized a cleaving rod is prepared with one side flattened so it can stand up straight on its own (Figure 3.2.3 a).

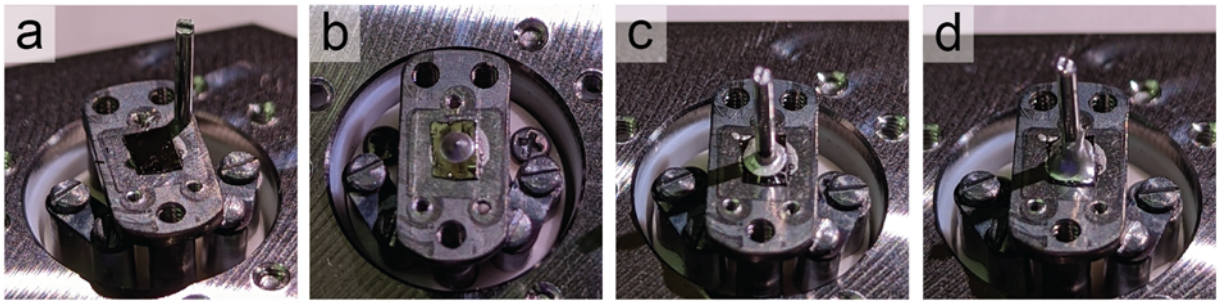

Figure 3.2.3: (a-d) The steps for effectively attaching a cleaving rod to a substrates surface, (a) the cleaving rod should be able to stand up on its own. (b) Example of a blob of epoxy on the substrate surface and (c) after it has been used to adhere a cleaving rod to the sample. (d) Additional epoxy is added to provide more support increasing the chances of a successful cleave.

Next a small blob of epoxy is added to the sample surface (Figure 3.2.3 b) and the rod is placed on top of the fresh epoxy (Figure 3.2.3 c). It is important that the cleaving rod stand without the aid of the added stickiness of the epoxy because when the epoxy is curing it becomes less viscous for a short period of time and the rod could fall over during curing. After the cleaving rod has been cured we let

it cool down before adding additional epoxy to the sample surface and up the rod (Figure 3.2.3 d), being extremely careful not to get epoxy on the edges of the substrate. After it has cured the sample holder is put into our load lock and pumped down, when the pressure is better than 5×10^{-7} we knock the rod off exposing a clean surface in vacuum. For demonstration purposes figure 3.2.4 shows the removal of a cleaving rod in air.

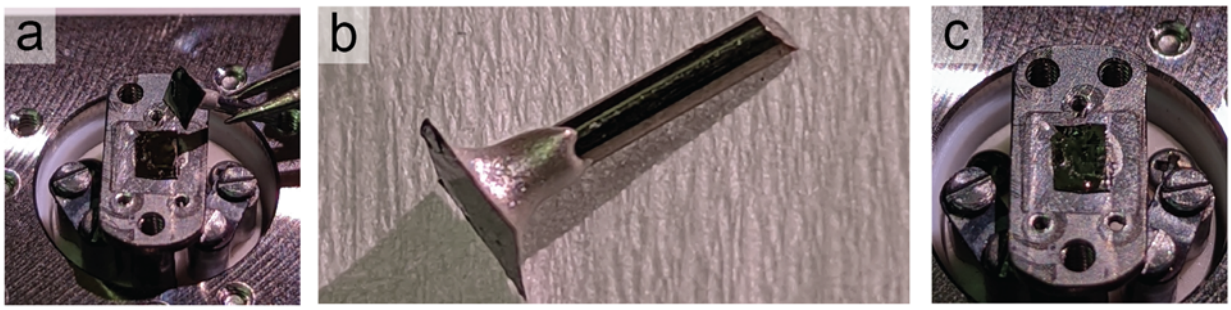

Figure 3.2.4: (a-c) Demonstration of cleaving a sample in air (a) shows the removal of the rod using tweezers, (b) the removed rod with some of the substrate with it and (c) the remaining substrate on the sample holder.

As you can, see once the rod is removed it takes several layers with it but most importantly also leaves some behind on the sample holder. This remaining substrate is what we grow our films on.

The other type of single crystal substrates one could use for MBE are non-cleavable polished ones. For example, the two main ones I've used are Al_2O_3 (Figure 3.2.1 b) and $SrTiO_3$. These typically go through some sort of cleaning procedure before being put in vacuum. I'm going to cover the way you would prepare the specific oxide substrates Al_2O_3 and $SrTiO_3$. The substrates are purchased with one side polished. We submerge these polished single crystals first in acetone and sonicated for 10 minutes. After that it is then sonicated for an additional 10 minutes in isopropyl alcohol. Once the substrate has been thoroughly cleaned, we then put it inside a tube furnace (Figure 3.2.5).

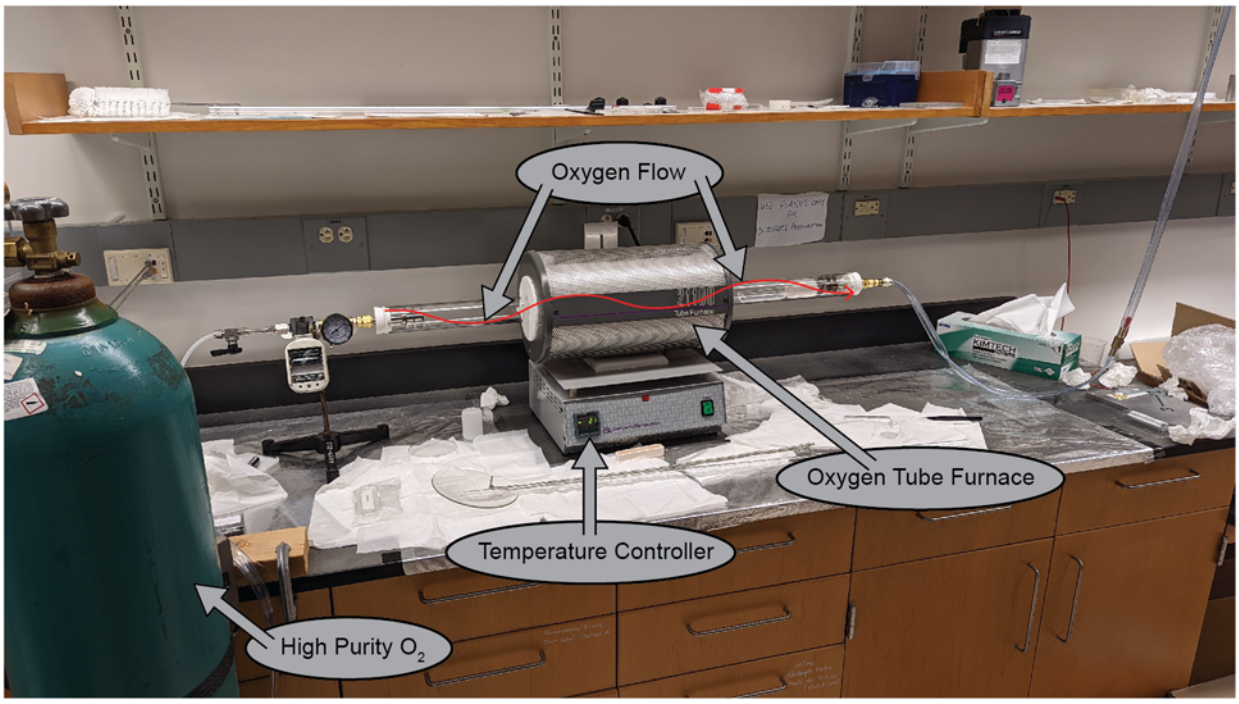

Figure 3.2.5: Photo of the tube furnace we use to anneal our oxide single crystal polished substrates in. The red wavy arrow denotes the direction of oxygen flow.

The tube furnace is preheated to 1000 °C and is subjected to 1500 cm^3/min of oxygen flow prior to putting the substrate inside. The substrate then anneals inside the tube furnace for two hours. This crucial step reintroduces surface oxygen to our substrates that have naturally escaped over time. Lastly after the substrate has been annealed in oxygen we mount it to our sample holder using three 000-120 titanium screws (Figure 3.2.6)

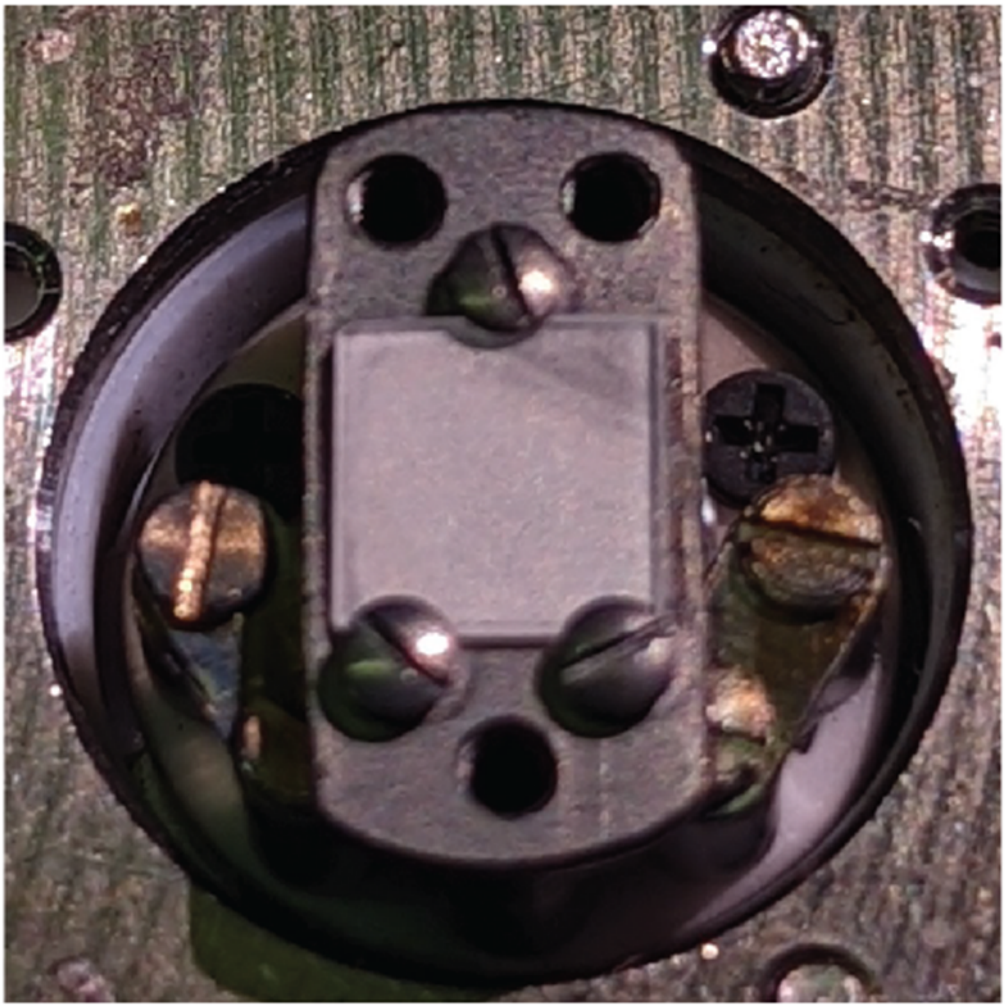

Figure 3.2.6: Photo showing how we attach our polished single crystal substrates that we prepare in the tube furnace, we use three 000-120 titanium screws that hold the substrate down with their heads.

After this we put the sample holder in the load lock. Once the load lock pressure is sufficient enough to transfer the sample holder to the MBE's heating stage we then anneal it in vacuum at around 500 °C for another couple of hours. Then the substrate is tuned to our growth temperature and is ready for thin film deposition.

3.3 Zeljkovic Lab's Scanning Tunneling Microscope

Over the past few decades the scanning tunneling microscope has worked its way into the general public's familiarity. Many are aware that it is some sort of fancy microscope that lets you image atoms

but few people have seen what one typically looks like. When I've given tours of our lab and have introduced people to our microscope (Figure 3.3.1) most are surprised about how big it is.

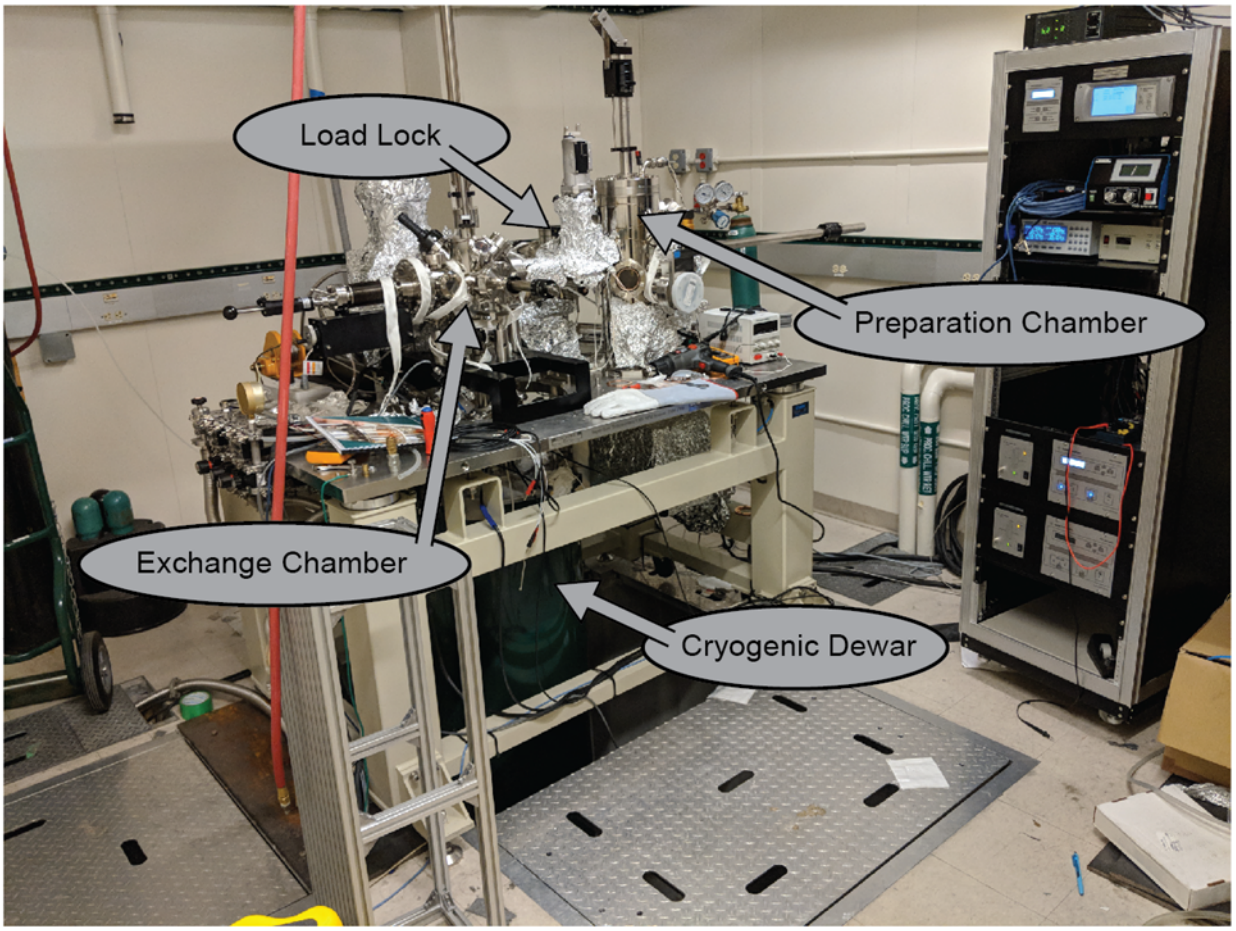

Figure 3.3.1: A photo of the Unisoku USMI1300 STM in the Zeljkovic lab with various parts labeled

I typically go on to explain that everything one sees is just various ultra-high vacuum chambers that aid in our STM studies and that the STM itself is fairly small and sits at the bottom of the green cryogenic dewar. This dewar under the table can be lowered if one needs to access the microscope for repair, but in ideal circumstances you never see the STM. On top of the table there are three separate chambers with gate valves between them. Similar to the MBE the STM also has a load lock so samples can be loaded without the need to vent the whole system to atmosphere. The preparation chamber contains a heating stage, tip annealer and sputter gun for various STM sample and tip preparation. The last chamber before the sample goes into the STM is aptly named the exchange chamber. This chamber contains sample storage as well as a cleaver. A gate valve underneath the exchange chamber

can be opened and a long magnetic manipulator is used to transfer the sample into the STM itself (Figure 3.3.2 b).

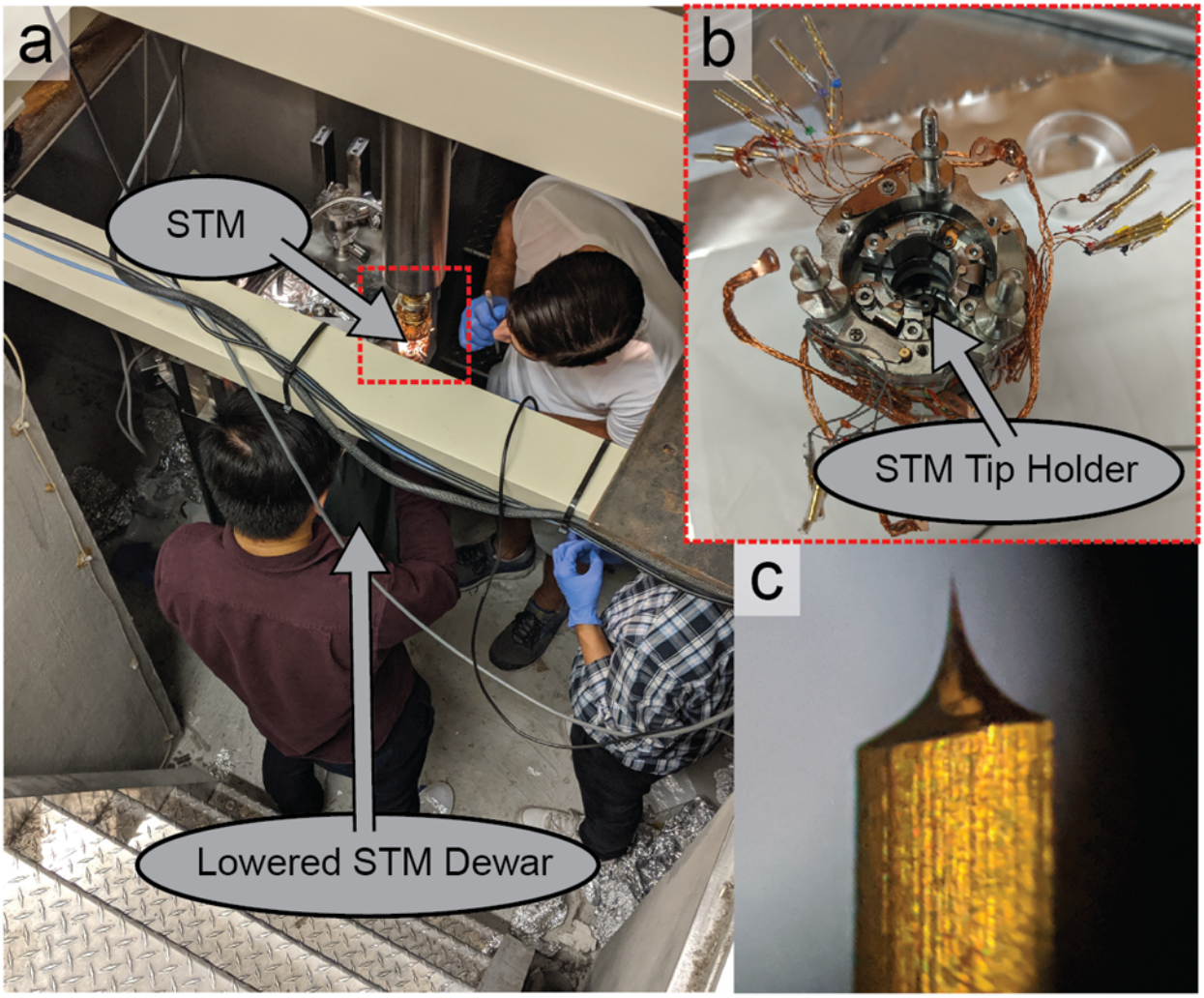

Figure 3.3.2: (a) Photo of the STM being worked on after the dewar had been lowered, (b) close up of the STM after it had been removed and (c) microscope photo of a chemically etched tungsten tips.

Figure 3.3.2 a is a photo of one of the rare times the dewar has been lowered the STM itself is outlined in red. When removed you can see down inside it where the STM tip is inserted (Figure 3.3.2 b). The STM tips we use are typically chemically etched in house tungsten tip (Figure 3.3.2 c).

3.4 Vacuum Suitcases

So far I've introduced the two main experimental techniques MBE and STM. The main drawback of STM is that you must have a very flat surface that has never been exposed to air. Because of this it is difficult to study materials that cannot be cleaved. In order to get around this difficulty we utilized a vacuum suitcase to interface between our ultra-high vacuum systems (Figure 3.4.1)

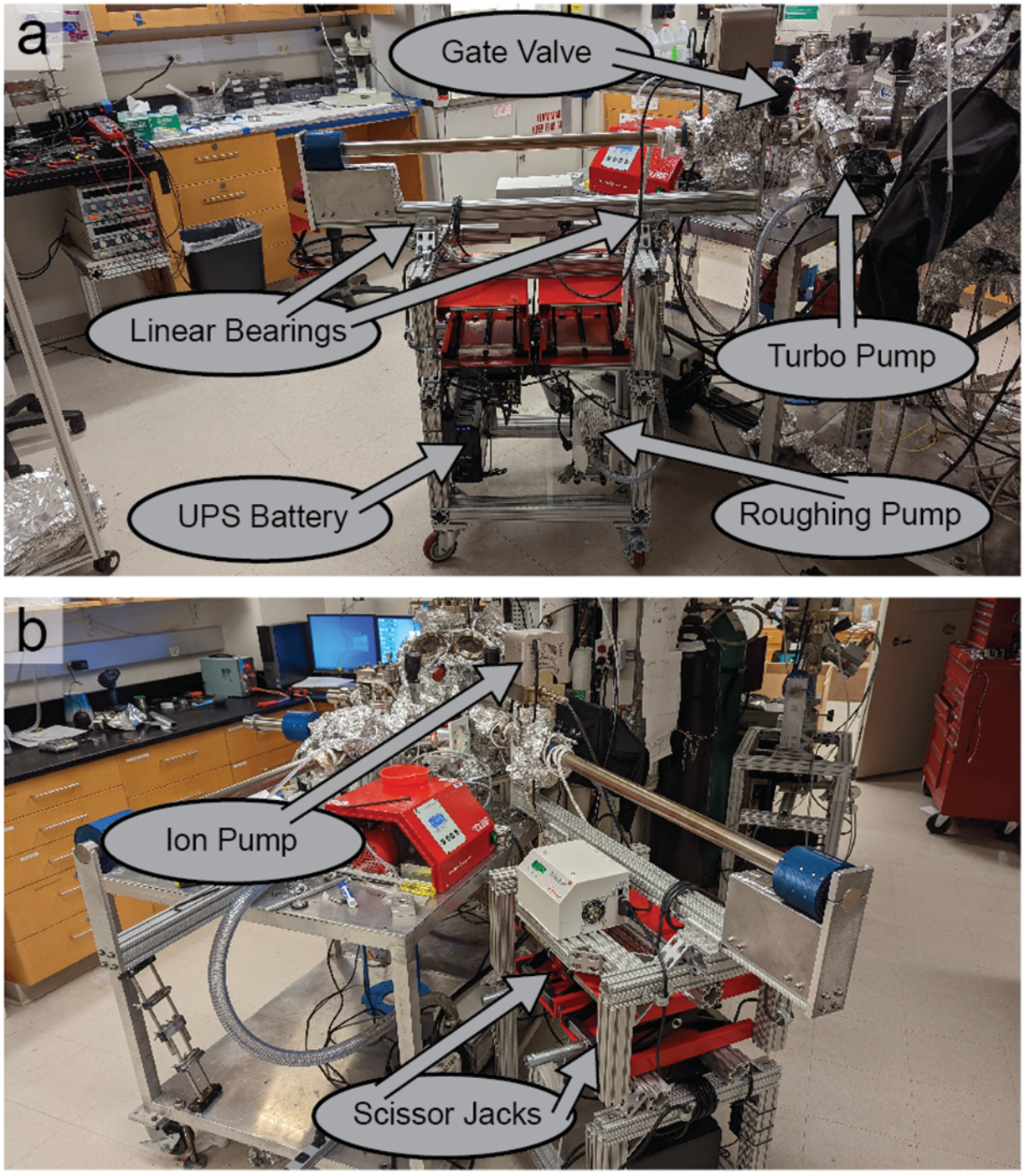

Figure 3.4.1: (a,b) Photos of one of our vacuum suitcases attached to the MBE chamber with the

various parts labeled.

The vacuum suitcases I built are sort of a portable vacuum chamber on wheels. The front end has a turbo pump backed by a roughing pump (Figure 3.4.1 a), this intermediary space attaches to the MBE chamber's gate valve and is separated from the rest of the suitcase by an additional gate valve (Figure 3.4.1 a). This space can be pumped down to achieve ultra-high vacuum conditions. The main part of the suitcase with the transfer arm is kept at pressures lower than 10^{-10} mbar at all times by an ion pump (Figure 3.4.1 b). The whole suitcase sits on a custom built cart with wheels that allows one person to attach and transfer samples. The cart can be raised and lowered thanks to two scissor jacks (Figure 3.4.1 b), additionally the angle of the cart can also be adjusted by manipulating the scissor jacks separately. Lastly the suitcase sits on linear Teflon bearings that allow the whole suitcase to slide in and out while the cart remains stationary.

On the end of the suitcase's magnetic manipulator arm is a unisoku style grabber that lets us remove the sample from the MBE and store it safely inside the suitcase's ultra-high vacuum space. When the STM is ready to accept the sample, the suitcase can be wheeled over and connect to the STM's suitcase port (Figure 3.4.2)

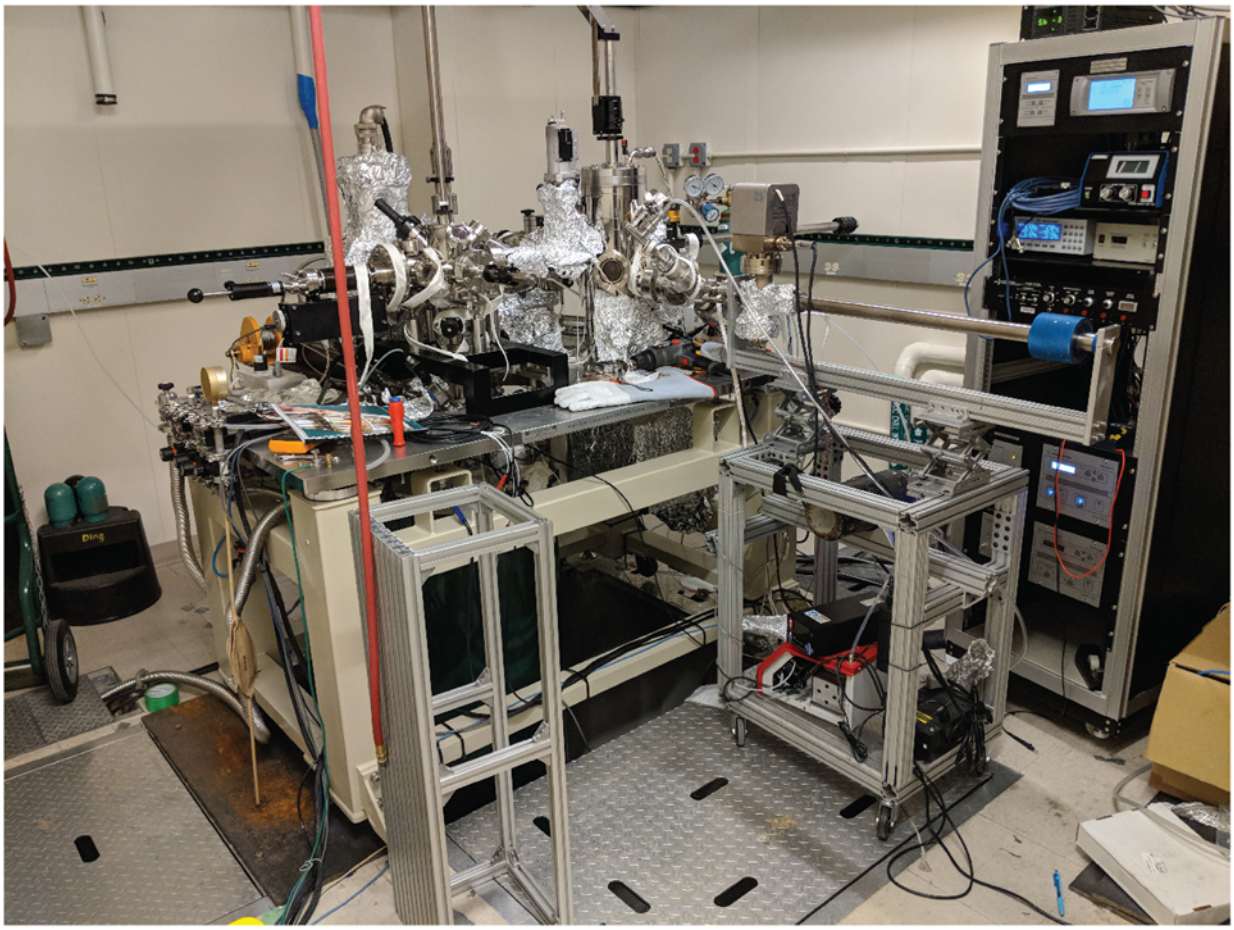

Figure 3.4.2: Photo of one of our suitcases attached to our STM pumping down in preparation to transfer a sample.

We typically let the suitcase's intermediary space turbo pump run for over an hour before transferring the sample out of the suitcase and into the STM to ensure good vacuum conditions. The suitcase is then disconnected from the STM so as to not couple it to the vibrations of the room.

Chapter 4 - Use of an Iron Based Superconducting Substrate

4.1 $Fe(Te, Se)$ a High-T_c Superconducting Substrate

One promising way to realize a topological superconductor is with the use of the superconducting proximity effect (SPE). When a normal metal and a superconductor are brought in close proximity Cooper pairs will tunnel across the boundary leading to superconductivity on the surface of the normal metal [37]. Even though the discovery of the SPE happened in the 1960s it saw significant resurgence in this past decade due to promising new theoretical applications. One example that has drawn a lot of attention is that of Liang Fu and Charlie Kane. They theorized that with the use of the SPE you could induce superconductivity in a Z_2 topological insulator. When a magnetic field is applied to this system it will lead to a collective excitation known as a Majorana bound state [17]. The superconducting proximity effect requires precise control over the thickness of the TI film. This makes molecular beam epitaxy the natural technique of choice for synthesizing these heterostructures as the slower growth rate enables you to grow films precisely down to a single layer. Most of the prior work on TI/SC heterostructures has focused on the use of elemental superconducting substrates [25, 26] and low-T_c superconductor $NbSe_2$ [38, 21, 22, 23, 24]. Due to the low superconducting transition temperature, the induced gaps are fairly small on the order of ~1 mV [38, 21, 22, 23, 24], making it particularly challenging to characterize the emergent phenomena. The natural question to ask is why not use high-T_c superconductors to induce larger gaps in the TIs. Cuprate superconductors such as $Bi_2Sr_2CaCu_2O_{8+x}$ have a very high-T_c of ~91 K and large superconducting d-wave gap of ~40 mV seem to be a natural choice, but at the time of conducting this experiment the results had been mixed [27, 24, 28, 29]. These conflicting results have been attributed to Bi-2212 having a very short coherence length along the c-axis making it difficult to induce superconductivity [28], as well as there being a Fermi surface mismatch between the TI and Bi-2212 substrate [24, 28]. We will visit the use of optimally doped Bi-2212 as a substrate in the next chapter. High-T_c Iron based superconductors have only recently started being synthesized in 2008 [39] and could be a promising alternative as their pairing symmetry is believed to be s-wave [40]. Much like their cuprate counterparts they also exhibit much higher super conducting transition temperatures compared to most other superconductors [40], and in case of single layer $FeSe$ on $SrTiO_3$ rivaling that of some cuprates [41, 42]. In this chapter I'm going to cover the growth and characterization of two different topologically superconducting

heterostructures utilizing an iron based superconductor as the source of the induced superconductivity.

We picked $FeTe_{1-x}Se_x$ as our substrate for a couple of reasons, the first being it is a layered material where the layers are weakly van der Waals bonded. This gives it a natural cleavage plane (Figure 4.1.1 a) that exposes a square lattice of Te and Se atoms (Figure 4.1.1 b).

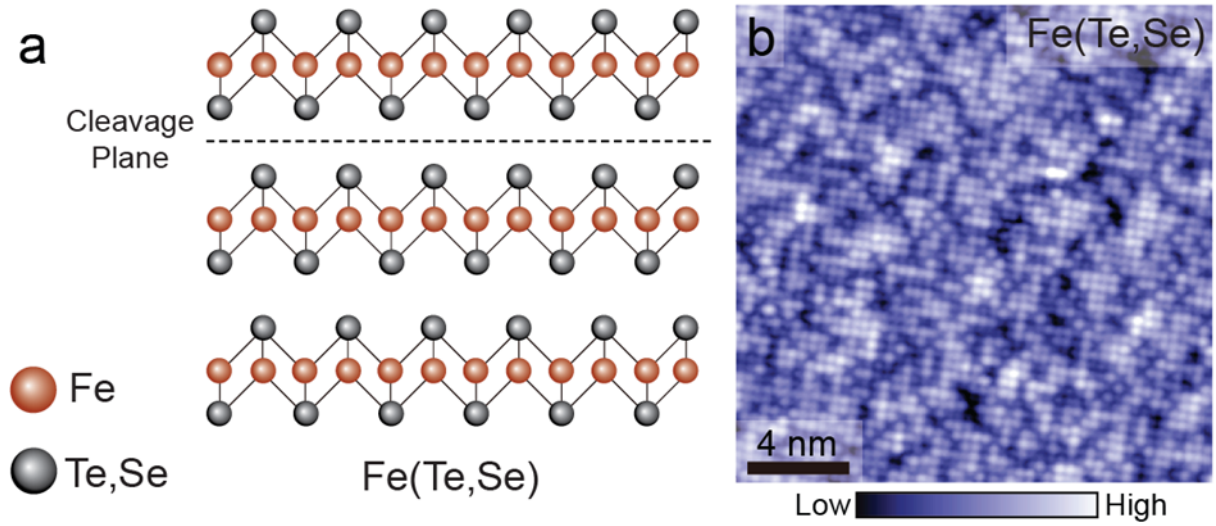

Figure 4.1.1: (a) Side view diagram of $Fe(Te, Se)$'s crystal structure, dashed line indicates the plane it cleaves between. (b) STM topograph of the characteristic square lattice of freshly cleaved $Fe(Te, Se)$.

Being able to be cleaved makes it a good substrate for MBE as it allows us to expose a clean uncontaminated surface to grow our film on. The second reason we picked $FeTe_{1-x}Se_x$ as our substrate is that tellurium doping $FeSe$ allows you to enhance the T_c [43]. Bulk $FeSe$ has a T_c of about 8 K [44] but tellurium doping allows you to push the T_c to almost 15 K [43]. We picked the particular doping of 45% Se to 55% Te because it gives the greatest enhancement of T_c , since all the $FeTe_{1-x}Se_x$ is x = 0.45 I will refer to $FeTe_{0.55}Se_{0.45}$ as just $Fe(Te, Se)$ from this point on. $Fe(Te, Se)$ because of its much higher T_c has a larger superconducting gap greater than 2.5 mV on its surface (Figure 4.1.2).

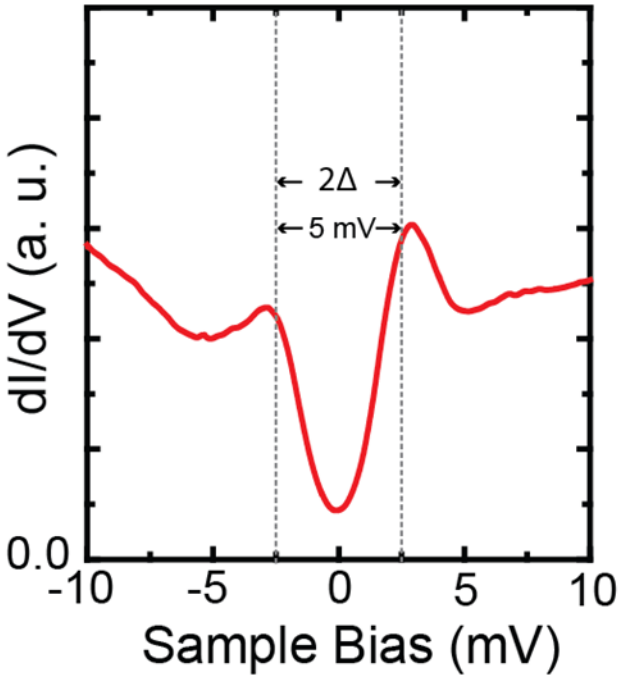

Figure 4.1.2: Average dI/dV spectra taken on the surface of $FeTe_{0.55}Se_{0.45}$ showing a prominent superconducting gap of ~2.5 mV.

This larger gap will allow us to induce much more robust superconductivity in our topological insulator film increasing the likelihood of detecting in gap states on the surface of our heterostructure.

4.2 Bi_2Te_3 Thin Film Growth on $Fe(Te, Se)$

The topological insulator Bi_2Te_3 was one of the first 3D topological insulators to be theoretically predicated [14] and experimentally verified to possess surface states [12]. Bi_2Te_3 also lends itself nicely to being synthesized using MBE because it is a naturally layered material. Typical growths of Bi_2Te_3 involve co-evaporating Bi and Te in separate effusion cells. The binary phase diagram (Figure 4.2.1) shows the various compounds that can be formed with different ratios of Bi to Te atoms.

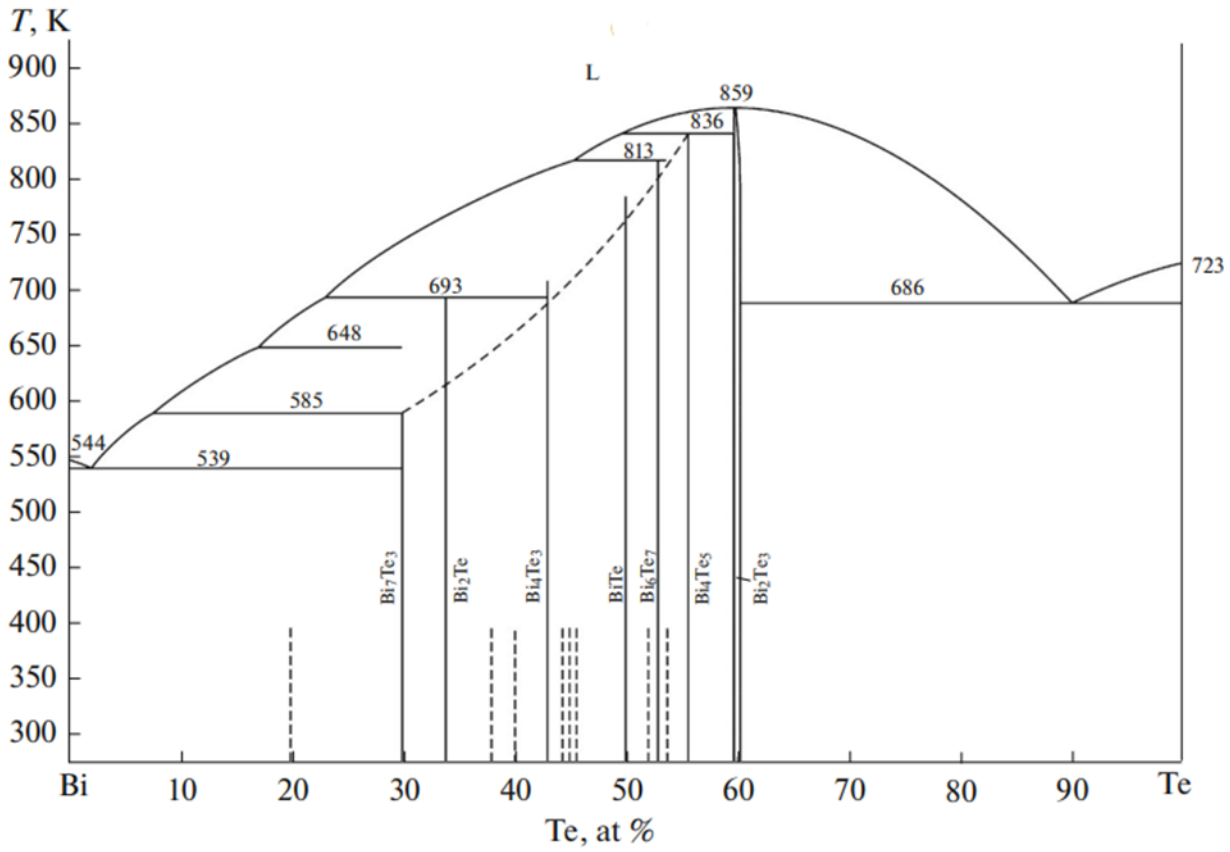

Figure 4.2.1: Phase diagram showing the different binary compounds comprised of bismuth and tellurium. This diagram is from reference [45].

As you increase the percentage of tellurium to around 60% you should start to favor Bi_2Te_3 instead of forming Bi_4Te_5. As we increase the Te percent even more we still favor Bi_2Te_3 . This fact means that as long as we have excess Te flux we should only ever grow Bi_2Te_3 and the bismuth flux alone determines the rate at which the layers are formed. To grow our Bi_2Te_3 /$Fe(Te, Se)$ heterostructure we start with high quality $Fe(Te, Se)$ single crystals grown using the self-flux method by our collaborator Genda Gu at Brookhaven nation lab. Using silver epoxy we glue the $Fe(Te, Se)$ single crystal to our sample holder and we also use the same epoxy to glue a cleaving rod onto the surface of our substrate. The substrate is put into our UHV load lock and cleaved when the pressure is lower than 10^{-7} mbar this ensures that new exposed surface is free of contaminants. The sample holder is then transferred to the main MBE chamber, where a filament positioned behind the substrate is used to heat it up. This serves two purposes, first it outgases the sample holder so its contamination does not contribute to the growth then it elevates the substrate temperate to achieve our desired growth conditions. We next use our RHEED system to check if the $Fe(Te, Se)$ cleaved well. If the cleave was successful we

should see a streaky RHEED pattern where the spacing between streaks is proportional to the lattice constant of our single crystal $Fe(Te, Se)$ (Figure 4.2.2 a).

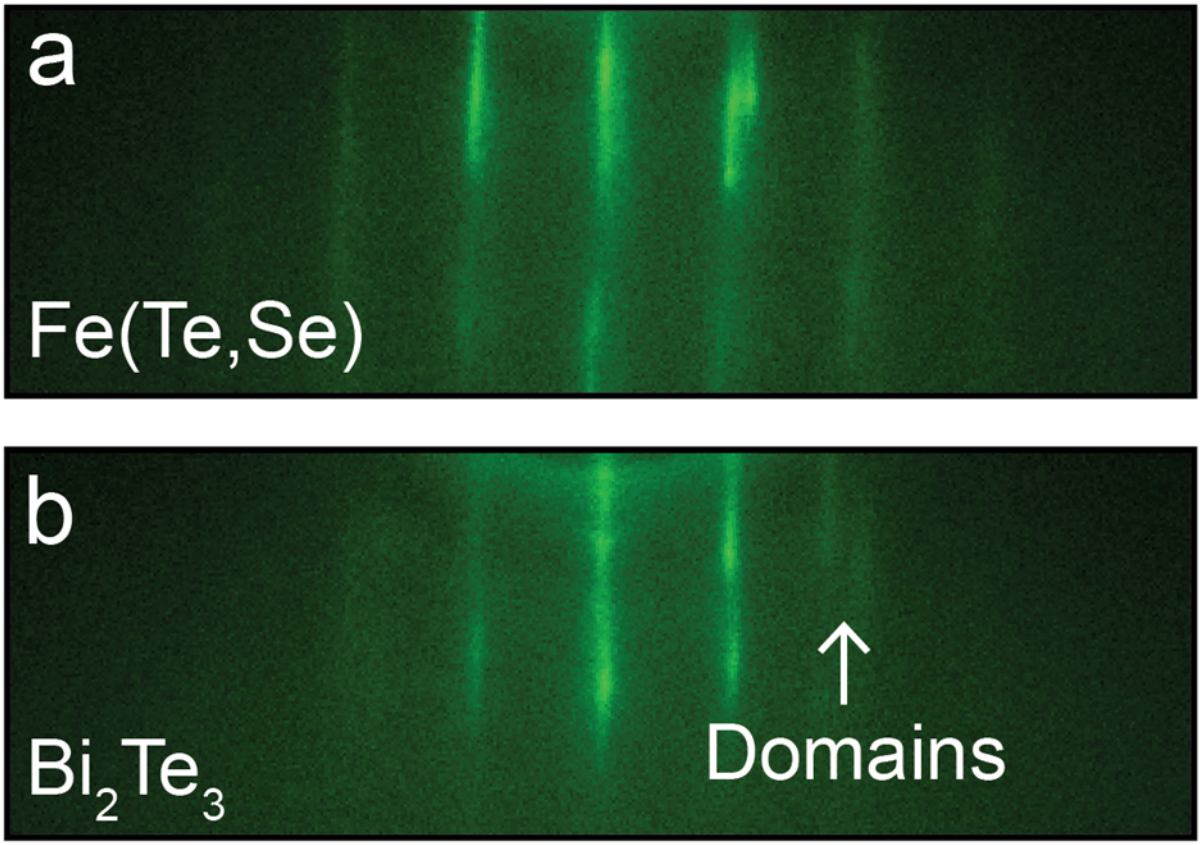

Figure 4.2.2: (a) RHEED image of as cleaved $Fe(Te, Se)$ and (b) RHEED image taken after a couple minutes of Bi_2Te_3 deposition showing the domain boundary formation

While the substrate outgasses at the Bi_2Te_3 growth temperature of ~250 °C we heat up high purity bismuth and tellurium inside separate effusion cells to 412 °C and 283 °C respectively. At the time of conducting this experiment these temperatures corresponded to deposition rate of 1 Å/min of elemental bismuth and 10 Å/min of tellurium. These rates were calibrated using a quartz crystal growth monitor. This nominal 1:10 flux ratio of Bi:Te ensures that we are growing in tellurium rich conditions which should favor the growth of Bi_2Te_3 instead of one of the other possible binary compound phases (Figure 4.2.1). When the sample outgassing is finished and the MBE pressure is on the order of 10^{-9} mbar we start the growth by first opening the tellurium shutter. Tellurium by itself will only condense at substrate temperatures closer to room temperature; this makes sure that we have plenty of Te flux before the bismuth arrives. The growth officially starts once the bismuth shutter is opened, within a

few minutes you should start the see the RHEED pattern change as the first Bi_2Te_3 layer is formed; at these flux rates it takes about 4 minutes. Figure 4.2.2 b shows the characteristic RHEED pattern streaks that starts to appear as the Bi_2Te_3 domains form, they are notably absent in freshly cleaved $Fe(Te, Se)$ RHEED (Figure 4.2.2 a). As the film grows thicker the RHEED pattern becomes brighter clearly showing the domains (Figure 4.2.3 a).

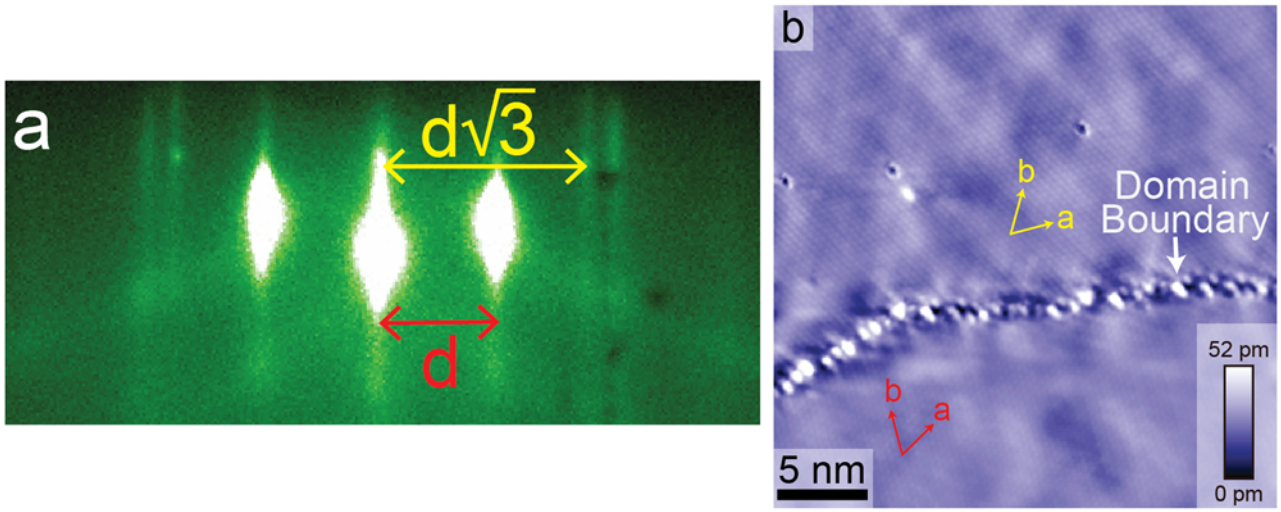

Figure 4.2.3: (a) RHEED image of a Bi_2Te_3 thin film grown on $Fe(Te, Se)$ showing the characteristic double line, the two different periodicities are marked with red and yellow arrows. (b) STM topograph of Bi_2Te_3 grown on $Fe(Te, Se)$ showing the location of a domain boundary.

These domains are a product of the mismatch between the Bi_2Te_3 film and the $Fe(Te, Se)$ substrate's crystal structure. $Fe(Te, Se)$ has a square lattice (Figure 4.1.1 b) but Bi_2Te_3 has a hexagonal crystal structure, but because Bi_2Te_3 has weakly bonded van der Waals layers it can be grown on a slew of mismatched substrates. This structural mismatch leads to the formation of domain boundaries that can be located on the films surface within the STM (Figure 4.2.3 b). Across these boundaries the crystal lattice is rotated 30° with respect to one another. These domains are smaller than the RHEED beam's spot size and therefore we see both hexagonal periodicities with every 30° rotation. The spacing between the two separate sets of lines are proportional to each other by a factor of $\sqrt{3}$. This comes from the geometry of a hexagonal lattice (Figure 4.2.3 a).

4.3 Characterization of Superconducting Bi_2Te_3 Thin Films

In this section, I will go over the STM characterization of our Bi_2Te_3 heterostructures grown on a $Fe(Te, Se)$ substrate. The films were grown by me in our home built MBE system and the STM

characterization was carried out by He Zhao, this work has been published [46].

To characterize this heterostructure we grew our Bi_2Te_3 films in a range of thicknesses down to a single quintuple layer (QL). When Bi_2Te_3 is only 1 QL thick the top and bottom surfaces hybridize, when it is greater than 2 QL thick the Dirac node should form [47]. We grew three different films 1 QL, 3 QL and 5 QL thick. We start with our 1 QL films to characterize the interface between the growth and substrate. On the surface of our 1 QL thick sample there are some small regions where we can locate the $Fe(Te, Se)$'s square lattice (Figure 4.3.1 b)

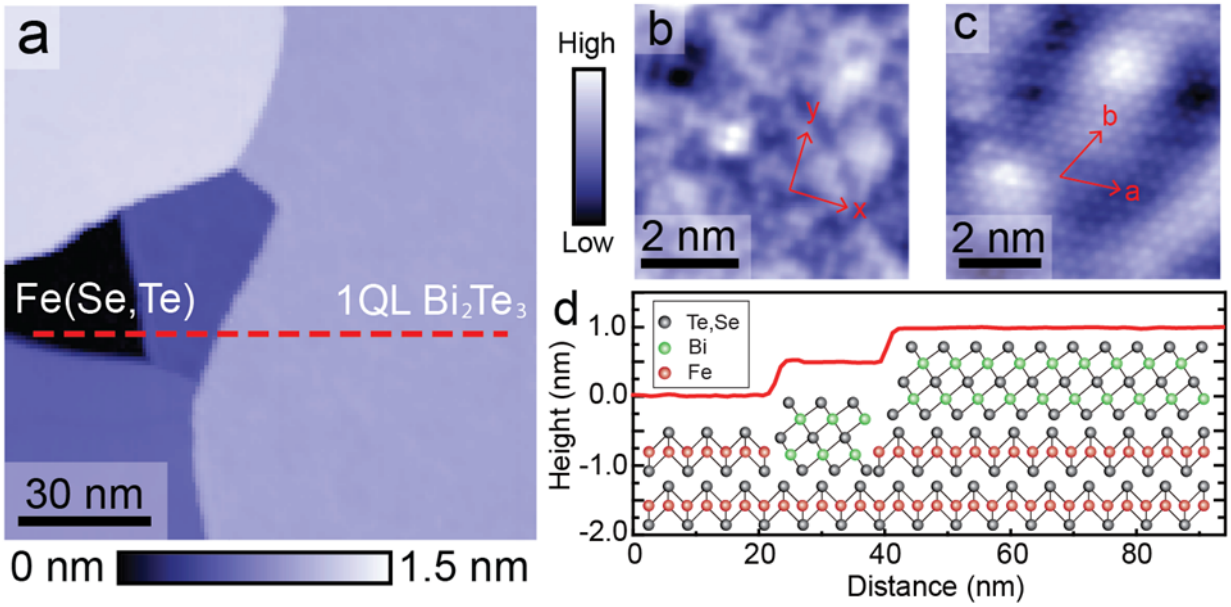

Figure 4.3.1: (a) Large scale STM topograph that has a region of exposed $Fe(Te, Se)$ substrate (b) that shows a square lattice and topmost Bi_2Te_3 (c) that shows a hexagonal lattice. (d) Height profile taken along the red dashed line in (a) showing a step height consistent with 1 QL of Bi_2Te_3 .

Taking a large scale topograph (Figure 4.3.1 a) lets us verify the single QL step height of ~1 nm (Figure 4.3.1 d). As mentioned in the previous section due to structural mismatch between the film and substrate we get inevitable domain formations (Figure 4.2.3). Despite these domains we are still able to find large single domain regions to scan (Figure 4.3.2).

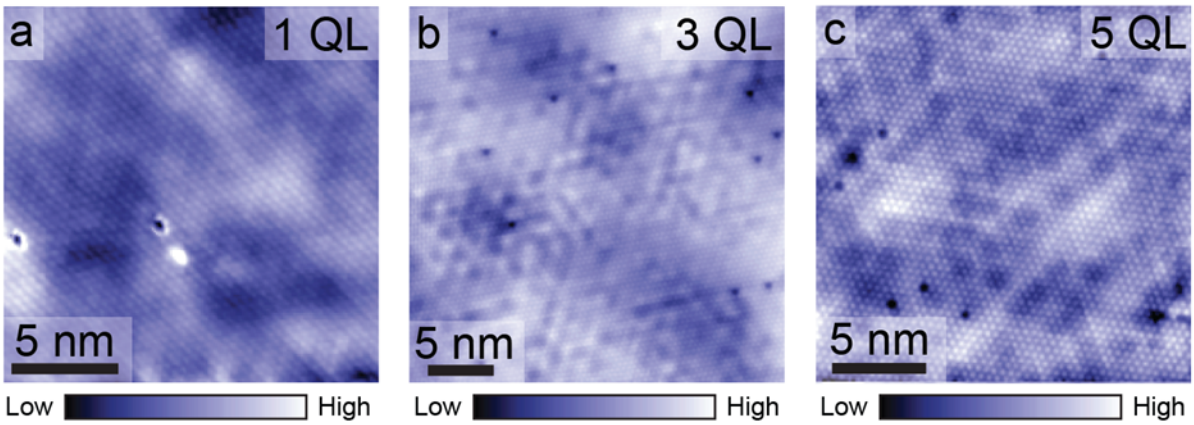

Figure 4.3.2: (a-c) STM topographs acquired on the surface of three different Bi_2Te_3 films grown on $Fe(Te, Se)$ (a) 1, (b) 3 and (c) 5 QL thick samples.

Next, in order to characterize the electronic structure we use quasiparticle interference to map out the dispersion of the Dirac surface state. We do this by acquiring a series of dI/dV maps at a constant bias voltage. On the surface of the sample electrons elastically scatter and interfere with themselves which creates standing waves in dI/dV measurements (Figure 4.3.3 a,b,c). Fourier transforming these dI/dV maps lets you pick out the dominant scattering vectors on the surface (Figure 4.3.3 e,f,g).

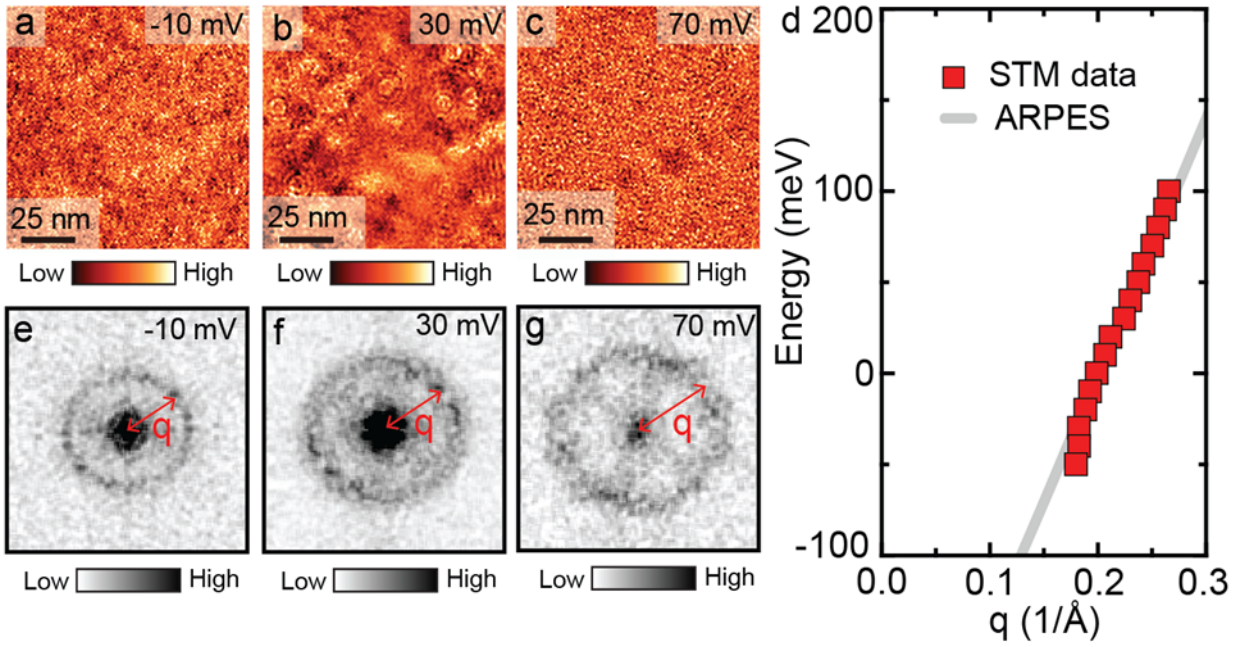

Figure 4.3.3: (a-c) dI/dV maps acquired over the same sample region with sample bias (a) -10 mV, (b) 30 mV and (c) 70 mV and (e-g) their respective Fourier transforms. (d) Extracted QPI dispersion from

our Fourier transformed dI/dV maps (red squares) compared to ARPES measurements of reference [47] (grey line).

Though we don't have direct access to the momentum information like ARPES, we are still able to measure the electron dispersion. We start with our single QL thick sample, and it indeed has a fairly linear dispersion that matches nicely with ARPES (Figure 4.3.3 d) [47]. We should note that for a single QL thick sample its top and bottom surfaces hybridize turning it into a trivial insulator [47], because of this we also measure the electron dispersion in thicker 3 QL and 5 QL samples. Our thicker films also show a linear dispersion that is consistent with ARPES (Figure 4.3.4 c,d).

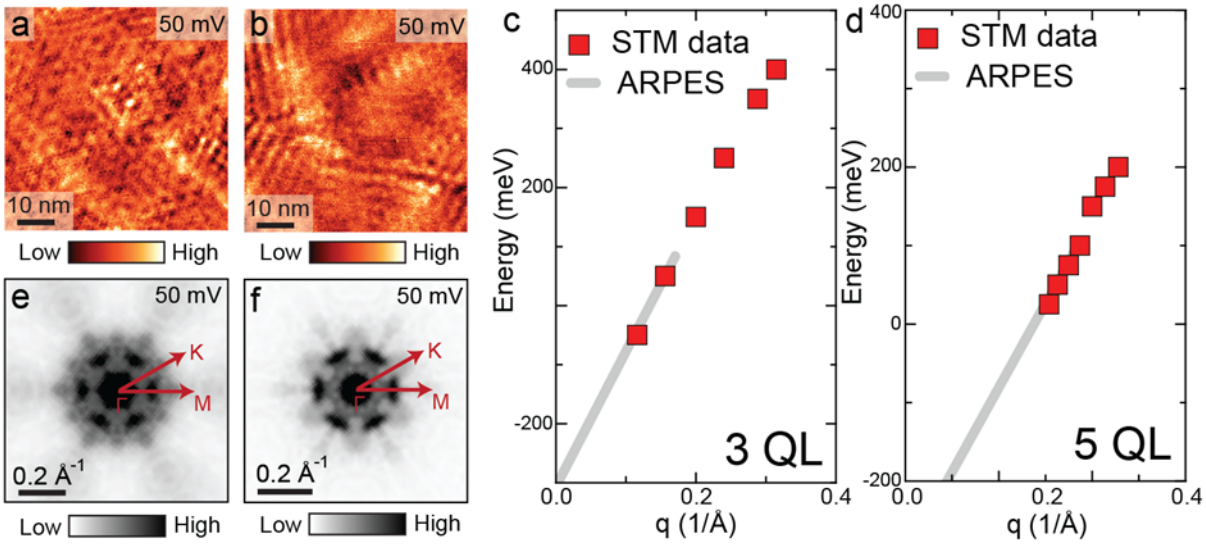

Figure 4.3.4: (a,b) dI/dV maps acquired on the surface of (a) 3 and (b) 5 QL thick films and (e,f) their respective Fourier transforms. (c,d) Extracted QPI dispersion from our Fourier transformed dI/dV maps (red squares) compared to ARPES measurements of reference [47] (grey line)

Both our 3 QL and 5 QL samples are thick enough such that there should not be any hybridization between the top and bottom surfaces. In ideal topological insulators back scattering is prohibited, but due to hexagonal warping of the constant energy contour additional scattering channels open up along the Γ-M direction [48, 49, 14] (Figure 4.3.4 e,f). In our thicker films we do indeed see this angular dependent QPI pattern (Figure 4.3.4 e,f), consistent with measurements on Bi_2Te_3 films [48, 49] and bulk single crystals [14]. This confirms the large scale electronic structure of our films.

Next we look for signs of superconductivity on the surface of our films. We start with our single QL film. Since the induced superconducting gap decreases the further you are from the interface [50], this

should in principle maximize our chances of detecting a gap on the surface our TI film. On the surface of our single QL film we see a clear gap measuring ~3.5 meV (Figure 4.3.5 a). This gap is significantly larger than those measured on monolayer $FeTe$ grown on Bi_2Te_3 of ~1 meV [51]. Additionally the coherence peaks are symmetric with respect to the Fermi energy consistent with a pairing-induced gap.

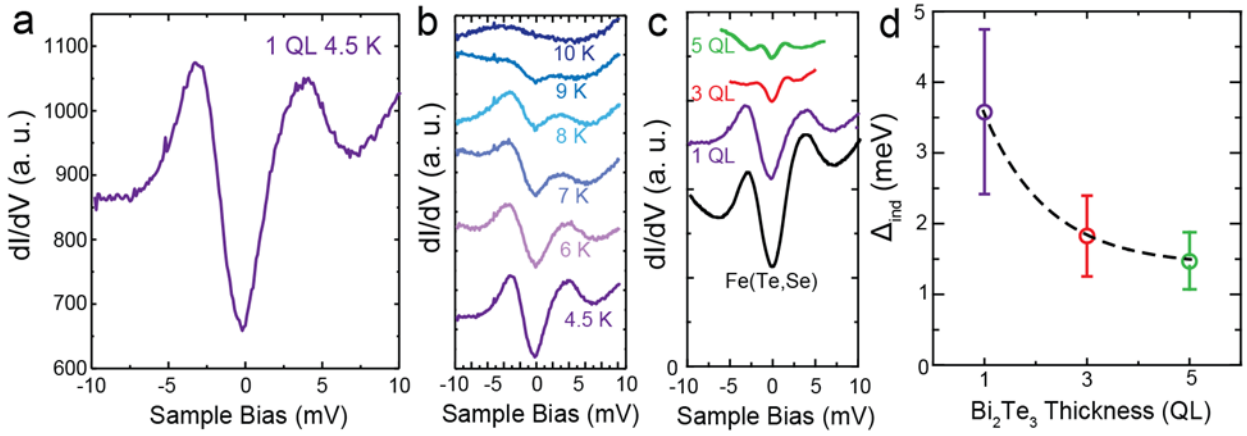

Figure 4.3.5: (a) Average dI/dV spectra acquired on the surface of 1 QL Bi_2Te_3 grown on $Fe(Te, Se)$ and (b) its temperature dependence. (c) Average dI/dV spectra acquired on different thicknesses of sample offset in energy for clarity. (d) Gap magnitude as a function of sample thickness showing an exponential decay.

Next we acquired average dI/dV spectrums for our single layer film at different temperatures over the sample region. As the sample heats up the gap vanishes at around 10 K (Figure 4.3.5 b). Although our measured T_c is smaller than that of our bulk $Fe(Te, Se)$ of ~14 K, this is likely due to the local variations of the superconducting properties of the $Fe(Te, Se)$ substrate [52]. On the surface of our thicker 3 QL and 5 QL films our measured gaps are ~1.8 meV and ~1.5 meV respectively (Figure 4.3.5 c). This trend is consistent with theoretical calculations [50] and measured decay rates on Bi_2Te_3 /$NbSe_2$ superconducting heterostructures [53] (Figure 4.3.5 d).

To obtain further evidence that the measured gap is indeed of superconducting origins, we investigated the dependence of our dI/dV spectra as a function of applied magnetic fields. When a type-II superconductor is placed in a magnetic field whose magnitude is below some upper critical value H_{c_2}, the magnetic field will penetrate the sample creating magnetic vortices. If the surface of our Bi_2Te_3 is a type-II superconductor like our $Fe(Te, Se)$ substrate we would expect to Abrikosov vortices as dark regions in our dI/dV maps acquired at biases near the superconducting gap energy [54]. Figure 4.3.6 shows a series a of dI/dV maps taken over the same region of our single QL film with an ~3 meV

applied bias and varying magnetic field strength.

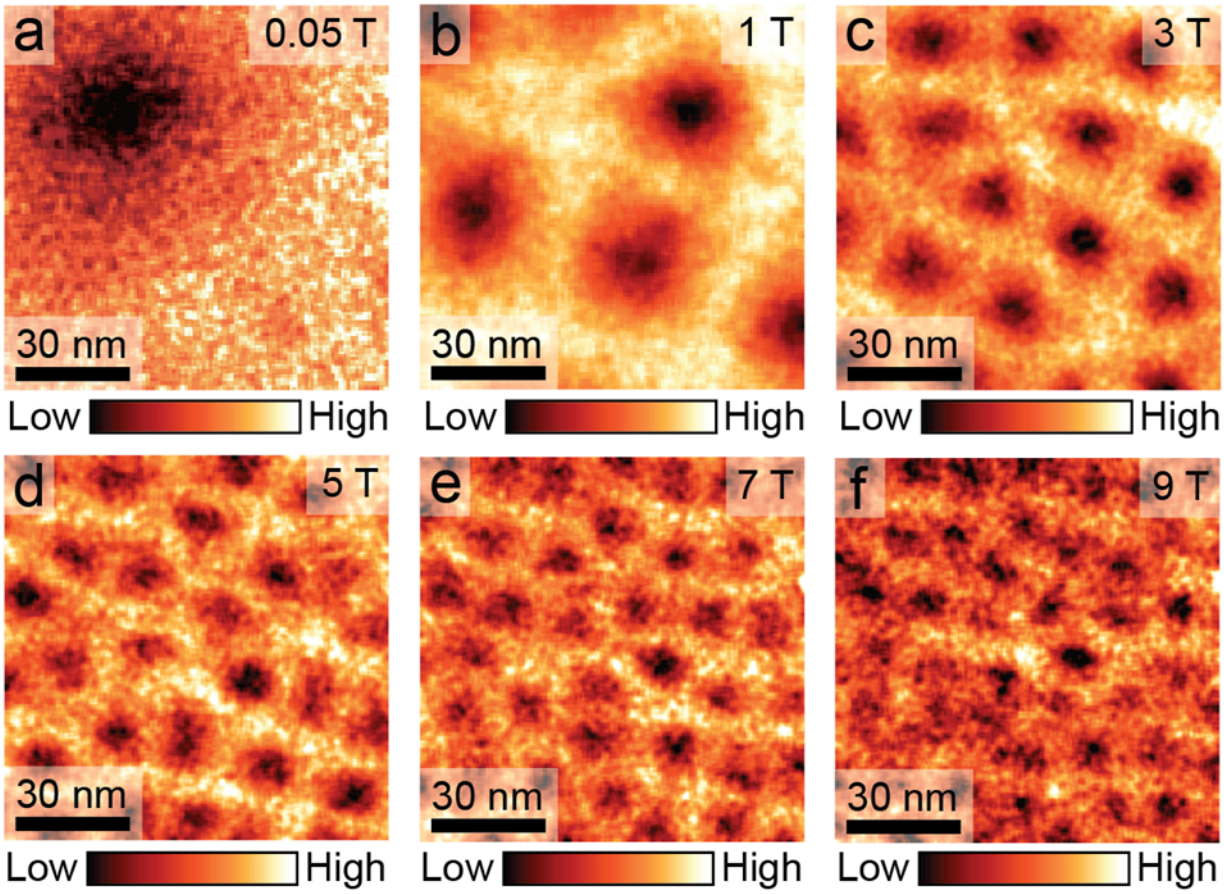

Figure 4.3.6: (a-f) dI/dV maps acquired with an applied sample bias of -3 mV over the same region of the sample in figure 4.3.3 b with different magnitudes of magnetic field applied out of plane (a) 0.05 T, (b) 1 T, (c) 3 T, (d) 5 T, (e) 7 T and (f) 9 T. Each dark region represents a single vortex core, and the vortex lattice can be seen with our largest applied field.

Each of our dI/dV maps shows a clear vortex lattice that persists to much higher fields compared to Bi_2Te_3 /$NbSe_2$ heterostructures [21]. This is consistent with the $Fe(Te, Se)$ class of materials having extremely high upper critical field values [55]. Additionally taking a line cut of the spectrum shows a suppression of the gap edges as we move inside the vortex core, confirming the superconducting origin of the gap (Figure 4.3.7).

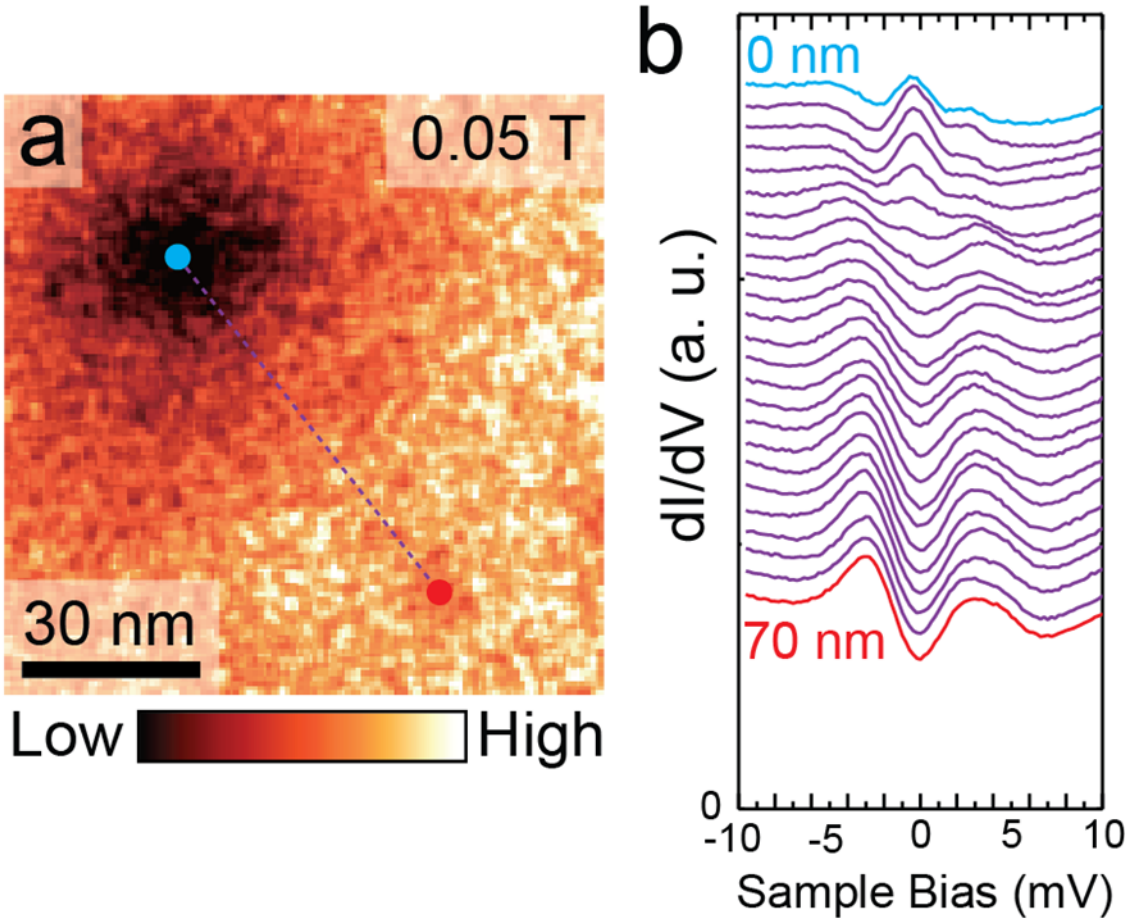

Figure 4.3.7: (a) dI/dV map showing a large magnetic vortex and (b) 70 nm line cut of the dI/dV spectra taken from inside the vortex core (blue) to 70 nm away from the core (red).

We note that none of our spectra show a flat bottom reaching zero conductance around the Fermi level, like an ideal s-wave BCS function should [56]. This could be due to localized incoherent states around the Fermi energy arising from things such as impurities. Previous Bi_2Te_3 /$NbSe_2$ experiments attributed this to the emergence of topological surface states in their thicker films [53], but this is unlikely as we measured some residual conductance even in our 1 QL film whose Dirac node has not yet formed.

Now that we have verified the nature of the induced gap, we proceed to look for evidence of whether or not this superconductivity has been induced in the surface state. We do this acquiring dI/dV maps in small increments around the Fermi level, if a gap in the surface state exists we should not have a very strong QPI signature. We start with our single layer film, where the only band that should cross the Fermi level is the surface state band. At energies outside the gap range Fourier transformed dI/dV maps (Figure 4.3.8 b red and purple insets) show a clear QPI pattern qualitatively similar to those at

larger biases (Figure 4.3.3 e-g).

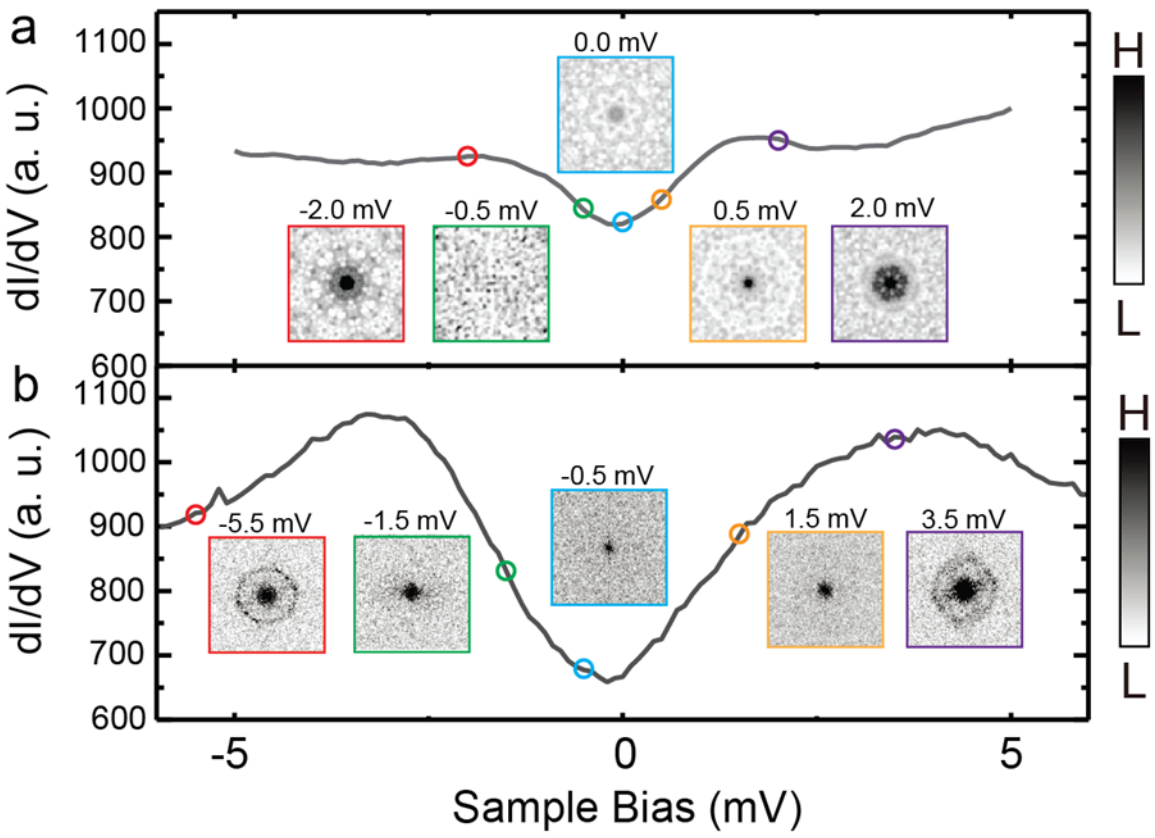

Figure 4.3.8: (a,b) Average spectra for our (a) 3 QL and (b) 1 QL thick samples, inset Fourier transforms show the QPI signal inside the gapped regions (green, blue and yellow) and outside the gapped region (red and purple).

However as we tune into the energy range of the gap, the QPI single becomes significantly suppressed (Figure 4.3.8 b green, blue and yellow insets). Similar to our 1 QL thick Bi_2Te_3 film we also see a strong suppression of the QPI in our thicker 3 QL film as well (Figure 4.3.8 a). Our data at the time presented the first microscopic visualization of a fully gapped surface state of Bi_2Te_3 arising from proximity induced superconductivity. One of the major goals for realizing topologically superconducting systems, is that they are said to host Majorana zero modes inside their magnetic vortex cores [17]. The key signature of these Majoranas is a peak at zero energy in the density of states. As you move away from the vortex core this peak should not split in energy [23, 57] unlike the bound states found in conventional superconductor vortices [58]. This key signature has been observed in Bi_2Te_3 films grown on $NbSe_2$ when the thicknesses is greater than 3 QL, but in thinner films it is notably absent due to hybridization of the top and bottom surfaces [23]. In our experiments we did observe this peak

at zero bias in our thinnest 1 QL film, but interestingly it does not seem to split in energy as we move away from the vortex core (Figure 4.3.7 b). Though this is the key signature of a Majorana bound state further spin-polarized tunneling measurements are necessary to uncover the origins of the peak [20]. Additionally pristine $FeTe_{0.55}Se_{0.45}$ also been observed to contain bound states inside of vortex cores [59]. It is also possible that the observed bound states are from the $Fe(Te, Se)$ substrate rather than the Bi_2Te_3 film.

Our results offer a promising pathway to study topological superconductivity with higher T_c . Iron based superconductors can be used to induce much larger gaps in the topological surface states than their low T_c counterparts. These larger gaps in turn allow much greater energy resolution for studying the emergent in-gap states. Other iron based superconductors can be used to push this experiment to pretty high temperature limits. For example you could use single-layer $FeSe$ grown on $SrTiO_3$ as a substrate, which offers a ~5 times larger gap [42], and a ~8 times greater T_c [41] than $Fe(Te, Se)$. This work offers a viable platform for exploring topological superconductivity without requiring millikelvin temperatures.

4.4 Synthesis of $SnTe$ Thin Films on $Fe(Te, Se)$

The previous section covered the growth and characterization of proximity induced superconductivity for the a $Bi_2(Te, Se)_3$ material class. Another subclass of the topological insulator is the topological crystalline insulator (TCI). Similar to $Bi_2(Te, Se)_3$ they have metallic surface states, except the TCI's surface states arise due to the symmetry of the crystal lattice [60]. At the time of conducting this experiment only one TCI class based on the rock salt crystal structure of $(Pb, Sn)Te$ and $(Pb, Sn)Se$ had been predicated [15] and experimentally realized [61, 16, 62, 63]. If a TCI undergoes a superconducting phase transition theory predicts that a new type of topological superconductivity can arise [64, 18, 65, 66] that is different than proximitized $Bi_2(Te, Se)_3$ materials [67, 38, 21, 23, 53, 24, 46]. Predictions such as multi Majorana zero modes inside single magnetic vortices [18] and tunable Andreev bound states [19] have ignited considerable interest in experimentally realizing this system. The main issue that has hindered STM studies has been the fabrication of high quality superconducting TCI surfaces. Past work on achieving superconductivity in a TCI has used doping [68] similar to how doping has also been used to make superconducting Z_2 TIs [69]. Even though there is additional disorder from the doping the topological nature of the surface state still persists [70, 71, 72]. On the other hand, this disorder makes it much more difficult to obtain a flat clean surface by cleaving. This has hindered STM from being used to study the superconducting TCI phase on the nanoscale. Similar to our previous work on Bi_2Te_3 [46] the proximity effect could be a way to realize topological superconduc-

tivity without the addition of disorder [37]. Previous work on proximitized TCIs has shown promising results [73], but the difficulty lies with fabricating a clean interface for the TCI/superconductor heterostructure. This difficulty arises from $(Pb, Sn)Te$ and $(Pb, Sn)Se$ having much stronger covalent bonds unlike $Bi_2(Te, Se)_3$ whose layers are weakly van der Waals bonded. This significantly limits which superconducting substrates can be used, requiring a much closer lattice match at the interface [74, 75]. In this work we fabricated heterostructures for the purpose of realizing topological crystalline superconductivity in prototypical TCI $SnTe$, by employing the use of a buffer layer.

Similar to our work on Bi_2Te_3 we picked $FeTe_{0.55}Se_{0.45}$ as our superconductor because of its high T_c ~14.5 K and s-wave pairing symmetry. Unlike Bi_2Te_3 that can be grown on a multitude of structurally mismatched substrates [76, 21]. TCI films such as $SnTe$ are much more prone to warping and straining [77, 78, 79] which could affect the topological surface states. This means we must have a close lattice match for our substrate. $Fe(Te, Se)$ cleaves along the (001) direction and has a square lattice constant of ~3.9 Å (Figure 4.4.1 b), while $SnTe$ also has a square lattice, its lattice constant is ~6.3 Å this makes their mismatch almost 50% making their interface highly incompatible. $SnTe$ when grown along the (111) direction it has an in plane lattice constant of ~4.4 Å and has a only 1.7% lattice mismatch to the lattice constant of Bi_2Te_3 [75]. In order to bridge this structural mismatch we use a single Bi_2Te_3 buffer layer (Figure 4.4.1 a), which from our previous work we know can grow just well on an $Fe(Te, Se)$ substrate with domains (Figure 4.2.3).

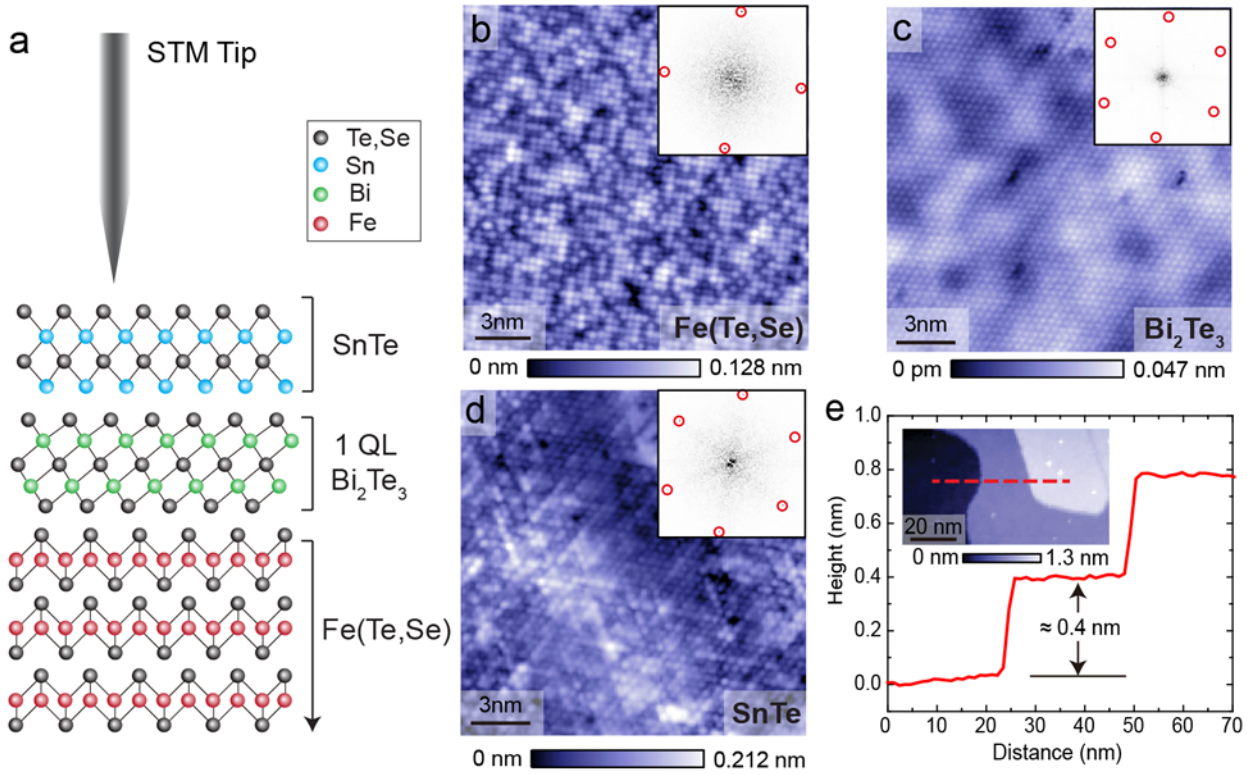

Figure 4.4.1: (a) Schematic of $SnTe/Bi_2Te_3$ $/Fe(Te,Se)$ heterostructure grown in this experiment. (b-d) STM to topographs showing (b) exposed $Fe(Te,Se)$ substrate, (c) 1 QL Bi_2Te_3 buffer layer and (d) topmost $SnTe$ layer (insets are Fourier transforms of the topographs red circles denote the Bragg peaks). (e) Height profile taken along the red dashed line in the inset topograph, the step height is consistent with consecutive bilayers of $SnTe$.

For this experiment we grew three different samples labeled samples A, B and C and were nominally 3, 6 and 14 bilayers (BL) thick respectively (Figure 4.4.2).

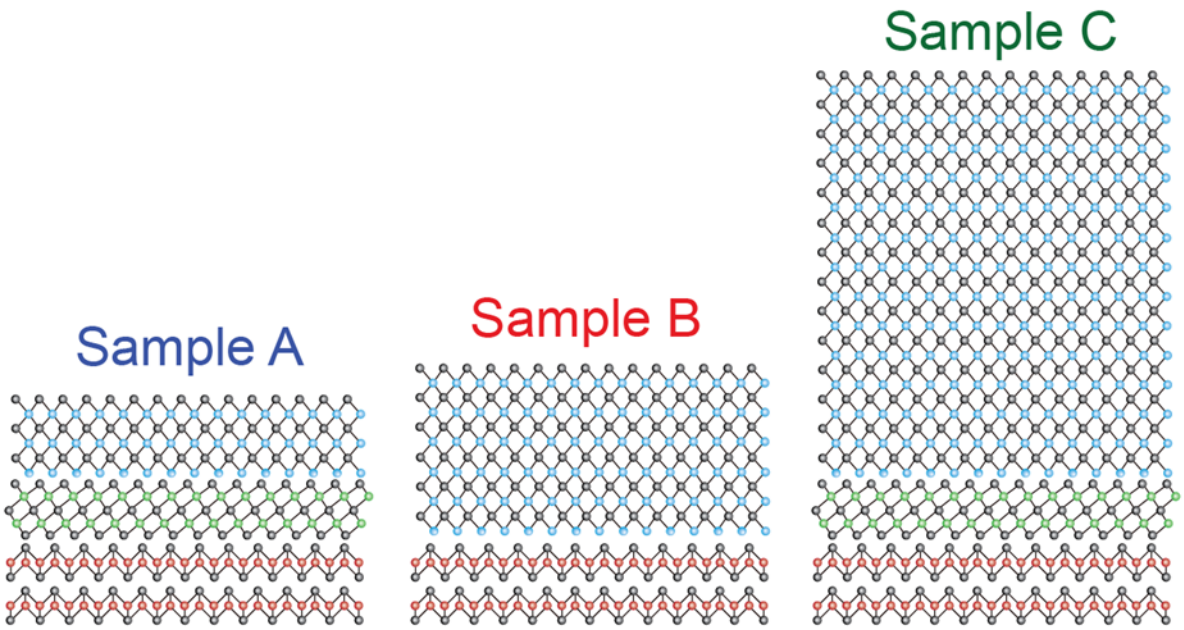

Figure 4.4.2: Side view the three different samples that were analyzed in this experiment, labeled samples A, B and C. Sample A is nominally 3 bilayers (BL) $SnTe$ with a Bi_2Te_3 buffer layer, sample B is nominally 6 BL $SnTe$ without a buffer layer and sample C is nominally 14 BL of $SnTe$ with a Bi_2Te_3 buffer layer.

For all the samples, we start with optimally doped $Fe(Te, Se)$ T_c ~14K that were grown using the self-flux method and cleaved it in vacuum to expose a clean lattice of square atoms (Figure 4.4.1 b). We next obtain a RHEED image that shows the characteristic pattern we expect for $Fe(Te, Se)$ (Figure 4.4.3 a). We next grow a single quintuple layer of Bi_2Te_3 to act as our buffer layer (Figure 4.4.3 b). After the buffer layer is formed we then grow our $SnTe$ layers on top, the $SnTe$ RHEED matches the Bi_2Te_3 only brighter in intensity (Figure 4.4.3 c). The buffer layer was grown at 200 °C, 250 °C and 180 °C for samples A,B and C respectively. While the $SnTe$ layers were growth at 300 °C for both A and B and 180 °C for sample C. The (Bi,Sn):Te flux ratio was kept at 1:10 for all the growth. Sample A was not annealed post growth while samples B and C were annealed at 320 °C and 270 °C respectively. This higher temperature annealing had unintended consequences for sample B, that being its Bi_2Te_3 buffer layer had seemly evaporated away.

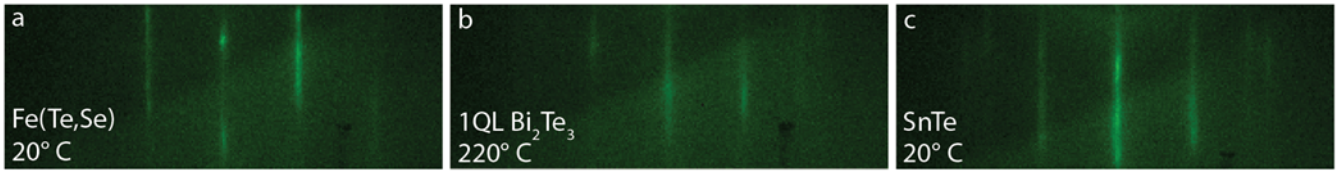

Figure 4.4.3: Typically, we can locate a region of our sample where we can see the interface between our growth and substrate. For sample B we could never locate our Bi_2Te_3 buffer layer despite being able to see $Fe(Te, Se)$ substrate (Figure 4.4.4 a). The step heights were consistent with our growth if the Bi_2Te_3 buffer layer did indeed evaporate away (Figure 4.4.4 b).

Typically we can locate a region of our sample where we can see the interface between our growth and substrate. For sample B we could never locate our Bi_2Te_3 buffer layer despite being able to see $Fe(Te, Se)$ substrate (Figure 4.4.4 a). The step heights were consistent with our growth if the Bi_2Te_3 buffer layer did indeed evaporate away (Figure 4.4.4 b).

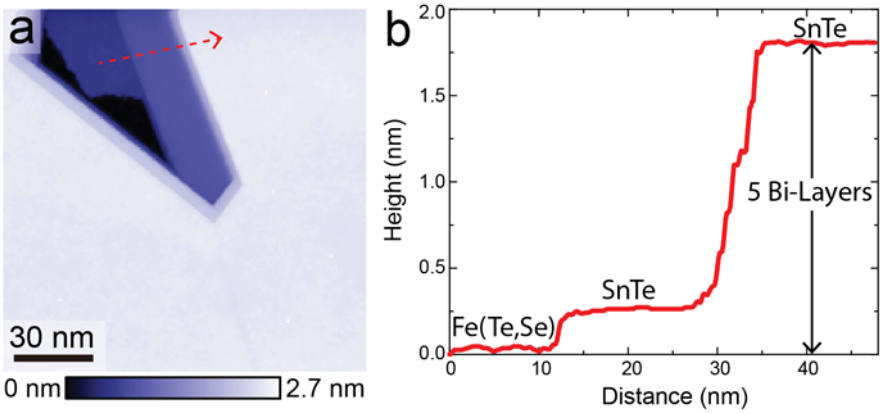

Figure 4.4.4: (a) Large-scale STM topograph of Sample B showing how the thickness of this sample was determined. (b) Topographic height as a function of distance along the red dashed arrow in (a).

We further verify that this is the case by monitoring the Bi_2Te_3 buffer layer's RHEED pattern as we anneal it at higher temperatures. At 250 °C the characteristic domain RHEED pattern for 1 QL of Bi_2Te_3 does not change (Figure 4.4.5 b,j). As we heat it up 320 °C the RHEED image starts to fade in intensity and the domain lines start to disappear (Figure 4.4.5 c,k).

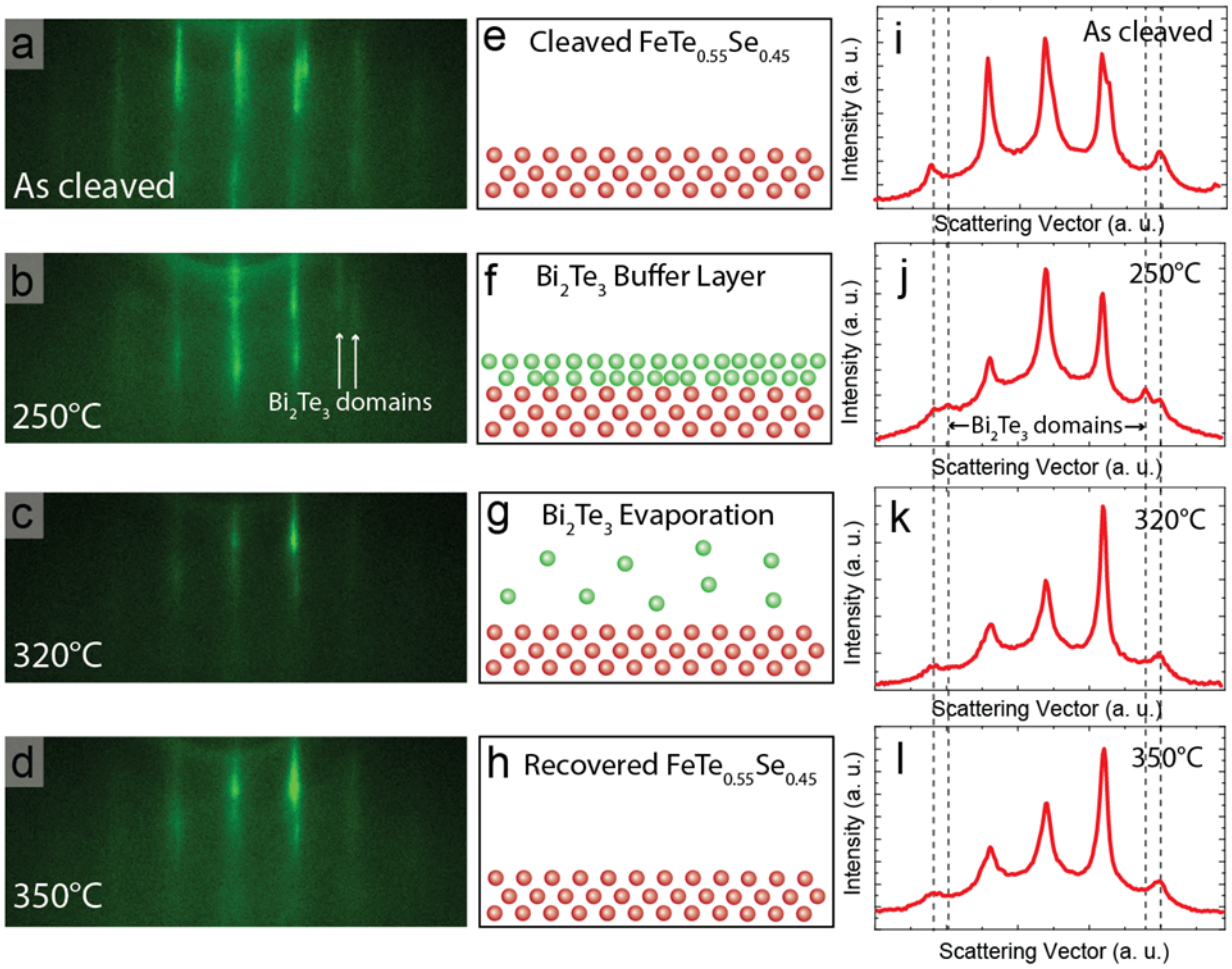

Figure 4.4.5: (a-d) RHEED images demonstrating the removal of a Bi_2Te_3 buffer layer from a $Fe(Te, Se)$ substrate. (a) RHEED image on as cleaved $Fe(Te, Se)$, (b) RHEED image after growing a single Bi_2Te_3 buffer layer at 250 °C, (c) RHEED image after heating the heterostructure to 320 °C and (d) RHEED image after heating to 350 °C. (e-h) Schematic depiction of the Bi_2Te_3 /$Fe(Te, Se)$ interface observed in RHEED images (a-d). (i-l) Intensity line profiles taken across the RHEED images (a-d) demonstrating the appearance of the Bi_2Te_3 domains in (b) and disappearance in (k) and (l).

This method of evaporating the buffer layer was similarly used in previous experiments as well to engineer complicated interfaces [80].

Within our STM we are able to locate regions of our sample that show a hexagonal $SnTe$ lattice that is consistent with those reported in previous experiments [75]. Additionally the $SnTe$'s topographs are bias dependent and become more electronically inhomogeneous at higher biases (Figure 4.4.6). They also show a clearly different surface than our Bi_2Te_3 buffer layer making it very easy to distinguish between the two (Figure 4.4.1 c,d).

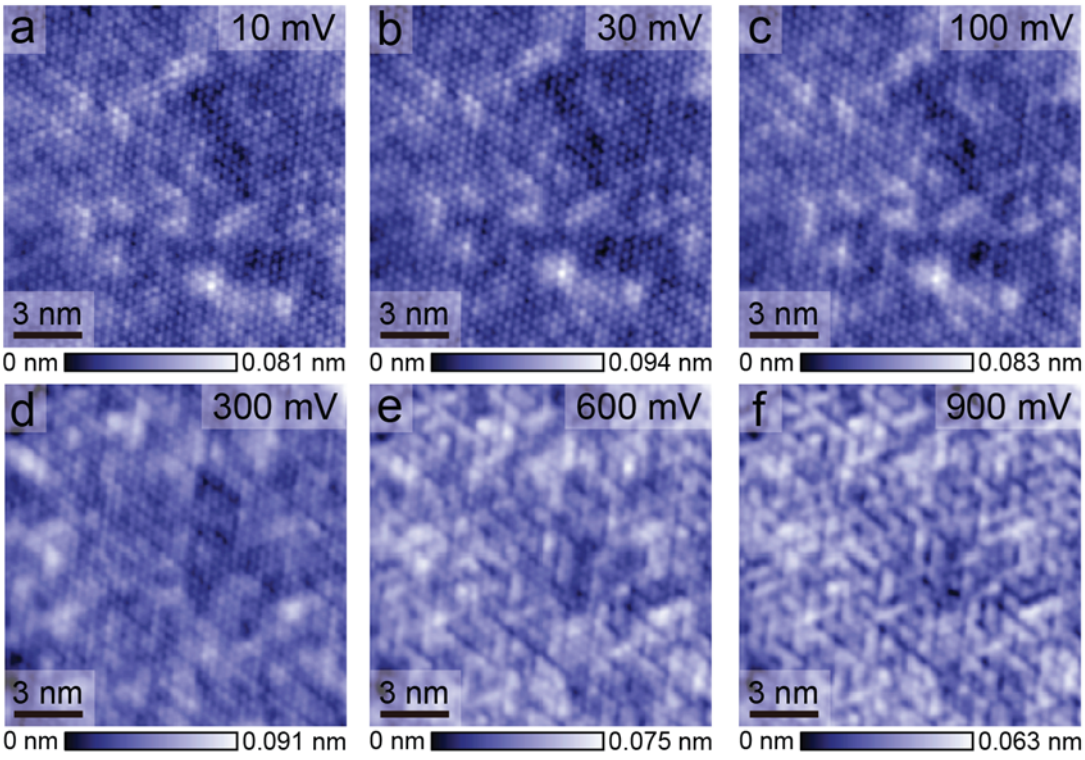

Figure 4.4.6: (a-f) STM topographs acquired of the same region of Sample C with applied bias (a) 10 mV, (b) 30 mV, (c) 100 mV, (d) 300 mV, (e) 600 mV and (f) 900 mV.

Additionally, the step height between consecutive layers is ~0.4 nm, which matches the height of a single bilayer of $SnTe$ along the (111) direction (Figure 4.4.1 e).

4.5 Characterization of Superconducting TCI films

To characterize our heterostructures we employ the use of scanning tunneling spectroscopy. We start by acquiring dI/dV spectra on all three of our samples across a wide energy range (Figure 4.5.1). From our measurements we are we are able to estimate the position of the valence band top (VBT). The top of the valence band occurs when there is a sharp increase in the differential conductance at the negative energies (Figure 4.5.1).

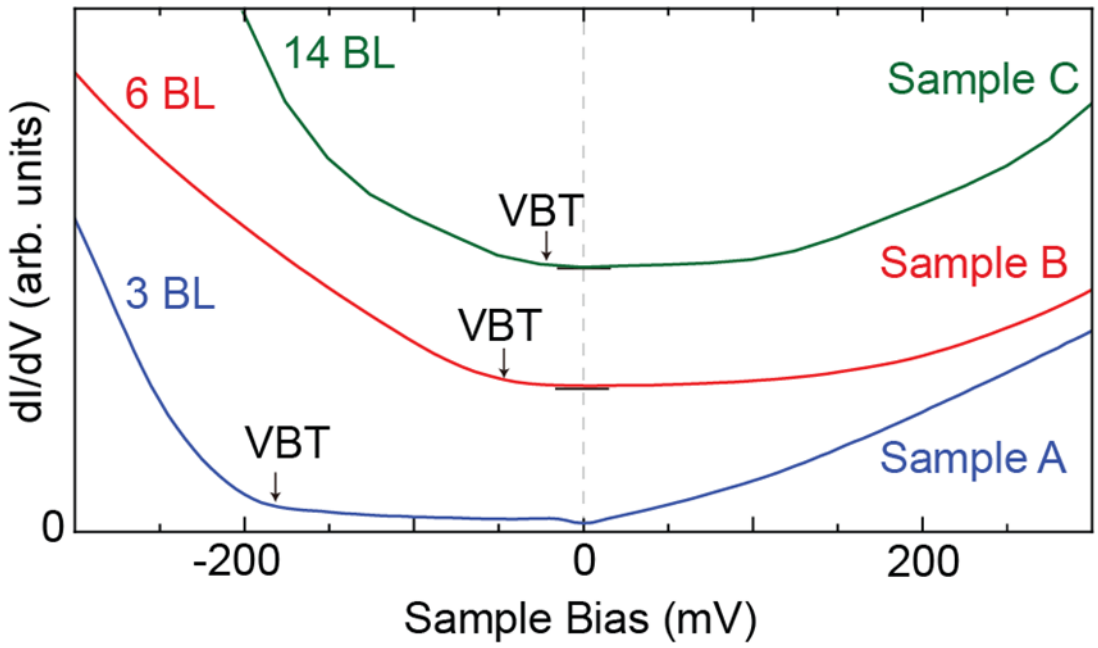

Figure 4.5.1: Long range dI/dV spectra on our three different sample sample A (blue) sample B (red) and sample C (green). The arrow labeled VBT denotes the approximate position of the top of the valence band.

As the thickness of our film increases from samples A to C, the Fermi level shifts down closer to the VBT. In our thickest film the VBT is just slightly above our Fermi level. This is consistent with the existence of surface states spanning the Fermi level. $SnTe$'s (111) surface state consists of a Dirac cone at the Γ point with additional Dirac cones at each of the M points, these two cones are slightly offset in energy [81]. This surface states structure will lead to three dominant scattering vectors, illustrated in figure 4.5.2 a.

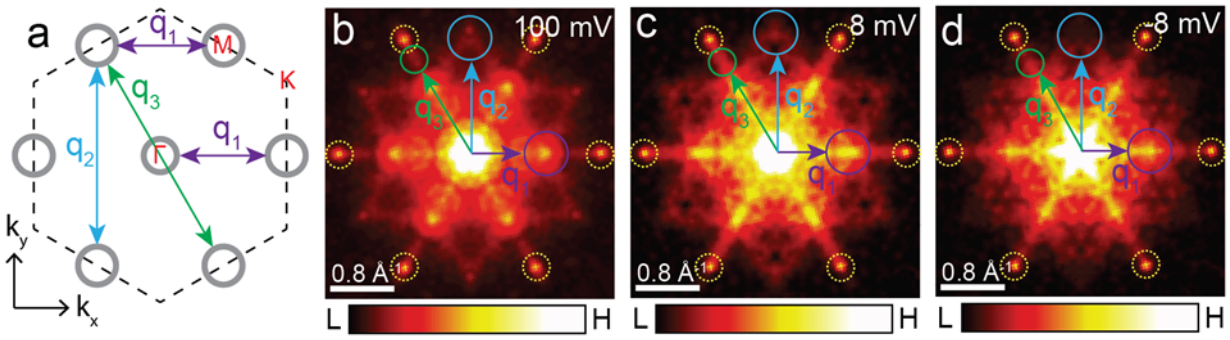

Figure 4.5.2: Quasiparticle interference imaging of the $SnTe$ (111) surface sample C and (a)

schematic of its constant energy contour where q_1 (purple), q_2 (blue) and q_3 (green) denote the dominant scattering vectors. (b-d) Fourier transformed dI/dV maps acquired at (b) 100 mV, (c) 8 mV and (d) -8 mV. The peaks in the Fourier transforms (b-d) circled in purple, blue and green correspond to their respective scattering channels in (a).

Using quasiparticle interference imaging we are able to detect signatures from all three of the scattering channels (Figure 4.5.2 b,c,d). These QPI scatting vectors are consistent with the existence of a Dirac surface state in all three of our samples. Similarly to our Bi_2Te_3 $/Fe(Te,Se)$ samples hybridization of the top and bottom surfaces could lead to a gap opening at the Dirac point, but for $SnTe$ the surface state remains intact for a wide range of thicknesses [82].

After verifying the large scale electronic structure of our films, we next look for signs of induced superconductivity. We start with our thinnest sample, sample A which consists of a single QL of Bi_2Te_3 and 3 BL of $SnTe$ on top. On our topmost surface we see a prominent spectral gap that is symmetric across the Fermi level (Figure 4.5.3 a) that is also spatially uniform (Figure 4.5.3 c). If we increase the temperature the gap disappears at ~12 K (Figure 4.5.3 b) which is consistent with the bulk transition temperature of our $Fe(Te,Se)$ substrate.

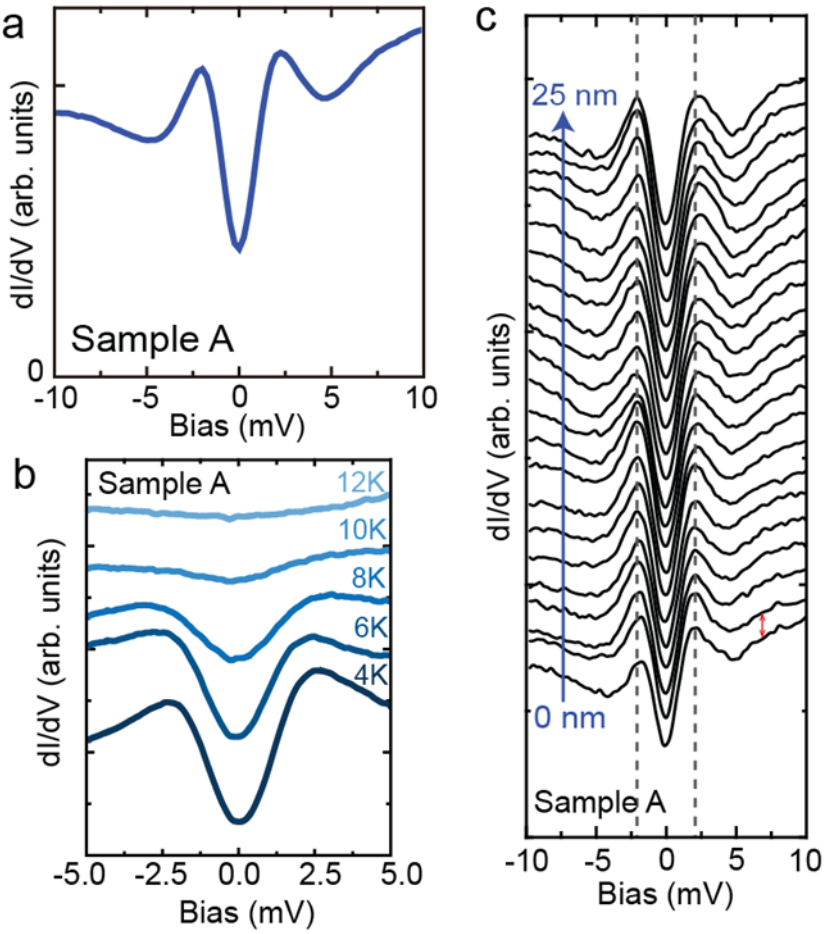

Figure 4.5.3: (a) Average dI/dV spectra acquired on the surface on sample A and (b) its temperature dependence. (c) 25 nm line cut taken across the surface of sample A showing the gap to be spatially homogenous.

We fit each of the spectra in figure 4.5.3 b to a thermally broadened BCS function [56] (Figure 4.5.4), which is in good agreement with our experimental data. The extracted gap magnitudes closely follow a BCS trend (Figure 4.5.4 e).

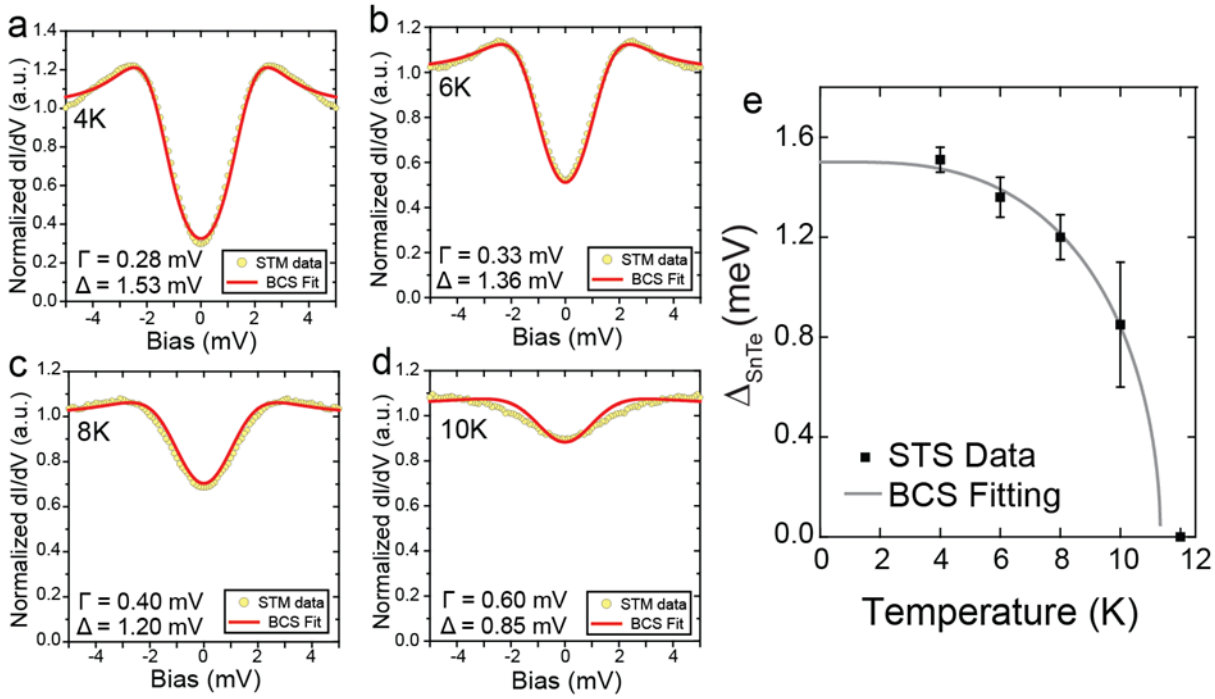

Figure 4.5.4: (a-d) Average dI/dV spectra of sample A acquired at different temperatures and symmetrized around the Fermi level (yellow points) and the s-wave BCS spectral function fit (red line). (e) Spectral gap extracted from (a-d) as a function of temperature.

Differential conductance maps acquired on the surface of sample A and B show a prominent spectral gap symmetric around the Fermi level in the density of states (Figure 4.5.6 a,b), both these samples are of comparable thickness. Since sample A and B's surface is a similar distance from the $Fe(Te, Se)$ substrate these variations could be due to different STM tips, as well as variations in the Sn:Te ratio. Additionally $Fe(Te, Se)$'s excess interstitial iron varies across different $Fe(Te, Se)$ substrates [83, 84, 85].

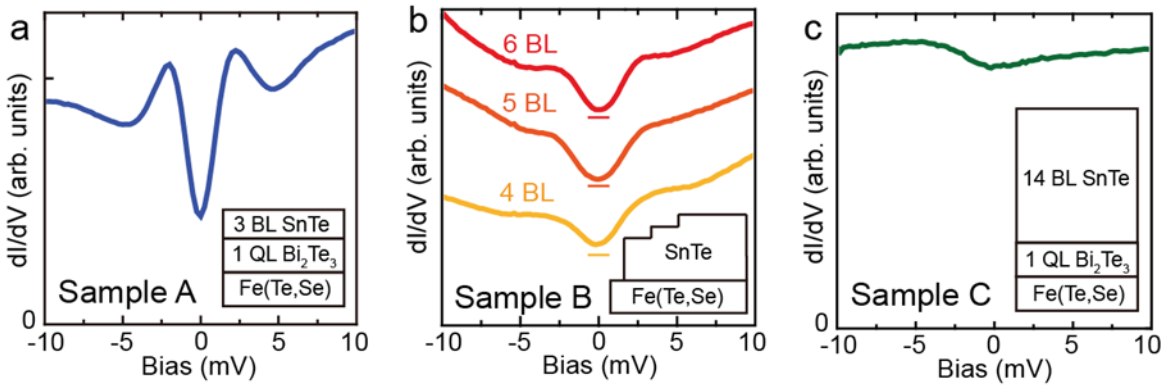

Figure 4.5.5: (a-c) Average dI/dV spectra acquired on the surface of (a) sample A (c) and sample C (c), and (b) dI/dV spectra acquired on multiple terraces of sample B offset for clarity. The insets in the lower right are schematics of each samples heterostructure

Our much thicker sample C only shows a small suppression in the density of states around the Fermi level (Figure 4.5.5 c). This would be consistent with the expected trend of proximity induced superconductivity, where the superconducting gap decays with increasing sample thickness [50]. $Fe(Te, Se)$ also has a relativity short coherence length [67, 83], so this could also be a possible explanation for the quick suppression of the gap.

Lastly, we use spectroscopic STM imaging to spatially map the differential conductance with an applied perpendicular magnetic field. Since our $Fe(Te, Se)$ substrate is a type-II superconductor we would expect the superconductivity on the surface of our samples to also be type-II. When a type-II superconductor is subjected to a magnetic field, the magnetic field will penetrate the sample in quantized vortices. If our $SnTe$ heterostructures are indeed superconductive, we would expect to observe Abrikosov vortices as localized regions of low conductance in our dI/dV measurements acquired at bias of superconducting gap [54]. We acquired a series of dI/dV at 1 T, 2 T and 4 T over the same region of the sample and a clear vortex lattice can be observed (Figure 4.5.6).

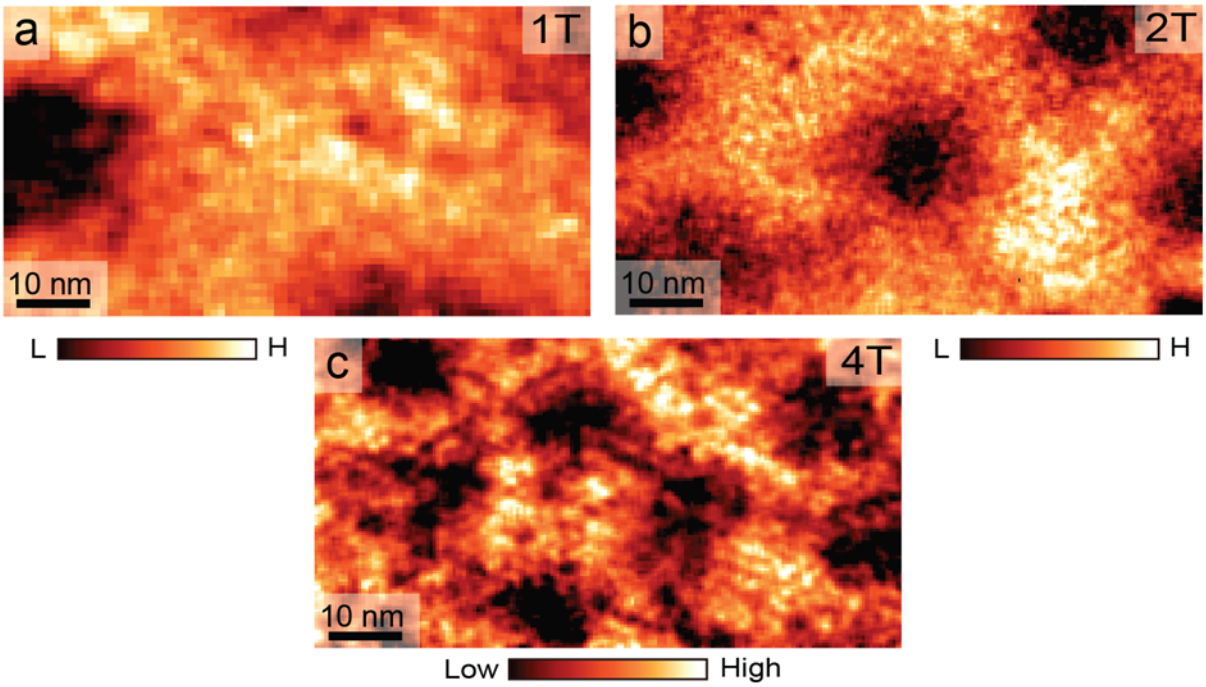

Figure 4.5.6: (a-c) dI/dV maps acquired of the same region of the sample with an applied magnetic field out of plane of magnitude (a) 1 T, (b) 2 T and (c) 4 T.

The number of vortices increases with magnetic field strength further confirming that the gap measured on the surface of our $SnTe$ (111) films is indeed a superconducting one. Most importantly, this superconducting gap is larger and persists to higher temperatures than proximity induced TCI experiments using lower T_c s-wave superconductors [73]. Interestingly spectroscopic measurements around the vortex core not only show the expected suppression of the coherence peak, but intriguingly possess a peak centered at zero energy inside the vortex core (Figure 4.5.7).

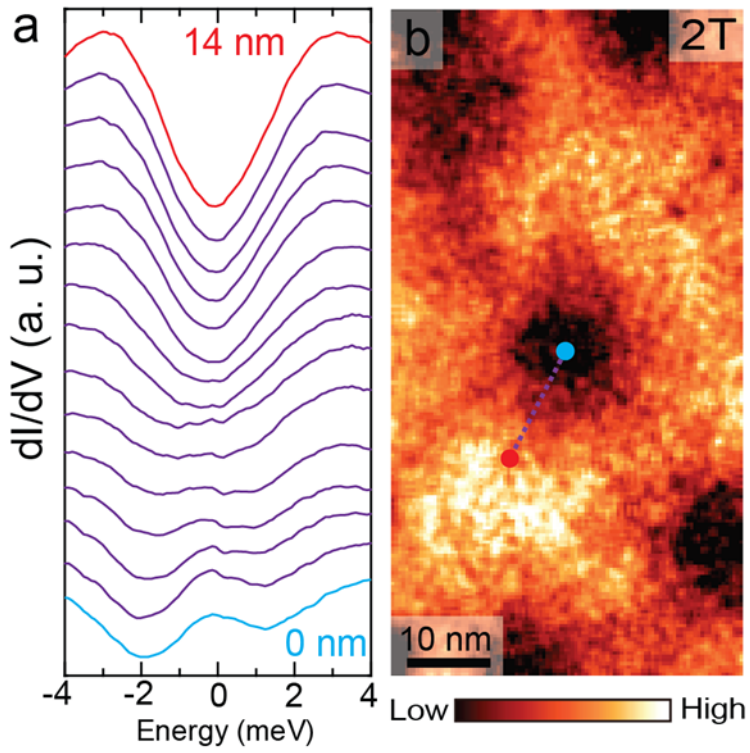

Figure 4.5.7: (a) Radially averaged dI/dV spectra 14 nm line cut taken from inside the vortex core (blue) to 14 nm outside (red) taken in the region denoted in (b) by the purple dashed line.

Similar zero bias conductance peaks have been reported in numerous other systems as well. For example some fraction of the vortices on the bare surface $Fe(Te, Se)$ (Figure 4.5.8 a) [86] as well as on its surface iron impurities [57] have shown these zero bias conductance peaks.

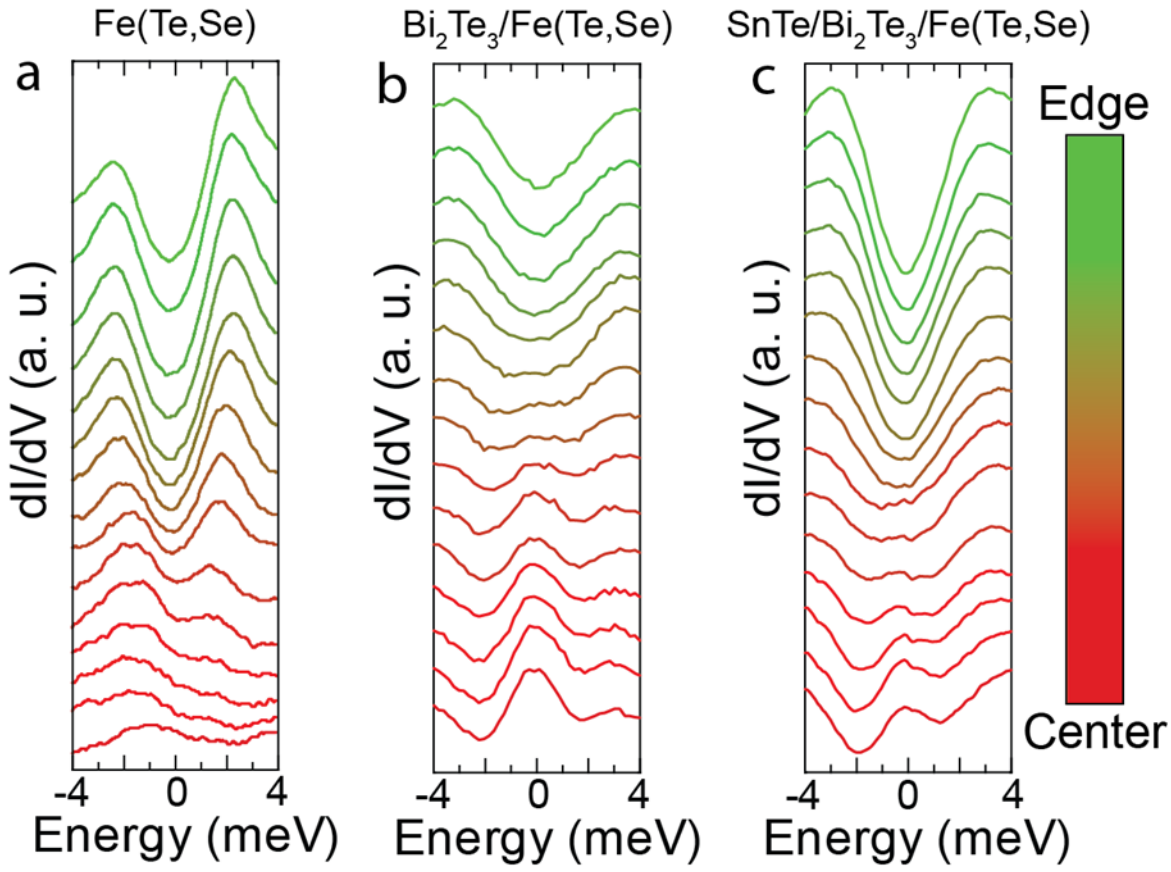

Figure 4.5.8: (a-c) dI/dV spectra line cuts taken from the center of a magnetic vortex core (red) out towards the edge (gree) acquired on (a) as-cleaved $Fe(Te, Se)$ (measurements from reference [86]), (b) the surface of 1 QL Bi_2Te_3 grown on $Fe(Te, Se)$ (Figure 3.3.7 [46]) and (c) our sample A $SnTe$ (111) heterostructure surface.

In addition to $Fe(Te, Se)$, Bi_2Te_3 grown on $Fe(Te, Se)$ also shows this peak at zero conductance inside a vortex core [67] (Figure 4.5.8 b). Interestingly the zero bias peak measured on the surface of our $SnTe$ (111) samples (Figure 4.5.8 c) is distinctly different from those reported on $Fe(Te, Se)$ [86] and Bi_2Te_3 /$Fe(Te, Se)$ heterostructures [67, 46].

4.6 Conclusion

Our results offer a promising pathway to study topological superconductivity with higher T_c . With the use of iron based superconductors one can induce much larger gaps in the topological surface states than with their low T_c counterparts. These larger gaps in turn allow one much greater energy resolution for studying the emergent in-gap states. Other iron based superconductors can be used to push this experiment to much higher temperature limits. For example one could use single-layer $FeSe$

grown on $SrTiO_3$ as a substrate, which offers a ~5 times larger gap [42], and a ~8 times greater T_c [41] than $Fe(Te, Se)$. This work offers a viable platform for exploring topological superconductivity without requiring millikelvin temperatures. We further extended this system to be a viable platform for studying the emergent phenomena when TCI materials undergo a superconducting phase transition. The van der Waals nature of Bi_2Te_3 makes it excellent for bridging the lattice mismatch on $SnTe$ drastically increasing the slew of available substrates.

Chapter 5 - Use of a Copper Based Superconducting Substrate

5.1 Bi_2Te_3 Thin Films Grown on Bi-2212

In the previous chapter I discussed using an iron based superconductor as a platform for realizing topological superconductivity in two different types of topological insulators. Use of an iron based superconductor allows us to induce larger superconducting gaps. This provides us with a platform for investigating in gap states with better energy resolution than heterostructures involving low T_c and elemental superconductors [25, 87, 20, 88, 21, 23, 53, 24, 26]. Even though the T_c in these iron based heterostructures is more than double that of lower T_c ones, 14 K is still a fairly low temperature. Additionally Iron based superconductors are relatively new when it comes to the field of high T_c superconductors. Copper based superconductors known as cuprates were the first high T_c superconductors to be discovered a few decades ago [89]. Cuprates such optimally doped $Bi_2Sr_2CaCu_2O_{8+x}$ (Bi-2212) has an extremely high T_c of ~91 K and it being a layered 2D material makes it an ideal substrate. Current efforts to realize topological superconductivity using cuprates have been mixed. ARPES measurements report no evidence of an induced superconducting gap in the topological insulators band structures [24, 28]. Possible reasons for this have been attributed to Bi-2212's very short coherence length along the c-axis [28], as well the Fermi surface mismatch between the TI and Bi-2212 substrate [24, 28]. On the other hand tunneling measurements performed on elemental bismuth [87] and Bi_2Te_3 [88] grown on Bi-2212 have reported gaps in the dI/dV spectra. These measured gaps have been interpreted as proximity induced topological superconductivity [87, 88]. In this work we grew a wide range of Bi_2Te_3 films in order to study the nature of this spectral gap.

Optimally doped $Bi_2Sr_2CaCu_2O_{8+x}$ (Bi-2212) is a layered 2D material that is weekly van der Waals bonded and has a natural cleavage plane (Figure 5.1.1). It cleaves between its consecutive BiO planes and reveals a square lattice of Bi atoms and characteristic super modulation (Figure 5.1.2 a).

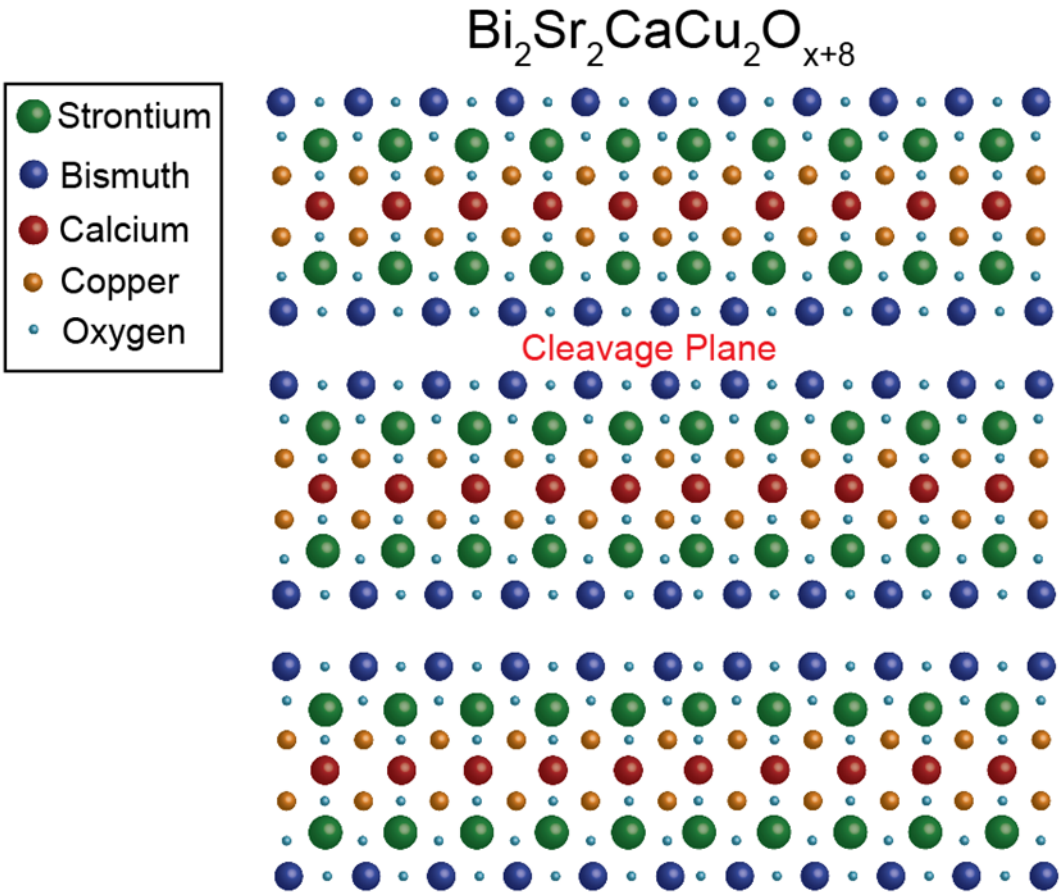

Figure 5.1.1: Side view of the $Bi_2Sr_2CaCu_2O_{8+x}$ crystal structure, the c-plane is pointing to the top of the page. Bulk $Bi_2Sr_2CaCu_2O_{8+x}$ cleaves between the BiO planes labeled in red.

Spectroscopic measurements on the surface of our pristine cleaved *Bi*-2212 reveal the large d-wave superconducting gap that is greater than 40 mV (Figure 5.1.2 b). This verifies that our *Bi*-2212 substrates are optimality doped and of high quality.

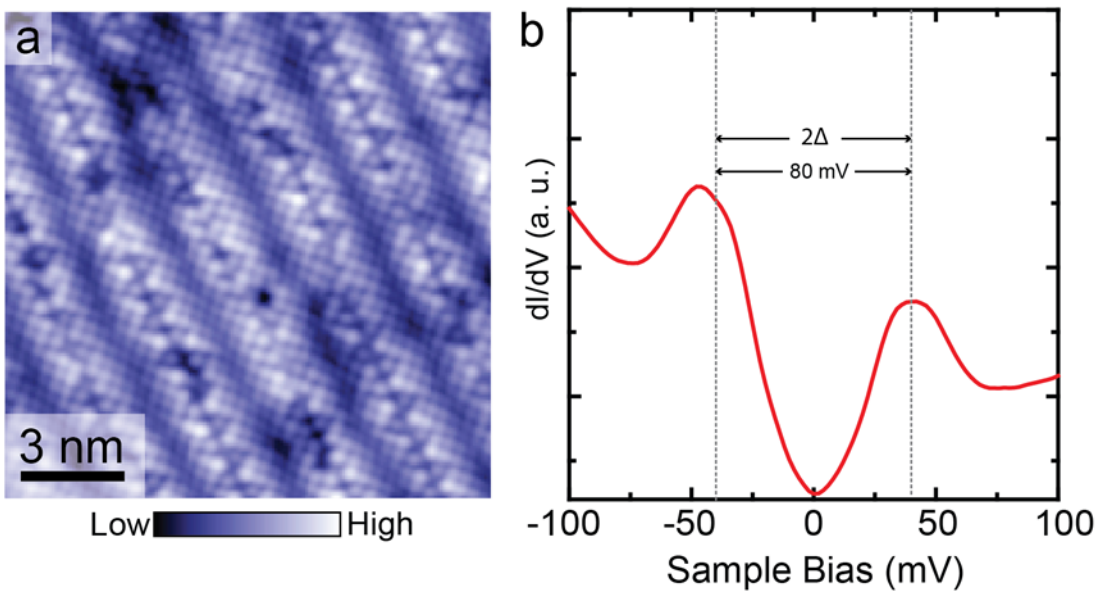

Figure 5.1.2: (a) STM topograph on an as cleaved Bi-2212 single crystal showing the characteristic super modulation, (b) average dI/dV spectra acquired on the surface of our Bi-2212 single crystals showing a large d-wave superconducting gap.

To grow our heterostructures we start by epoxying our Bi-2212 substrate to our sample holder along with a cleaving rod epoxied to the surface. Unlike our growths on cleaved $Fe(Te, Se)$, Bi-2212's surface is more prone to contamination from outgassing. To avoid this contamination, we first heat up the substrate prior to cleaving to let it outgas first. After it has outgassed for at least an hour, we let it cool down back to room temperature prior to cleaving. After cleaving we use RHEED to check the quality of the cleave. The characteristic RHEED pattern is not your typical 4 fold symmetric pattern you would expect from a square lattice. Instead you have three high symmetry directions that give you a streaky RHEED pattern (Figure 5.1.3). Two of the high symmetry directions figure 5.1.3 a and figure 5.1.3 b correspond to the in plane lattice constant and are proportional by a factor of $\sqrt{2}$. The third high symmetry direction figure 5.1.3 c shows a very fine reciprocal spacing corresponding to the structural super modulation.

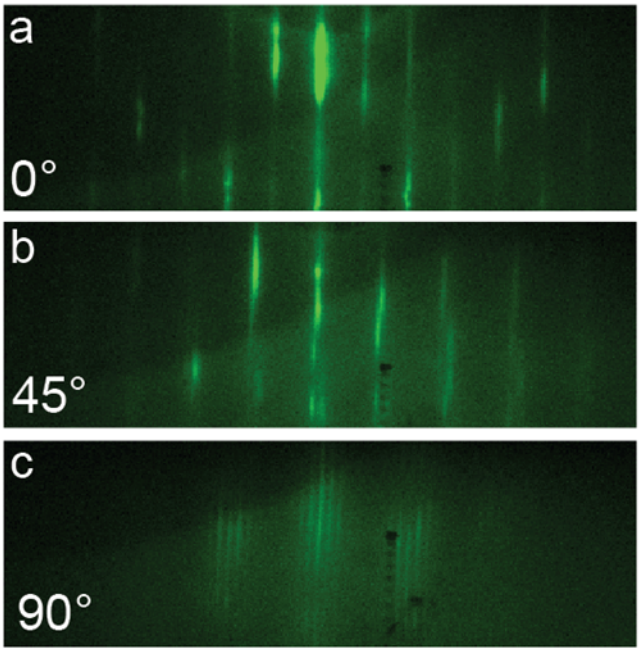

Figure 5.1.3: RHEED images taken along all three high symmetry directions on pristine cleaved *Bi*-2212 after it had been outgassed (a) 0° (b) 45° and (c) 90°.

Your typical square lattice will repeat its RHEED patterns every 90° but due to the super modulation *Bi*-2212 repeats very 180°. After cleaving we heat the substrate back up to our growth temperature. For the films in this experiment we used a range of different temperatures from ~170 to ~250 °C: the goal being to push the substrate growth temperature as low as possible. This is because the superconducting properties of the *Bi*-2212 surface are highly susceptible to heating (Figure 5.1.4). When the substrate is annealed, oxygen atoms escape from the top most crystal layer giving rise to a hard insulating gap [90].

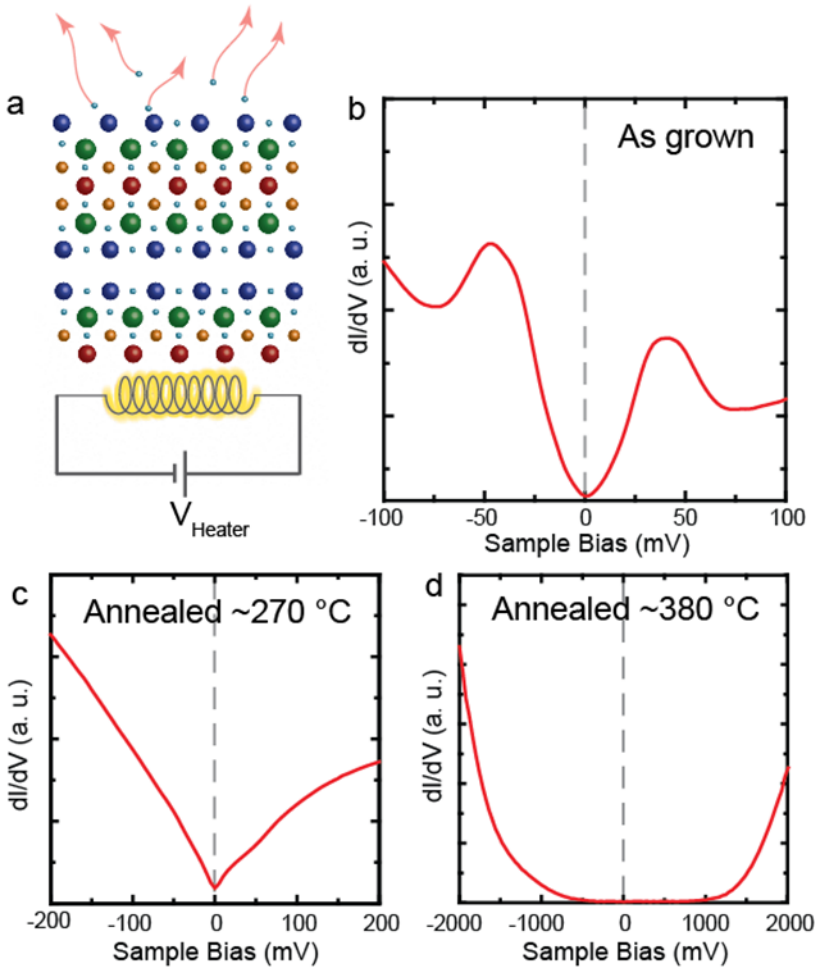

Figure 5.1.4: (a) Cartoon diagram showing how heating removes oxygen from the Bi-2212's top most layers. (b-d) Average dI/dV spectra taken on the surface of Bi-2212 before annealing (b), and after annealing it to ~270 °C (c) and ~380 °C (d).

Once the substrate has reached the desired growth temperature, elemental Bi and Te are co-evaporated in a ratio of 1:10 Bi:Te. Similar to our growth on $Fe(Te, Se)$ the Bi_2Te_3 grows with domain boundaries and these domains can be located within our STM (Figure 5.1.5 a). This gives us our characteristic "double line" RHEED pattern that repeats every 30° (Figure 5.1.6 a).

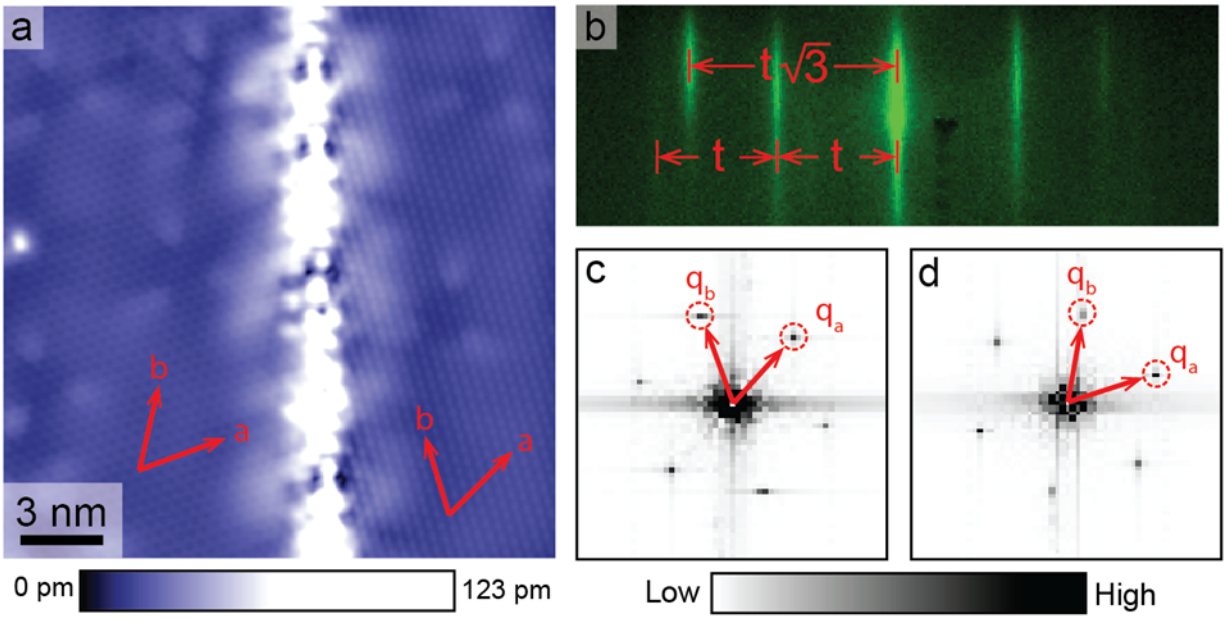

Figure 5.1.5: (a) STM topograph showing the location of a domain boundary on our Bi_2Te_3 surface. (b) RHEED image taken during the few minutes of Bi_2Te_3 deposition, (c) and (d) Fourier transforms of 9 nm square areas of (a) taken on the (c) left side and (d) right side of the domain boundary.

Despite these inevitable domain formations, we still are able to locate large flat regions to characterize the sample in STM (Figure 5.1.6 b).

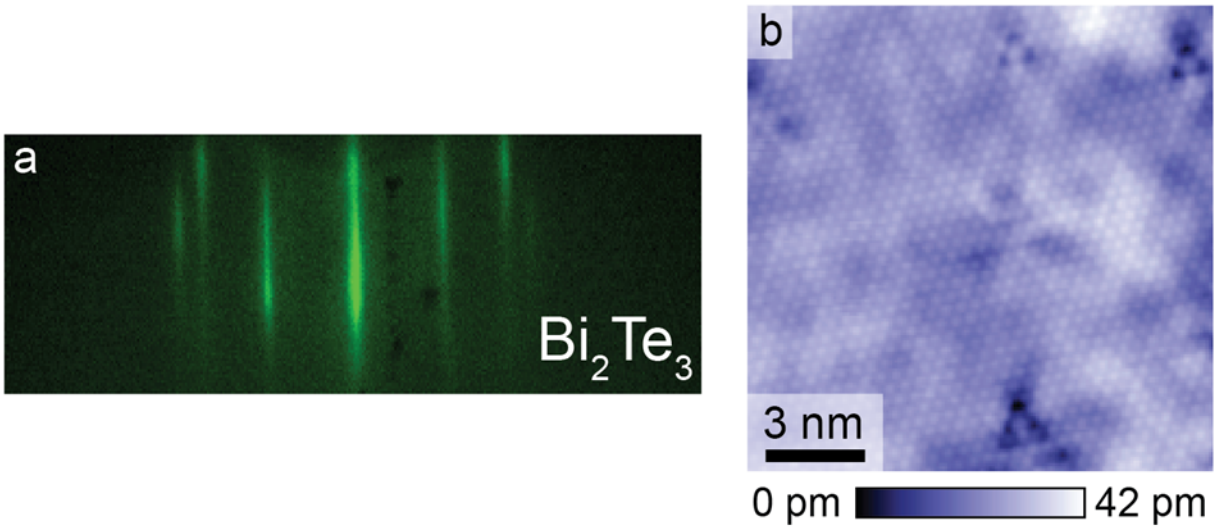

Figure 5.1.6: (a) RHEED image and (b) STM topograph of a few layers of Bi_2Te_3 grown on Bi-2212 below ~250 °C.

Once the samples are grown we transfer them to our STM via our vacuum suitcase to ensure they are never exposed to air.

5.2 Characterization of Thin Films of Bi_2Te_3 on Bi-2212

The main goal of this experiment was to see whether or not a d-wave superconductor can be used to induce a superconducting gap in the surface states of a topological insulator. Since the size of the superconducting gap at the exposed surface of our film decreases as a function of thicknesses [50], we grew a slew of different samples from 10 QL thick down to partial coverage. We start by characterizing the large scale electronic structure of our films by using QPI imaging [48, 91].

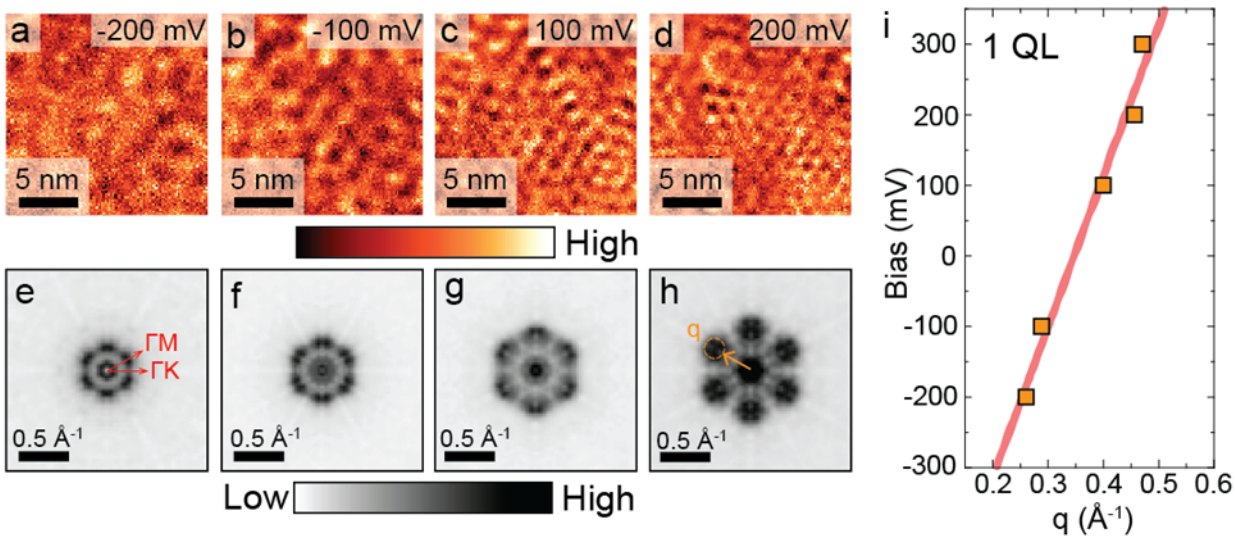

Figure 5.2.1: (a-d) dI/dV maps taken over the same area on our 1 QL thick sample and (e-h) their respective Fourier transforms. Wave-vector q in (h) denotes the QPI scattering vectors increasing length as a function of sample bias. (i) The extracted dispersion from the wave-vectors in (e-h).

Both our 1 QL (Figure 5.2.1) and our 2 QL (Figure 5.2.2) films show the characteristic scattering patterns and dispersion similar to bulk Bi_2Te_3 crystals [48, 49] and films [14, 46].

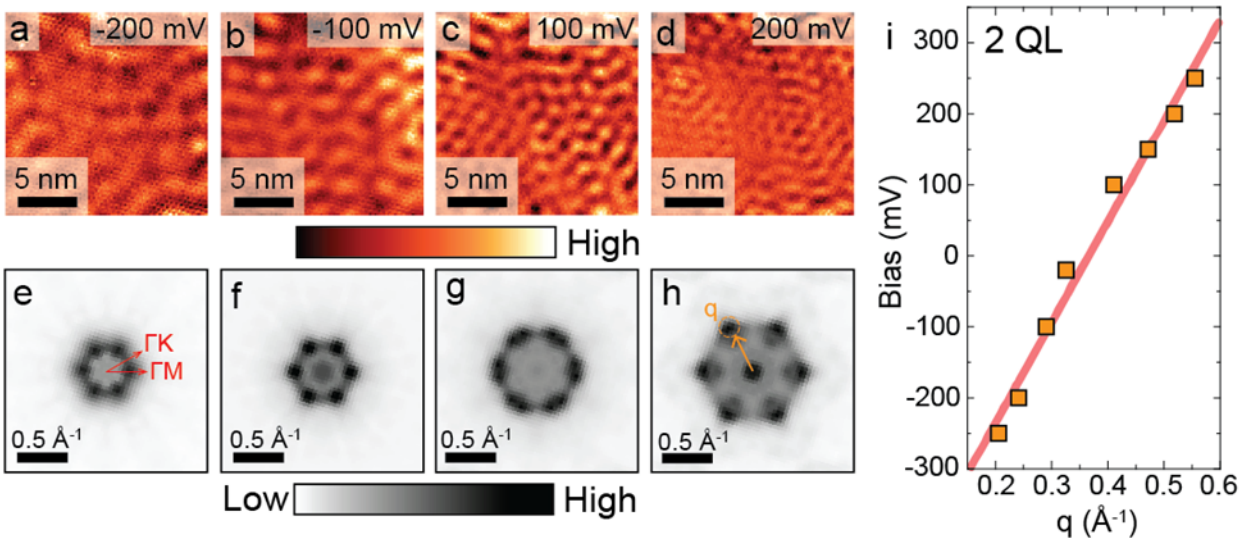

Figure 5.2.2: (a-d) dI/dV maps taken over the same area on our 2 QL thick sample and (e-h) their respective Fourier transforms. Wave-vector q in (h) denotes the QPI scattering vectors increasing length as a function of sample bias. (i) The extracted dispersion from the wave-vectors in (e-h).

We next look for look for any evidence of induced superconductivity on the surface of our 1 and 2 QL thick films. The dI/dV spectra acquired on both our 1 and 2 QL films show a small suppression in the density of states located ±5 to 10 meV around the Fermi level (Figure 5.2.3 b,e).

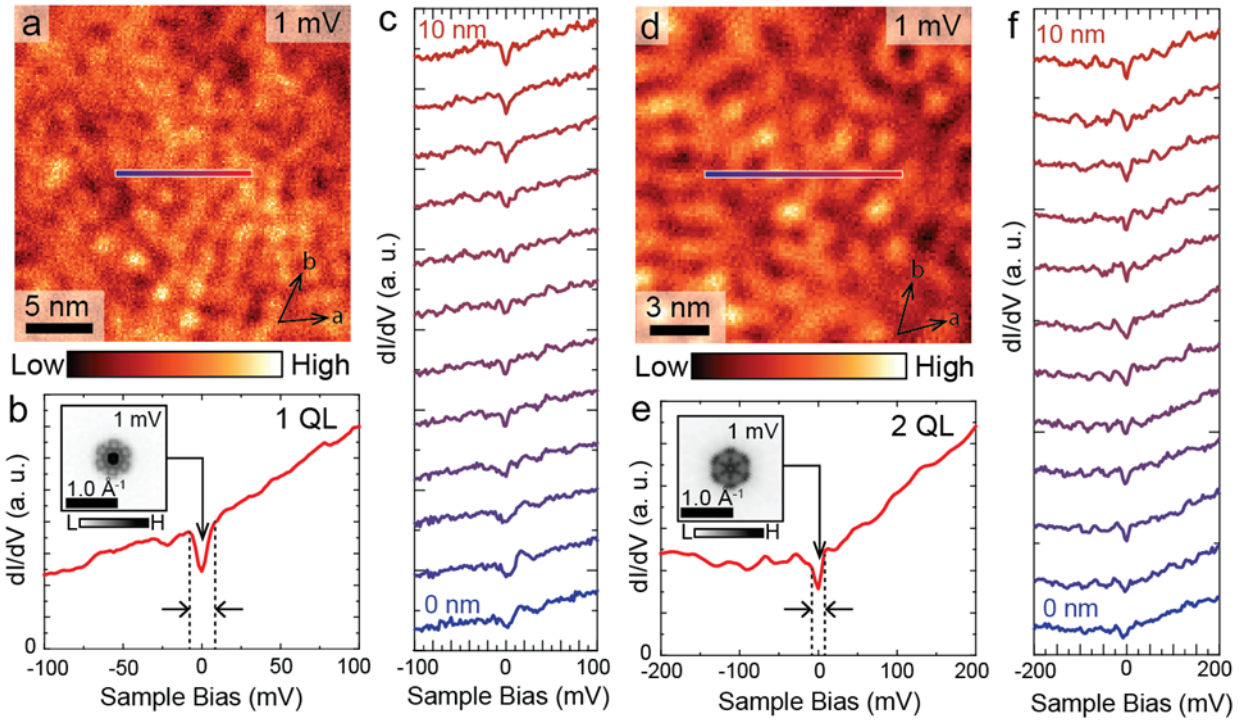

Figure 5.2.3: (a,d) dI/dV maps taken on (a) 1 QL and (d) 2 QL thick Bi_2Te_3 films showing a clear QPI interference pattern at a 1 mV bias. (b,e) Average dI/dV spectra taken on our (b) 1 QL and (e) 2 QL samples showing a gap-like feature near the Fermi energy denoted with dashed lines and arrows. Insets in (b) and (e) are the Fourier transforms of (a) and (d) respectively showing an in-gap QPI signature. (c,f) 10 nm line cut of the dI/dV spectra on (c) 1 QL and (f) 2 QL offset for clarity showing the showing the variation of the gap like feature. The gradient line in (a,d) denotes the region line cuts (c,f) were taken.

This gap like feature does not show clear coherence peaks and is fairly inhomogeneous (Figure 5.2.3 c,f). Previous experiments that have reported similar gap like features have attributed it to arising from proximity induced superconductivity from the underlying cuprate [87, 92]. Since the goal of this experiment is to induce a gap in the surface states we would expect to see a suppression of the QPI within the gapped region. However dI/dV maps taken close to the Fermi energy revealed a strong QPI signal (Figure 5.2.3 a,d). Therefor even if this gap was induced by the underlying cuprate our surface states would not be fully gapped. Our thicker 4 QL film shows a similar small suppression around the Fermi level that we see in our 1 and 2 QL thick films (Figure 5.2.4 b).

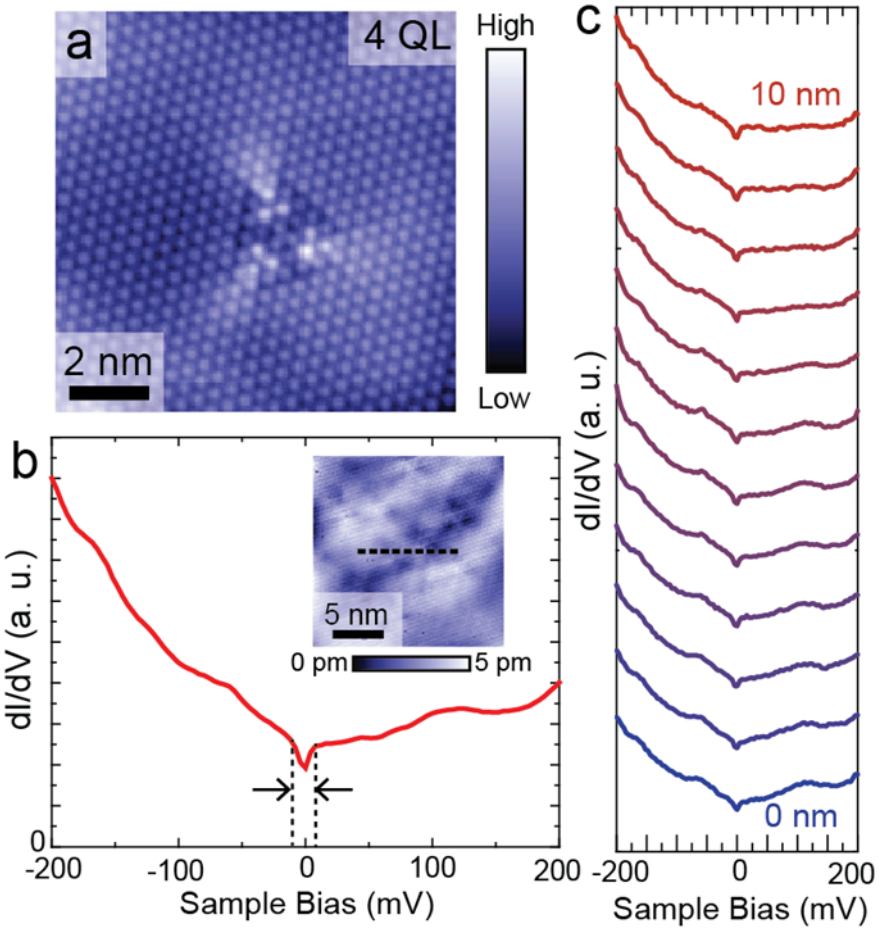

Figure 5.2.4: (a) STM topograph of a 4 QL Bi_2Te_3 film grown on Bi-2212. (b) Average dI/dV spectra taken over the region shown in (a). (c) 10 nm line cut of the dI/dV spectra taken across the dotted line in the inset topograph in (b).

Though unlike our 1 and 2 QL films the spectra is more homogenous (Figure 5.2.4 c), this is likely due to thicker films being more uniform. Since proximity induced superconductivity is expected to drop off exponentially as a function of thickness this gap is unlikely due to proximity induced superconductivity from the underlying cuprate; the gap magnitude seems to be unaffected by thickness. In order to shine some light on the nature of this gap, we grew films of reduced coverage. Typically it takes about 4 minutes to complete a full QL of Bi_2Te_3 , if we grow for only 24 seconds the result is mostly exposed Bi-2212 substrate with about 10% coverage of Bi_2Te_3 islands. This allows us to investigate the interface of our film. We know from some of our other work that the superconducting properties of the Bi-2212 surface are highly susceptible to heating [90] (Figure 4.2.4). Due to this we grew the films in this work at temperatures below 250 °C. Our 0.1 QL film verifies that our Bi-2212 substrate still shows a prominent d-wave superconducting gap (Figure 5.2.5).

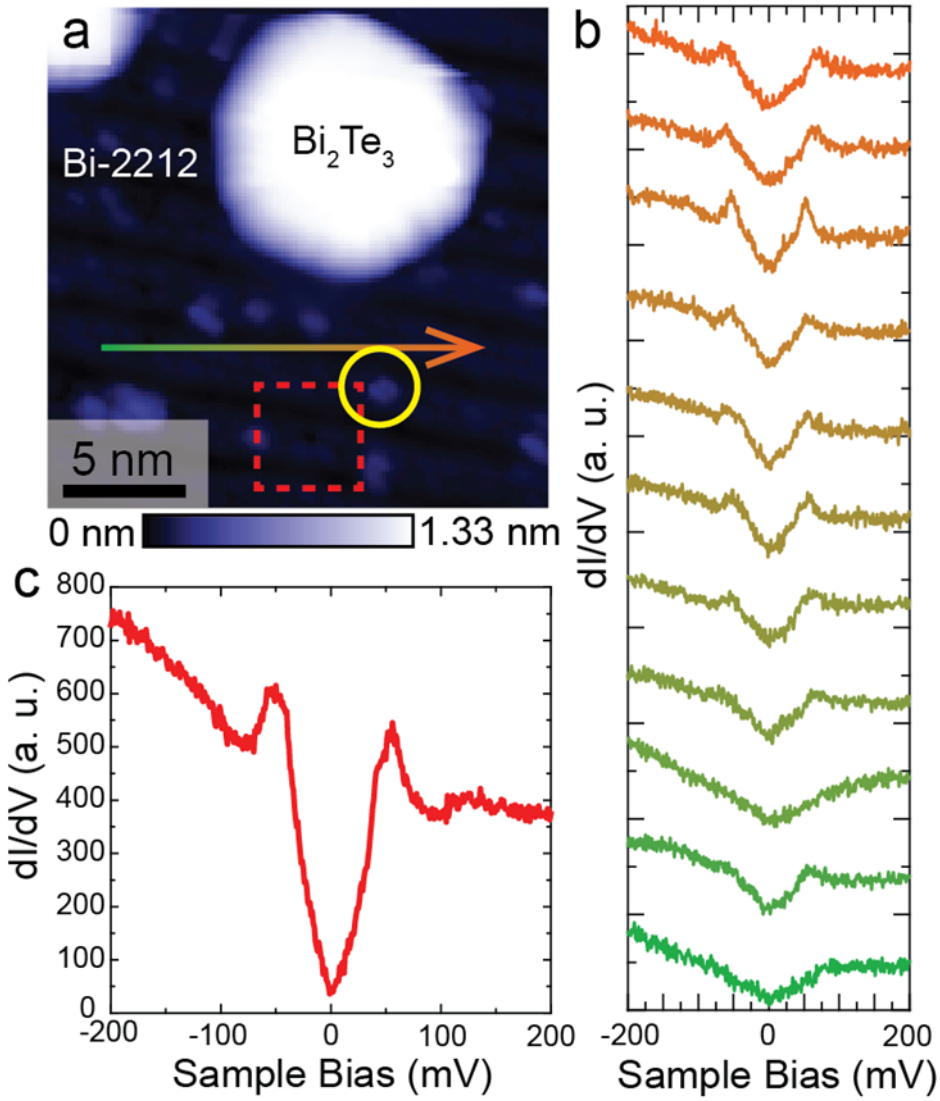

Figure 5.2.5: (a) STM topograph showing a Bi_2Te_3 nano-island and our exposed Bi-2212 substrate. (b) Line cut taken across the 15 nm line indicated by the arrow in (a). (c) Average dI/dV spectra take in the region denoted by red dashed square in (a). The yellow circle in (a) shows an example of an impurity on the surface that measures ~0.2 nm in height.

Though the spectra of our Bi-2212 substrate looks as expected (Figure 5.2.5 c), there are some noticeable clusters on the surface (circled in yellow in Figure 5.2.5 a). These are likely clusters composed of excess dilute amounts of Bi or Te. Most interestingly, when we check the topographic step height of our Bi_2Te_3 islands with respect to our substrate we find their apparent height to be ~1.2 nm (Figure 5.2.6 a,d).

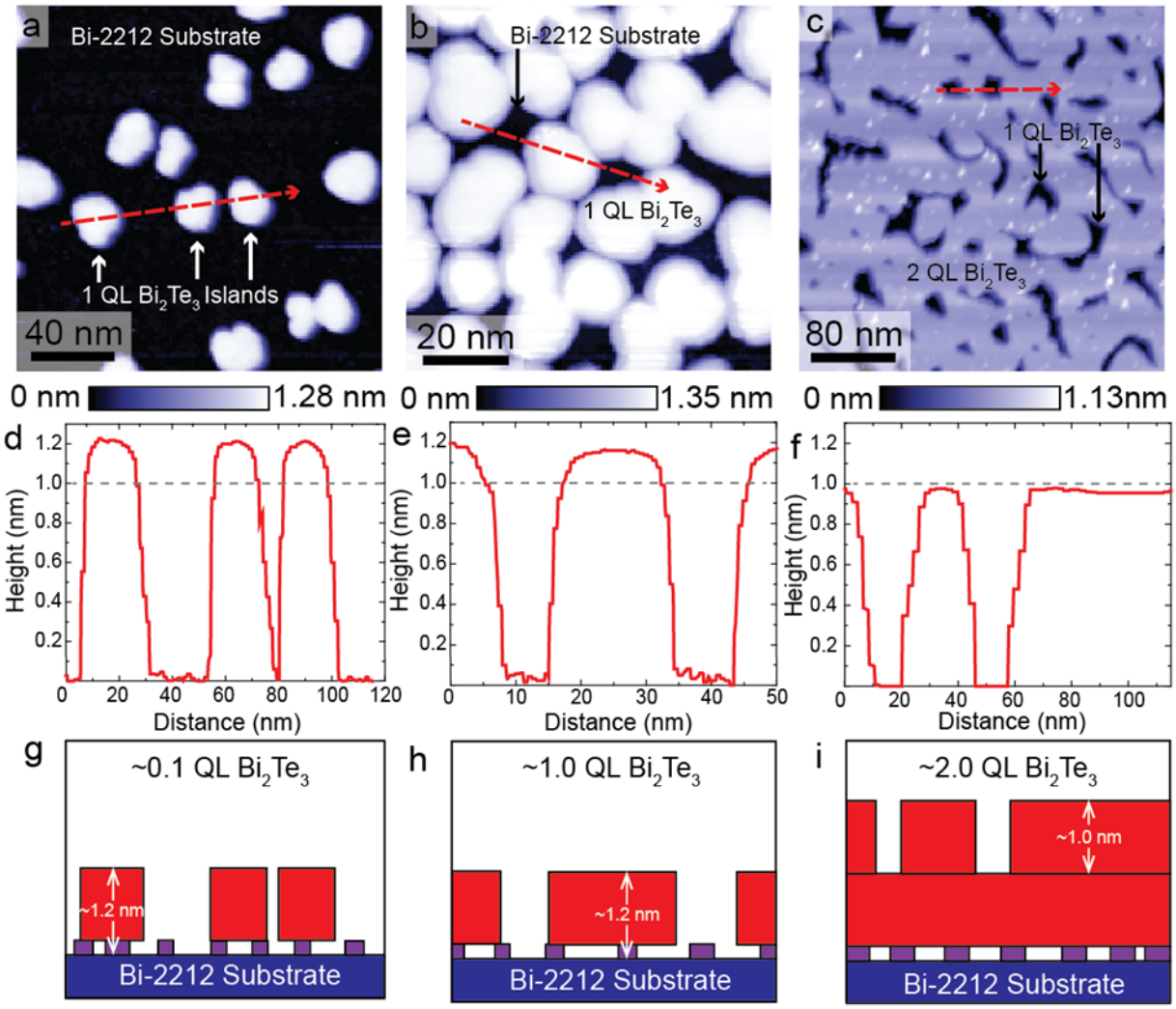

Figure 5.2.6: (a-c) STM topographs showing (a) Bi_2Te_3 nano-islands on Bi-2212 with ~10% coverage, (b) Bi_2Te_3 islands on Bi-2212 with ~90% coverage and (c) a 2 QL thick film of Bi_2Te_3 grown on Bi-2212. (d-f) topographic height profiles across the regions denoted by the red dashed arrows in (a-c). (g-f) Schematic depiction of the cross section of the interface consistent with the heights observed in (d-f).

This is ~20% taller than the expected 1 nm step height of Bi_2Te_3 was also apparent in films where we had nearly complete single layer coverage (Figure 5.2.6 b,e). In order to check that our STM scanner is properly calibrated, we also measured the topographic step height of a nearly completed 2 QL thick film with respect to the first layer of Bi_2Te_3 underneath. Our 2 QL thick films show the expected 1 nm step height (Figure 5.2.6 c,f). Since STM topographs contain both electronic and structural information, we provide two types of evidence that this height is indeed structural in nature. First we extract the step height from island topographs taken at both positive and negative sample bias; we found both to show the same additional height (Figure 5.2.7).

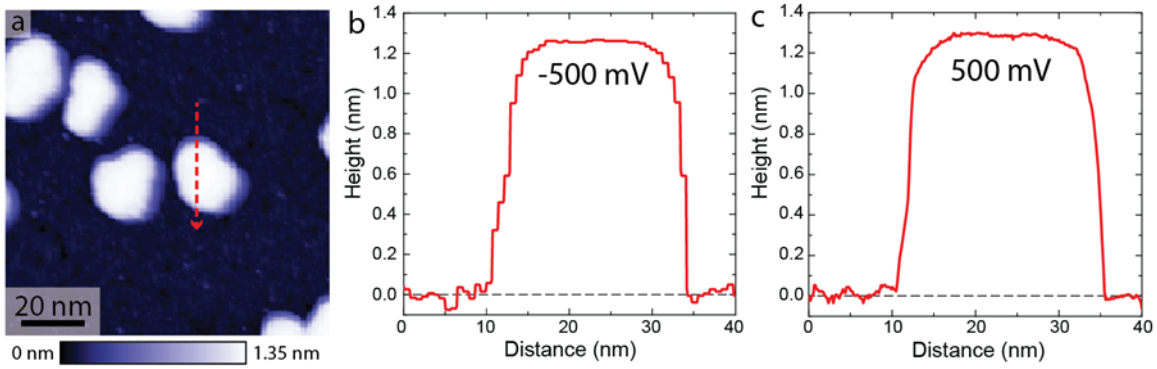

Figure 5.2.7: (a) A large-scale STM topograph showing Bi_2Te_3 islands on a Bi-2212 substrate, the red dashed arrow denotes where the height profiles in (b) and (c) were taken. (b,c) Topographic height profiles for the same island acquired at (b) negative and (c) positive sample bias.

The second piece of evidence is that Bi_2Te_3 islands grown on $SrTiO_3$ (111) (Figure 5.2.8 a,c) as well as $Fe(Te, Se)$ (Figure 5.2.8 b,d) both show the expected ~1 nm step height despite the fact that the two substrates are electronically very different materials.

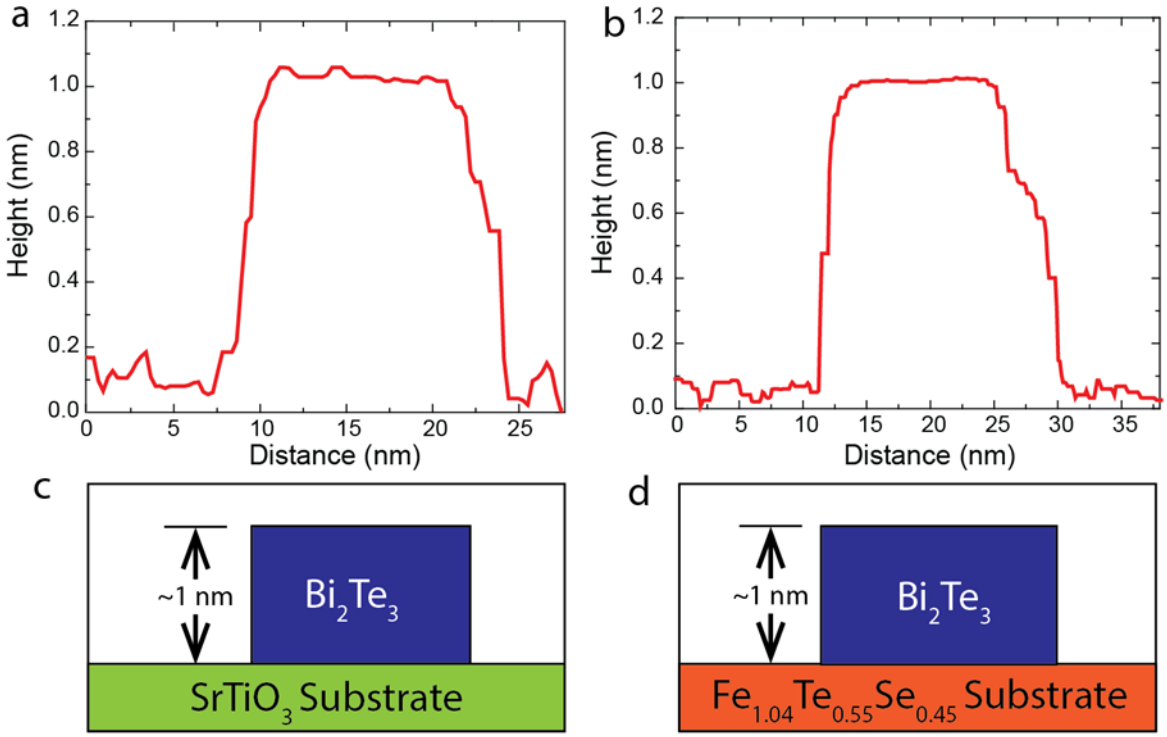

Figure 5.2.8: (a,b) Height profiles of Bi_2Te_3 a island grown on (a) $SrTiO_3$ and (b) $Fe(Te, Se)$ substrates. (c,d) Illustration of the observed island height on (c) $SrTiO_3$ and (d) $Fe(Te, Se)$.

To explain this additional ~20% height of our first Bi_2Te_3 layer with respect to our Bi-2212 substrate we postulate that it may be due to some sort of intergrowth layer forming at our interface. This intergrowth layer is likely made up of the same small cluster that can be seen on our substrates surface (Figure 5.2.5 a yellow circle). These clusters also have an approximate size equal to our barrier height; similar observations have occasionally been reported in other van der Waals heterostructures [93].

Next we investigate the consequences of the imperfect interface. A crucial insight comes from how the electronic properties of our Bi_2Te_3 islands are affected by their dimensional constraints. dI/dV spectra acquired on islands where the diameter was ~10 nm show a clearly different shaped hard gap (Figure 5.2.9 a). As the size of the island increases to an ~20 nm diameter this hard gap evolves into a V-shaped gap (Figure 5.2.9 b). Lastly as the first Bi_2Te_3 layer nears completion it evolves into the small suppression around the Fermi energy (Figure 5.2.9 c).

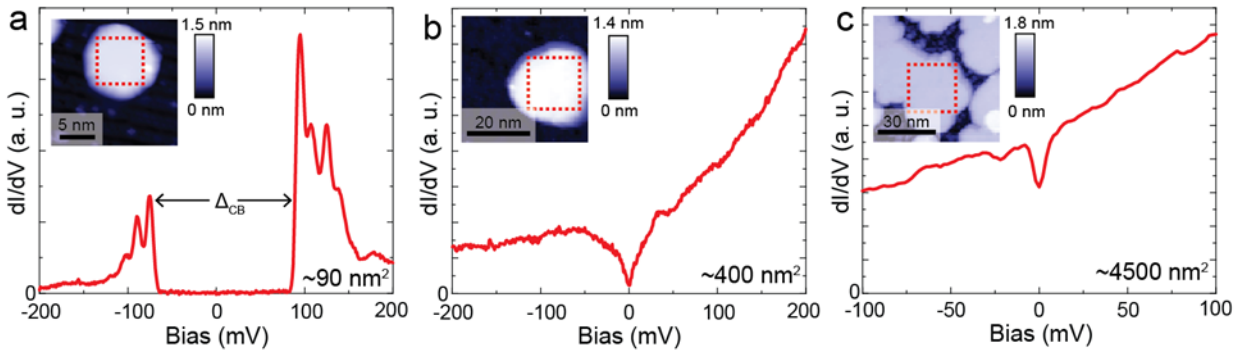

Figure 5.2.9: (a-c) Average dI/dV spectra taken over the regions denoted by the red dashed square in the inset topograph for (a) ~90 nm^2 island, (b) ~400 nm^2 island and (c) ~4500 nm^2 region of a 1 QL thick Bi_2Te_3 film.

This hard gap of ~150 meV in magnitude is significantly larger than 2Δ superconducting gap of Bi-2212. This hard gap interestingly also shows a clear asymmetry in energy (Figure 5.2.10).

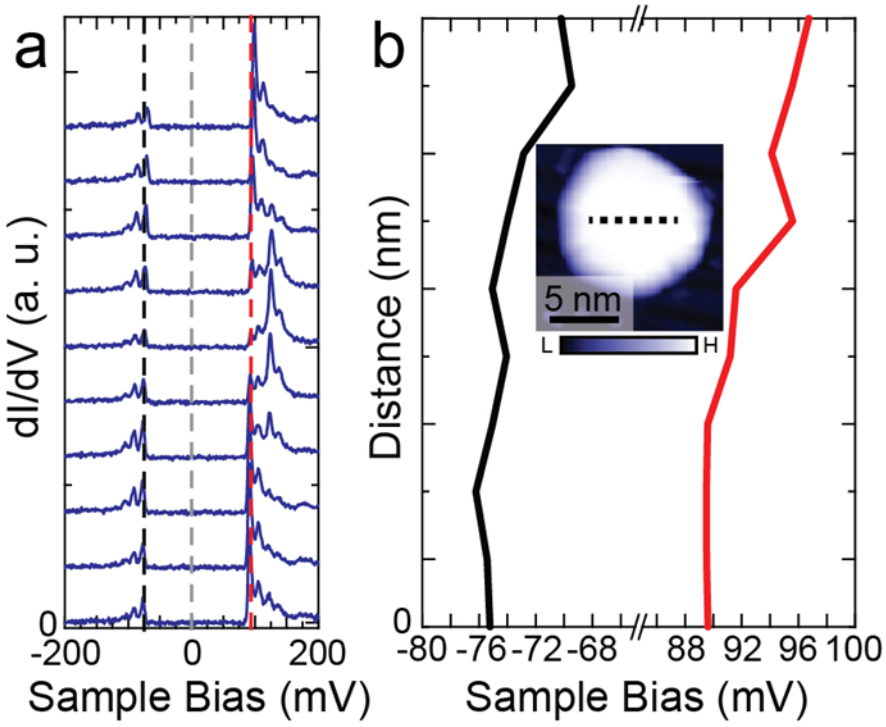

Figure 5.2.10: (a) dI/dV line cut on the ~90 nm^2 island from figure 5.2.9 a. (b) Spectral peak positions extracted from (a), the red and black lines denote the first positive (Red) and the first negative (black) peak positions.

Due to this clear asymmetry and the gap magnitude being several times larger than our *Bi*-2212 substrate we rule out proximity induced superconductivity as its origin. The additional peaks in the dI/dV spectra of our ~10 nm diameter island (Figure 5.2.9 a) outside the gap may be due to quantized bound states (Figure 5.2.11).

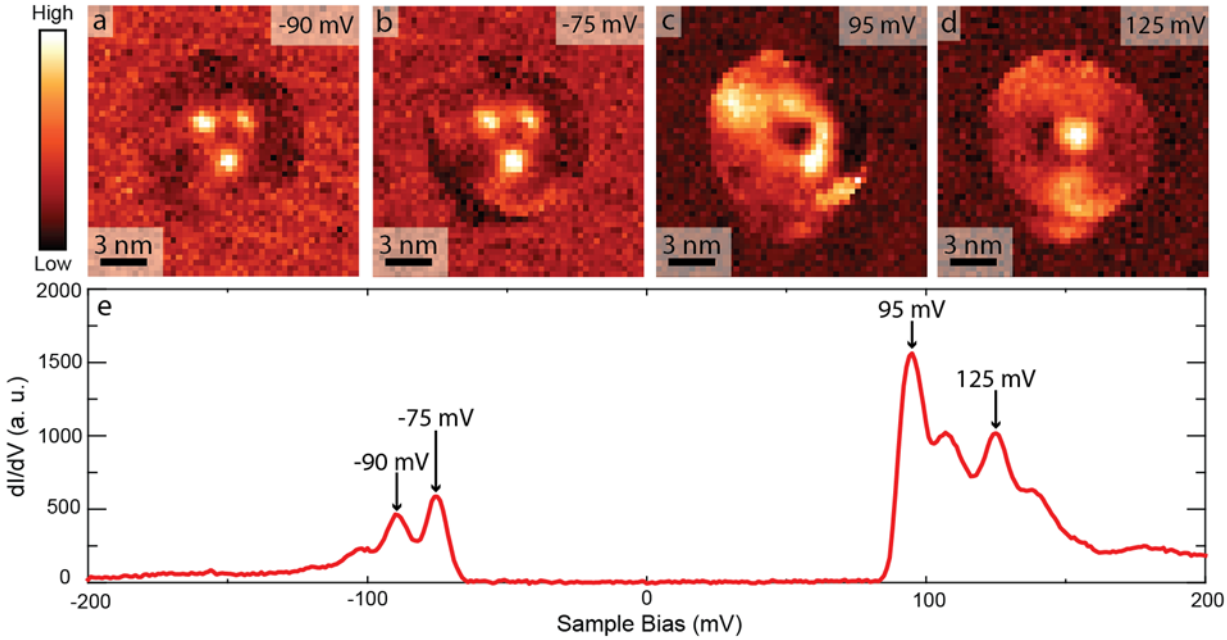

Figure 5.2.11: (a-d) dI/dV maps of the same field of view acquired at (a) -90 mV (b) -75 mV (c) 95 mV and (d) 125 mV sample bias. (e) dI/dV spectra averaged over the entire island.

This is similar to what has been observed on quantum dots [94]. Another possible explanation for these peaks could be due to capacitive coupling between island and STM tip [95]. Though it could be interesting to explore in future work, we did not explore a quantitative understanding of these peak positions in this work (Figure 5.2.11 e).

4.3 Coulomb Blockage

Due to this additional barrier at the interface and the effect it has on finite system size, we have concluded that a natural explanation for this gap can be understood as a Coulomb blockade (CB) gap [96]. These CB gaps arise due to single electrons exchanging energy with the environment during tunneling [97, 98]. Previous experiments have reported the CB effect in tunneling measurements for heterostructures when there is an additional barrier at the interface [99, 100, 95, 101]. Tunneling measurements that involve the CB effect can be modeled using a double tunnel junction, the first junction being the tip-sample junction and the second being the sample-substrate junction (Figure 5.3.1).

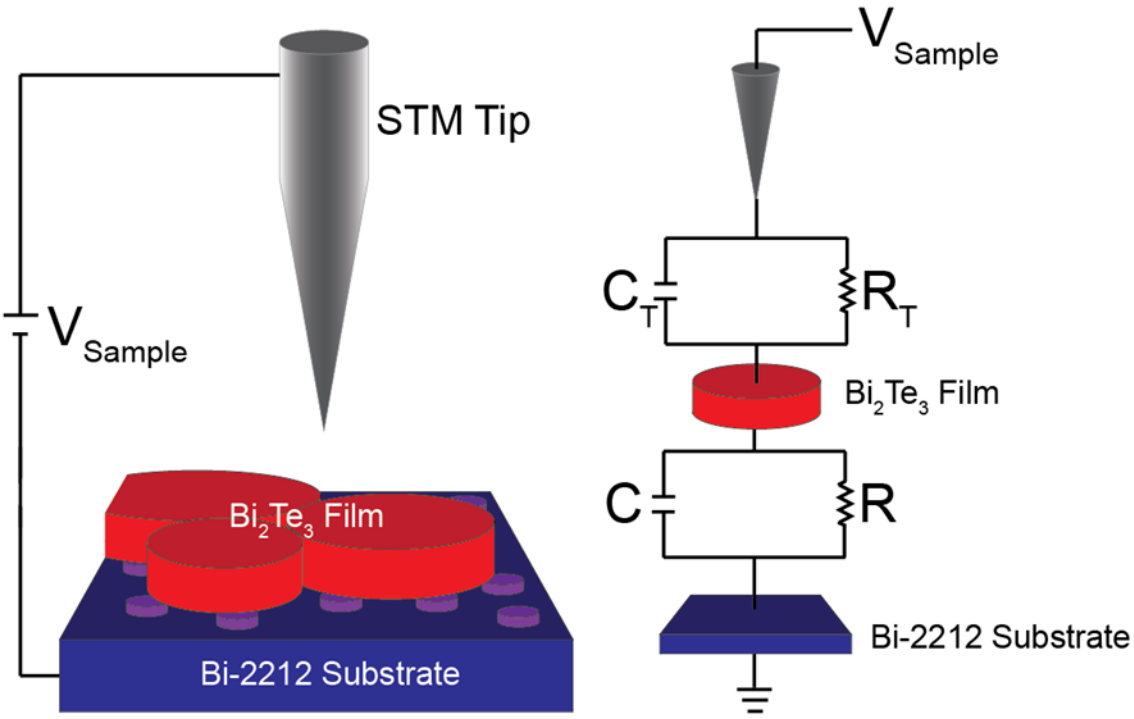

Figure 5.3.1: Diagram showing the double tunnel junction involved in our measurements, C_T and R_T are the respective tip-film capacitance and resistance, while C and R are the capacitance and resistance of the film-substrate junction.

The size of the CB gap is roughly inversely proportional to the capacitance (C) between the film and the substrate [99, 101]. The shaped of the gap depends on the resistive component of the film-substrate junction (R). Large R will give a sharp cut-off in the conductance at the gap edge, while small R gives a more gradual suppression when approaching the Fermi energy [99, 101]. On our smallest Bi_2Te_3 island we observe a sharp CB gap that goes to zero conductance (Figure 5.2.9 a). As our island increases in size C will become larger while R decreases evolving the gap into a smaller V-shaped gap (Figure 5.2.9 b). As the film grows to become more continuous these islands merge together and the V-shaped gap becomes more subdued with a finite conductance at the Fermi level (Figure 5.2.9 c). Similar to references [99, 101] we used the dynamical Coulomb blockade $P(E)$ theory to fit the overall shape of our observed spectra. This theory incorporates the additional capacitance/resistance from tip-film junction (C_T/R_T) as well as the film-substrate junction (C/R) as input parameters. Coulomb charging effects will be present in tunneling measurements when the total junction resistance is on the order of the resistance quanta $R_K = h/e^2$ [99, 98, 102, 103, 104]. The $P(E)$ theory of the dynamical Coulomb blockade accounts for the total impedance of the of our STM tunnel junction setup. This

total impedance is given by:

$$Z(\omega) = \left[i\omega C + i\omega C_T + R^{-1}\right]^{-1}$$

We can use this total impedance $Z(\omega)$ to get the equilibrium correlation function of the phase $J(t)$ given by:

$$J(t) = 2\int_0^\infty \frac{d\omega}{\omega} \frac{ReZ(\omega)}{R_K} \frac{e^{-i\omega t} - 1}{1 - e^{\frac{-\hbar\omega}{k_B T}}}$$

$J(t)$ can be solved analytically [104] and used to calculate the probability $P(E)$ that an electron with energy E will tunnel into the circuit [103].

$$P(E) = \frac{1}{2\pi\hbar}\int_{-\infty}^{\infty} dt\, exp\left[J(t) + \frac{iEt}{\hbar}\right]$$

From here the total tunneling current can be solved perturbatively from the difference of the tunneling rates from tip to sample and sample to tip.

$$I(V) = -e\left[\Gamma_{tip\rightarrow sample}(V) - \Gamma_{sample\rightarrow tip}(V)\right]$$

These rates can be computed using the $P(E)$ theory's probability integral form given by:

$$\Gamma_{sample\rightarrow tip}(V) = \frac{1}{e^2 R_T}\int_{-\infty}^{\infty} dE \frac{EP(eV + E)}{e^{\frac{E}{k_B T}} - 1}$$

The same code that was used by Brun et al. [99] was provided to us by Christian Flindt and Konrad Müller, that we used to calculate our theoretical dI/dV spectra in figure 5.4.2.

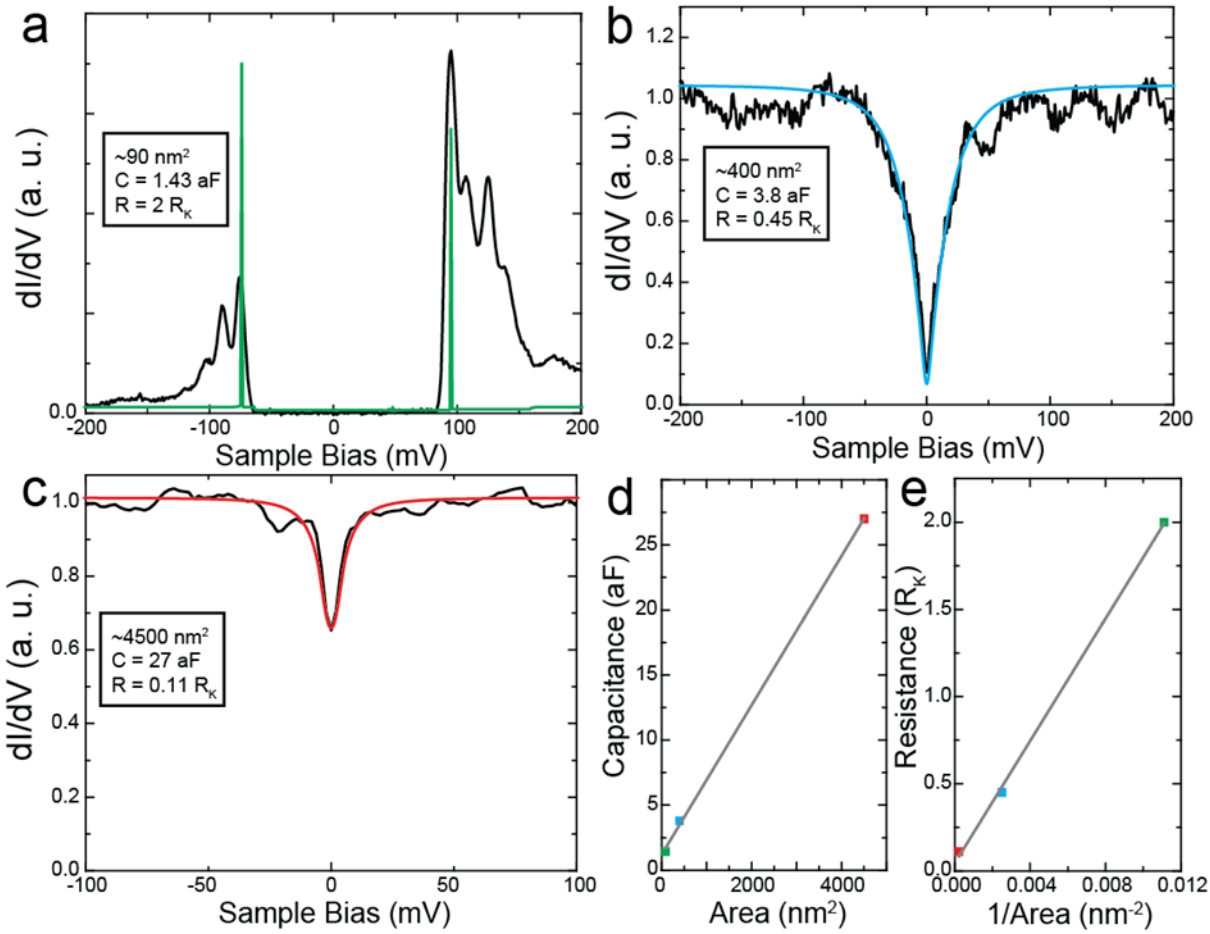

Figure 5.3.2: (a-c) (black curves) Normalized average dI/dV spectra from figure 5.2.9 on (a) ~90 nm^2 island (b) ~400 nm^2 island and (c) ~4500 nm^2 Bi_2Te_3 domains. Third and second order polynomials were subtracted from the background in (b) and (c) respectively in order to normalize the spectra; (a-c) (color curves) Theoretical model with the fitting parameters show in the inset. (d) Scatter plot of the capacitance values extracted from our fits with respect to approximate domain size. (e) Scatter plot of the resistance determined from the theoretical fits and inverse domain size.

From our calculated dI/dV spectra we obtain a good fit with our experimental data. The film-substrate capacitance C and resistance R depend on the exact nature of the contact, and therefor can vary quite a bit even if the film's area is kept the same [99]. If we were to treat our smallest island as a parallel plate capacitor with area $A = 90\,nm^2$ and spacing $d = 0.2\,nm$, the capacitance C would equal $\varepsilon_0 \varepsilon_r \frac{A}{d} \approx 4\,aF$. This is of comparable magnitude to $1.5\,aF$ extracted from our fits. Since the dielectric constant depends on the nature of the intergrowth layer and since ours is most likely comprised of excess Bi and Te, we take ε_r to be on the order of 1. Though there is clearly a discrepancy between treating our films like parallel plate capacitors and our extracted C values from our fits, we should still find that C increases linearly with area, while R decreases linearly with area [99]. We confirm this by plotting the fit parameters as a function of approximate area estimated from our STM topographs,

both show the expected liner scaling (Figure 5.3.2 d,e).

As mentioned a few times in this dissertation when Bi_2Te_3 is grown on a structurally mismatched substrate it will inevitably contain structural domains, that can be seen in both RHEED (Figure 5.1.6 a) and STM (Figure 5.1.5 a). These domains will be present even in thicker films giving rise to finite size effects despite the islands merging to form a continuous film. As our film thickness increases the gap-like feature gets suppressed and the zero-bias conductance increases (Figure 5.3.3).

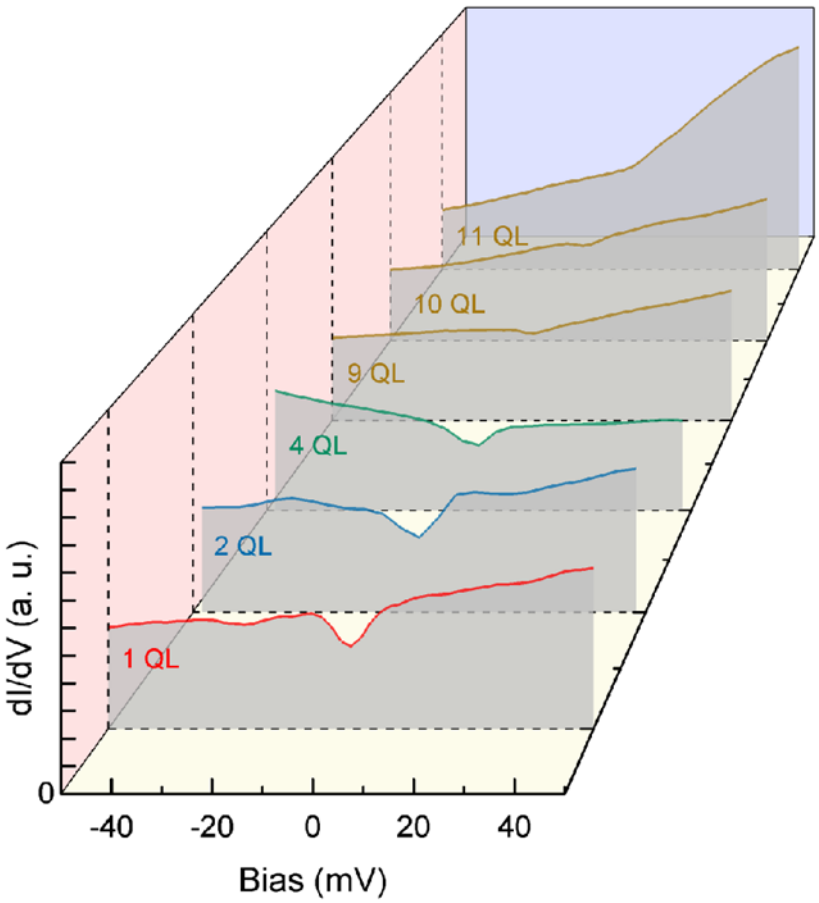

Figure 5.3.3: Average dI/dV spectra on Bi_2Te_3 taken over regions of various thickness on four different sample: 1 QL, 2 QL and 4 QL were all different samples while the ~9, ~10 and ~11 QL data is from the same nominally ~10 QL thick sample acquired on different consecutive terraces.

Though in our 1,2 and 4 QL films the gap-like feature is fairly prominent, our thicker films around 9-10 QL only show a small suppression around zero energy and nearly disappears in 11 QL thick films (Figure 5.3.3). This can be understood as a consequence of the decreased resistivity in thicker films. Our calculated dI/dV spectra for our 2,4 and 9 QL films are also in good agreement with our

experimental data (Figure 5.3.4).

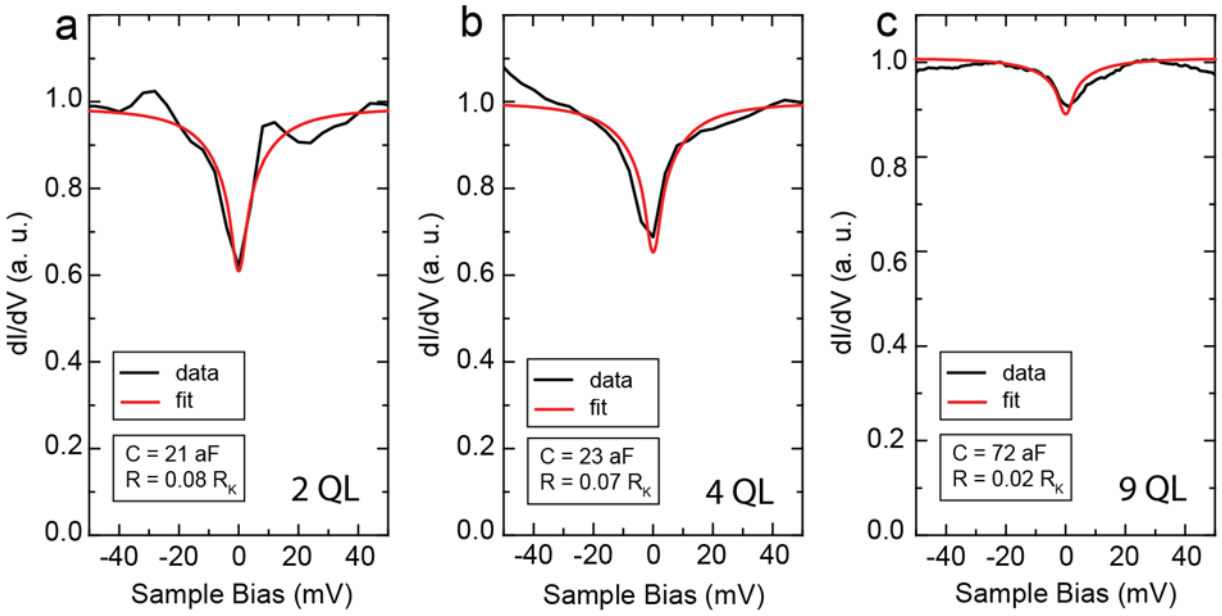

Figure 5.3.4: (a-c) (black curves) Normalized average dI/dV spectra take from figure 5.3.3 on (a) 2 QL, (b) 4 QL and (c) 9 QL thick films. Third degree polynomials were subtracted off the background of the raw data in order to normalize it. (red curves) DCB theoretical model with the fitting parameters shown in the inset.

We postulate that in our thicker films the domains on average become larger due to strain relaxation as the film grows. The increasing capacitance and decreasing resistance extracted from our fits adds further credence to domain size increasing in thicker films. Therefor the CB effect will be weaker but still present in thicker films, and the gap-like feature observed in our measurements is most likely a consequence of this and not from proximity induced superconductivity.

5.4 Conclusion

In chapter 4, I showed how an iron based superconductor can be used to induce superconductivity at higher temperatures in a TI and TCI. While in this chapter I covered our efforts to use a copper based superconductor in an attempt to gap out the surface states of a TI. Though we did measure a gap-like feature around the Fermi energy, it did not have the necessary elements to interpret it as a superconducting gap. Unlike our films grown on $Fe(Te, Se)$, the ones grown on Bi-2212 have an inevitable intergrowth layer, likely caused by the necessity of lower growth temperatures due to the sensitive of Bi-2212 surface itself. It is possible that through exfoliation methods a much cleaner

interface can be achieved, but with MBE grown films it would be extremely difficult to obtain. This work can be further extended to many MBE grown films where tunneling measurements show gap-like features around the Fermi energy. We stress the importance of investigating the bonding at the interface of the film and substrate and caution the interpretation of gap-like features.

References

[1] R. Pathria Beale and P. D. *Statistical Mechanics, 3rd ed.* Elsevier, 2011.

[2] L. D. Landau. On the Theory of Phase Transitions. *Zh. Eksp. Teor. Fiz*, 7:19–32, 1937.

[3] E. Noether. Invariante Variationsprobleme. *Nachrichten von der Gesellschaft der Wissenschaften zu Göttingen. Mathematisch-Physikalische Klasse*, S:235–257, 1918.

[4] K. V. Klitzing, G. Dorda, and M. Pepper. New Method for High-Accuracy Determination of the Fine-Structure Constant Based on Quantized Hall Resistance. *Physical Review Letters*, 45(6):494–497, aug 1980.

[5] J M Kosterlitz and D. J. Thouless. Ordering, metastability and phase transitions in two-dimensional systems. *Journal of Physics C: Solid State Physics*, 6(7):1181–1203, apr 1973.

[6] V. Berezinskii. Destruction of long range order in one-dimensional and two-dimensional systems having a continuous symmetry group. I. Classical systems. *Soviet Physics Jetp*, 32(3):493–500, jul 1971.

[7] D. J. Thouless, M. Kohmoto, M. P. Nightingale, and Marcel den Nijs. Quantized Hall Conductance in a Two-Dimensional Periodic Potential. *Physical Review Letters*, 49(6):405–408, aug 1982.

[8] F. D. M. Haldane. Model for a Quantum Hall Effect without Landau Levels: Condensed-Matter Realization of the "Parity Anomaly". *Physical Review Letters*, 61(18):2015–2018, oct 1988.

[9] B. Andrei Bernevig and Shou-Cheng Zhang. Quantum Spin Hall Effect. *Physical Review Letters*, 96(10):106802, mar 2006.

[10] Markus Konig, Steffen Wiedmann, Christoph Brune, Andreas Roth, Hartmut Buhmann, Laurens W Molenkamp, Xiao-liang Qi, and Shou-cheng Zhang. Quantum Spin Hall Insulator State in HgTe Quantum Wells. *Science*, 318(5851):766–770, nov 2007.

[11] D. Hsieh, D. Qian, L. Wray, Y. Xia, Y. S. Hor, R. J. Cava, and M. Z. Hasan. A topological Dirac insulator in a quantum spin Hall phase. *Nature*, 452(7190):970–974, apr 2008.

[12] Y L Chen, J G Analytis, J.-H. Chu, Z K Liu, S.-K. Mo, X L Qi, H. J. Zhang, D H Lu, X Dai, Z Fang, S C Zhang, I R Fisher, Z Hussain, and Z.-X. Shen. Experimental Realization of a Three-Dimensional Topological Insulator, Bi_2Te_3. *Science*, 325(5937):178–181, jul 2009.

[13] Y. Xia, D. Qian, D. Hsieh, L. Wray, A. Pal, H. Lin, A. Bansil, D. Grauer, Y. S. Hor, R. J. Cava, and M. Z. Hasan. Observation of a large-gap topological-insulator class with a single Dirac cone on the surface. *Nature Physics*, 5(6):398–402, jun 2009.

[14] Haijun Zhang, Chao-Xing Liu, Xiao-Liang Qi, Xi Dai, Zhong Fang, and Shou-Cheng Zhang. Topological insulators in Bi_2Se_3, Bi_2Te_3 and Sb_2Te_3 with a single Dirac cone on the surface. *Nature Physics*, 5(6):438–442, jun 2009.

[15] Timothy H Hsieh, Hsin Lin, Junwei Liu, Wenhui Duan, Arun Bansil, and Liang Fu. Topological crystalline insulators in the SnTe material class. *Nature Communications*, 3(1):982, jan 2012.

[16] Y. Tanaka, Zhi Ren, T. Sato, K. Nakayama, S. Souma, T. Takahashi, Kouji Segawa, and Yoichi Ando. Experimental realization of a topological crystalline insulator in SnTe. *Nature Physics*, 8(11):800–803, nov 2012.

[17] Liang Fu and C. L. Kane. Superconducting Proximity Effect and Majorana Fermions at the Surface of a Topological Insulator. *Physical Review Letters*, 100(9):096407, mar 2008.

[18] Chen Fang, Matthew J. Gilbert, and B. Andrei Bernevig. New Class of Topological Superconductors Protected by Magnetic Group Symmetries. *Physical Review Letters*, 112(10):106401, mar 2014.

[19] Tatsuki Hashimoto, Keiji Yada, Masatoshi Sato, and Yukio Tanaka. Surface electronic state of superconducting topological crystalline insulator. *Physical Review B*, 92(17):174527, nov 2015.

[20] Hao-Hua Sun, Kai-Wen Zhang, Lun-Hui Hu, Chuang Li, Guan-Yong Wang, Hai-Yang Ma, Zhu-An Xu, Chun-Lei Gao, Dan-Dan Guan, Yao-Yi Li, Canhua Liu, Dong Qian, Yi Zhou, Liang Fu, Shao-Chun Li, Fu-Chun Zhang, and Jin-Feng Jia. Majorana Zero Mode Detected with Spin Selective Andreev Reflection in the Vortex of a Topological Superconductor. *Physical Review Letters*, 116(25):257003, jun 2016.

[21] Mei-xiao Wang, Canhua Liu, Jin-Peng Xu, Fang Yang, Lin Miao, Meng-yu Yao, C L Gao, Chenyi Shen, Xucun Ma, X Chen, Zhu-an Xu, Ying Liu, Shou-cheng Zhang, Dong Qian, Jin-Feng Jia, and Qi-Kun Xue. The Coexistence of Superconductivity and Topological Order in the Bi_2Se_3 Thin Films. *Science*, 336(6077):52–55, apr 2012.

[22] Su-Yang Xu, Chang Liu, Anthony Richardella, I. Belopolski, N. Alidoust, M. Neupane, G. Bian, Nitin Samarth, and M. Z. Hasan. Fermi-level electronic structure of a topological-insulator/cuprate-superconductor based heterostructure in the superconducting proximity effect regime. *Physical Review B*, 90(8):085128, aug 2014.

[23] Jin-Peng Xu, Mei-Xiao Wang, Zhi Long Liu, Jian-Feng Ge, Xiaojun Yang, Canhua Liu, Zhu An Xu, Dandan Guan, Chun Lei Gao, Dong Qian, Ying Liu, Qiang-Hua Wang, Fu-Chun Zhang, Qi-Kun Xue, and Jin-Feng Jia. Experimental Detection of a Majorana Mode in the core of a

Magnetic Vortex inside a Topological Insulator-Superconductor $Bi_2Te_3NbSe_2$ Heterostructures. *Phys. Rev. Lett.*, 114(1):017001, jan 2015.

[24] Su-Yang Xu, Nasser Alidoust, Ilya Belopolski, Anthony Richardella, Chang Liu, Madhab Neupane, Guang Bian, Song-Hsun Huang, Raman Sankar, Chen Fang, Brian Dellabetta, Wenqing Dai, Qi Li, Matthew J. Gilbert, Fangcheng Chou, Nitin Samarth, and M. Zahid Hasan. Momentum-space imaging of Cooper pairing in a half-Dirac-gas topological superconductor. *Nature Physics*, 10(12):943–950, dec 2014.

[25] Fanming Qu, Fan Yang, Jie Shen, Yue Ding, Jun Chen, Zhongqing Ji, Guangtong Liu, Jie Fan, Xiunian Jing, Changli Yang, and Li Lu. Strong Superconducting Proximity Effect in Pb-Bi_2Te_3 Hybrid Structures. *Scientific Reports*, 2(1):339, dec 2012.

[26] Fan Yang, Yue Ding, Fanming Qu, Jie Shen, Jun Chen, Zhongchao Wei, Zhongqing Ji, Guangtong Liu, Jie Fan, Changli Yang, Tao Xiang, and Li Lu. Proximity effect at superconducting Sn-Bi_2Se_3 interface. *Physical Review B - Condensed Matter and Materials Physics*, 85(10):1–6, 2012.

[27] Eryin Wang, Hao Ding, Alexei V. Fedorov, Wei Yao, Zhi Li, Yan-Feng Lv, Kun Zhao, Li-Guo Zhang, Zhijun Xu, John Schneeloch, Ruidan Zhong, Shuai-Hua Ji, Lili Wang, Ke He, Xucun Ma, Genda Gu, Hong Yao, Qi-Kun Xue, Xi Chen, and Shuyun Zhou. Fully gapped topological surface states in Bi_2Se_3 films induced by a d-wave high-temperature superconductor. *Nature Physics*, 9(10):621–625, oct 2013.

[28] T. Yilmaz, I. Pletikosić, A. P. Weber, J. T. Sadowski, G. D. Gu, A. N. Caruso, B. Sinkovic, and T. Valla. Absence of a proximity effect for a thin-films of a Bi_2Se_3 topological insulator grown on top of a $Bi_2Sr_2CaCu_2O_{8+\delta}$ cuprate superconductor. *Physical Review Letters*, 113(6):1–5, 2014.

[29] Parisa Zareapour, Alex Hayat, Shu Yang F. Zhao, Michael Kreshchuk, Achint Jain, Daniel C. Kwok, Nara Lee, Sang Wook Cheong, Zhijun Xu, Alina Yang, G. D. Gu, Shuang Jia, Robert J. Cava, and Kenneth S. Burch. Proximity-induced high-temperature superconductivity in the topological insulators Bi_2Se_3 and Bi_2Te_3. *Nature Communications*, 3, 2012.

[30] K. G. Günther. Aufdampfschidhten aus halbleitenden III-V-Verbindungen. *Zeitschrift für Naturforschung A*, 13(12):1081–1089, dec 1958.

[31] John E. Davey and Titus Pankey. Epitaxial GaAs Films Deposited by Vacuum Evaporation. *Journal of Applied Physics*, 39(4):1941–1948, mar 1968.

[32] A.Y. Cho and J.R. Arthur. Molecular beam epitaxy. *Progress in Solid State Chemistry*, 10:157–191, jan 1975.

[33] G. Binnig, H. Rohrer, Ch. Gerber, and E. Weibel. Surface Studies by Scanning Tunneling Microscopy. *Physical Review Letters*, 49(1):57–61, jul 1982.

[34] J. Tersoff and D. R. Hamann. Theory of the scanning tunneling microscope. *Physical Review B*, 31(2):805–813, jan 1985.

[35] J. Bardeen. Tunnelling from a Many-Particle Point of View. *Physical Review Letters*, 6(2):57–59, jan 1961.

[36] J. E. Hoffman. Imaging Quasiparticle Interference in $Bi_2Sr_2CaCu_2O_{8+\delta}$. *Science*, 297(5584):1148–1151, aug 2002.

[37] P. G. DE GENNES. Boundary Effects in Superconductors. *Reviews of Modern Physics*, 36(1):225–237, jan 1964.

[38] Hao-Hua Sun, Kai-Wen Zhang, Lun-Hui Hu, Chuang Li, Guan-Yong Wang, Hai-Yang Ma, Zhu-An Xu, Chun-Lei Gao, Dan-Dan Guan, Yao-Yi Li, Canhua Liu, Dong Qian, Yi Zhou, Liang Fu, Shao-Chun Li, Fu-Chun Zhang, and Jin-Feng Jia. Majorana Zero Mode Detected with Spin Selective Andreev Reflection in the Vortex of a Topological Superconductor. *Physical Review Letters*, 116(25):257003, jun 2016.

[39] Yoichi Kamihara, Takumi Watanabe, Masahiro Hirano, and Hideo Hosono. Iron-Based Layered Superconductor $La[O_{1-x}F_x]FeAs$ (x = 0.05-0.12) with T_c = 26 K. *Journal of the American Chemical Society*, 130(11):3296–3297, mar 2008.

[40] G. R. Stewart. Superconductivity in iron compounds. *Reviews of Modern Physics*, 83(4):1589–1652, dec 2011.

[41] Jian-Feng Ge, Zhi-Long Liu, Canhua Liu, Chun-Lei Gao, Dong Qian, Qi-Kun Xue, Ying Liu, and Jin-Feng Jia. Superconductivity above 100 K in single-layer FeSe films on doped $SrTiO_3$. *Nature Materials*, 14(3):285–289, mar 2015.

[42] Wenhao Zhang, Zhi Li, Fangsen Li, Huimin Zhang, Junping Peng, Chenjia Tang, Qingyan Wang, Ke He, Xi Chen, Lili Wang, Xucun Ma, and Qi-Kun Xue. Interface charge doping effects on superconductivity of single-unit-cell FeSe films on $SrTiO_3$ substrates. *Physical Review B*, 89(6):060506, feb 2014.

[43] Yalin Zhang, Tong Wang, Zhihe Wang, and Zhongwen Xing. Effects of Te- and Fe-doping on the superconducting properties in $Fe_ySe_{1-x}Te_x$ thin films. *Scientific Reports*, 12(1):391, dec 2022.

[44] Fong-Chi Hsu, Jiu-Yong Luo, Kuo-Wei Yeh, Ta-Kun Chen, Tzu-Wen Huang, Phillip M. Wu, Yong-Chi Lee, Yi-Lin Huang, Yan-Yi Chu, Der-Chung Yan, and Maw-Kuen Wu. Supercon-

ductivity in the PbO-type structure α-FeSe. *Proceedings of the National Academy of Sciences*, 105(38):14262–14264, sep 2008.

[45] M. B. Babanly, E. V. Chulkov, Z. S. Aliev, A. V. Shevelkov, and I. R. Amiraslanov. Phase diagrams in materials science of topological insulators based on metal chalcogenides. *Russian Journal of Inorganic Chemistry*, 62(13):1703–1729, dec 2017.

[46] He Zhao, Bryan Rachmilowitz, Zheng Ren, Ruobin Han, J. Schneeloch, Ruidan Zhong, Genda Gu, Ziqiang Wang, and Ilija Zeljkovic. Superconducting proximity effect in a topological insulator using Fe(Te, Se). *Physical Review B*, 97(22):224504, jun 2018.

[47] Yao-Yi Li, Guang Wang, Xie-Gang Zhu, Min-Hao Liu, Cun Ye, Xi Chen, Ya-Yu Wang, Ke He, Li-Li Wang, Xu-Cun Ma, Hai-Jun Zhang, Xi Dai, Zhong Fang, Xin-Cheng Xie, Ying Liu, Xiao-Liang Qi, Jin-Feng Jia, Shou-Cheng Zhang, and Qi-Kun Xue. Intrinsic Topological Insulator Bi_2Te_3 Thin Films on Si and Their Thickness Limit. *Advanced Materials*, 22(36):4002–4007, sep 2010.

[48] Yoshinori Okada, Chetan Dhital, Wenwen Zhou, Erik D. Huemiller, Hsin Lin, S. Basak, A. Bansil, Y.-B. Huang, H. Ding, Z. Wang, Stephen D. Wilson, and V. Madhavan. Direct Observation of Broken Time-Reversal Symmetry on the Surface of a Magnetically Doped Topological Insulator. *Physical Review Letters*, 106(20):206805, may 2011.

[49] Paolo Sessi, Felix Reis, Thomas Bathon, Konstantin A. Kokh, Oleg E. Tereshchenko, and Matthias Bode. Signatures of Dirac fermion-mediated magnetic order. *Nature Communications*, 5(1):5349, dec 2014.

[50] Kyungmin Lee, Abolhassan Vaezi, Mark H. Fischer, and Eun-Ah Kim. Superconducting proximity effect in topological metals. *Physical Review B*, 90(21):214510, dec 2014.

[51] S. Manna, A. Kamlapure, L. Cornils, T. Hänke, E. M. J. Hedegaard, M. Bremholm, B. B. Iversen, Ph. Hofmann, J. Wiebe, and R. Wiesendanger. Interfacial superconductivity in a bi-collinear antiferromagnetically ordered FeTe monolayer on a topological insulator. *Nature Communications*, 8(1):14074, apr 2017.

[52] T Hanaguri, S Niitaka, K Kuroki, and H Takagi. Unconventional s -Wave Superconductivity in Fe(Se,Te). *Science*, 328(5977):474–476, apr 2010.

[53] Jin-Peng Xu, Canhua Liu, Mei-Xiao Wang, Jianfeng Ge, Zhi-Long Liu, Xiaojun Yang, Yan Chen, Ying Liu, Zhu-An Xu, Chun-Lei Gao, Dong Qian, Fu-Chun Zhang, and Jin-Feng Jia. Artificial Topological Superconductor by the Proximity Effect. *Physical Review Letters*, 112(21):217001, may 2014.

[54] H. F. Hess, R. B. Robinson, R. C. Dynes, J. M. Valles, and J. V. Waszczak. Scanning-Tunneling-Microscope Observation of the Abrikosov Flux Lattice and the Density of States near and inside a Fluxoid. *Physical Review Letters*, 62(2):214–216, jan 1989.

[55] J. L. Her, Y. Kohama, Y. H. Matsuda, K. Kindo, W-H Yang, D. A. Chareev, E. S. Mitrofanova, O. S. Volkova, A. N. Vasiliev, and J-Y Lin. Anisotropy in the upper critical field of FeSe and $FeSe_0.33Te_0.67$ single crystals. *Superconductor Science and Technology*, 28(4):045013, apr 2015.

[56] R. C. Dynes, J. P. Garno, G. B. Hertel, and T. P. Orlando. Tunneling Study of Superconductivity near the Metal-Insulator Transition. *Physical Review Letters*, 53(25):2437–2440, dec 1984.

[57] J-X. Yin, Zheng Wu, J-H. Wang, Z-Y. Ye, Jing Gong, X-Y. Hou, Lei Shan, Ang Li, X-J. Liang, X-X. Wu, Jian Li, C-S. Ting, Z-Q. Wang, J-P. Hu, P-H. Hor, H. Ding, and S. H. Pan. Observation of a robust zero-energy bound state in iron-based superconductor Fe(Te,Se). *Nature Physics*, 11(7):543–546, jul 2015.

[58] H. F. Hess, R. B. Robinson, and J. V. Waszczak. Vortex-core structure observed with a scanning tunneling microscope. *Physical Review Letters*, 64(22):2711–2714, may 1990.

[59] Dongfei Wang, Lingyuan Kong, Peng Fan, Hui Chen, Shiyu Zhu, Wenyao Liu, Lu Cao, Yujie Sun, Shixuan Du, John Schneeloch, Ruidan Zhong, Genda Gu, Liang Fu, Hong Ding, and Hongjun Gao. Evidence for Majorana bound states in an iron-based superconductor. *Science*, 362(6412):333–335, oct 2018.

[60] Liang Fu. Topological Crystalline Insulators. *Physical Review Letters*, 106(10):106802, mar 2011.

[61] P Dziawa, B J Kowalski, K Dybko, R Buczko, A Szczerbakow, M Szot, E Łusakowska, T Balasubramanian, B M Wojek, M H Berntsen, O Tjernberg, and T Story. Topological crystalline insulator states in $Pb_{1-x}Sn_xSe$. *Nature Materials*, 11(12):1023–7, dec 2012.

[62] B. M. Wojek, M. H. Berntsen, V. Jonsson, A. Szczerbakow, P. Dziawa, B. J. Kowalski, T. Story, and O. Tjernberg. Direct observation and temperature control of the surface Dirac gap in a topological crystalline insulator. *Nature Communications*, 6(May):8463, oct 2015.

[63] Su-Yang Xu, Chang Liu, N Alidoust, M Neupane, D Qian, I Belopolski, J.D. Denlinger, Y.J. Wang, H Lin, L.A. Wray, G Landolt, B Slomski, J.H. Dil, A Marcinkova, E Morosan, Q Gibson, R Sankar, F.C. Chou, R.J. Cava, A Bansil, and M.Z. Hasan. Observation of a topological crystalline insulator phase and topological phase transition in $Pb_{1-x}Sn_xTe$. *Nature Communications*, 3(1):1192, jan 2012.

[64] Ching Kai Chiu, Hong Yao, and Shinsei Ryu. Classification of topological insulators and superconductors in the presence of reflection symmetry. *Physical Review B - Condensed Matter and Materials Physics*, 88(7):1–24, 2013.

[65] Ken Shiozaki and Masatoshi Sato. Topology of crystalline insulators and superconductors. *Physical Review B*, 90(16):165114, oct 2014.

[66] Fan Zhang, C. L. Kane, and E. J. Mele. Topological Mirror Superconductivity. *Physical Review Letters*, 111(5):056403, aug 2013.

[67] Mingyang Chen, Xiaoyu Chen, Huan Yang, Zengyi Du, and Hai-Hu Wen. Superconductivity with twofold symmetry in $Bi_2Te_3/FeTe_0.55Se_0.45$ heterostructures. *Science Advances*, 4(6):eaat1084, jun 2018.

[68] R. D. Zhong, J. A. Schneeloch, X. Y. Shi, Z. J. Xu, C. Zhang, J. M. Tranquada, Q. Li, and G. D. Gu. Optimizing the superconducting transition temperature and upper critical field of $Sn_{1-x}In_xTe$. *Physical Review B*, 88(2):020505, jul 2013.

[69] Y. S. Hor, A. J. Williams, J. G. Checkelsky, P. Roushan, J. Seo, Q. Xu, H. W. Zandbergen, A. Yazdani, N. P. Ong, and R. J. Cava. Superconductivity in $Cu_xBi_2Se_3$ and its Implications for Pairing in the Undoped Topological Insulator. *Physical Review Letters*, 104(5):057001, feb 2010.

[70] C. M. Polley, V. Jovic, T-Y. Su, M. Saghir, D. Newby, B. J. Kowalski, R. Jakiela, A. Barcz, M. Guziewicz, T. Balasubramanian, G. Balakrishnan, J. Laverock, and K. E. Smith. Observation of surface states on heavily indium-doped SnTe(111), a superconducting topological crystalline insulator. *Physical Review B*, 93(7):075132, feb 2016.

[71] Weidong Si, Cheng Zhang, Lijun Wu, Toshinori Ozaki, Genda Gu, and Qiang Li. Superconducting thin films of (100) and (111) oriented indium doped topological crystalline insulator SnTe. *Applied Physics Letters*, 107(9):092601, aug 2015.

[72] Ruidan Zhong, Xugang He, J. A. Schneeloch, Cheng Zhang, Tiansheng Liu, I. Pletikosić, T. Yilmaz, B. Sinkovic, Qiang Li, Wei Ku, T. Valla, J. M. Tranquada, and Genda Gu. Surface-state-dominated transport in crystals of the topological crystalline insulator In-doped $Pb_{1-x}Sn_xTe$. *Physical Review B*, 91(19):195321, may 2015.

[73] Robin Klett, Joachim Schönle, Andreas Becker, Denis Dyck, Kiril Borisov, Karsten Rott, Daniela Ramermann, Björn Büker, Jan Haskenhoff, Jan Krieft, Torsten Hübner, Oliver Reimer, Chandra Shekhar, Jan-Michael Schmalhorst, Andreas Hütten, Claudia Felser, Wolfgang Wernsdorfer, and Günter Reiss. Proximity-Induced Superconductivity and Quantum Interference in Topological Crystalline Insulator SnTe Thin-Film Devices. *Nano Letters*, 18(2):1264–1268, feb 2018.

[74] B. A. Assaf, F. Katmis, P. Wei, B. Satpati, Z. Zhang, S. P. Bennett, V. G. Harris, J. S. Moodera, and D. Heiman. Quantum coherent transport in SnTe topological crystalline insulator thin films. *Applied Physics Letters*, 105(10):102108, sep 2014.

[75] Chenhui Yan, Junwei Liu, Yunyi Zang, Jianfeng Wang, Zhenyu Wang, Peng Wang, Zhi-Dong Zhang, Lili Wang, Xucun Ma, Shuaihua Ji, Ke He, Liang Fu, Wenhui Duan, Qi-Kun Xue, and Xi Chen. Experimental Observation of Dirac-like Surface States and Topological Phase Transition in $Pb_{1-x}Sn_xTe(111)$ Films. *Physical Review Letters*, 112(18):186801, may 2014.

[76] Qing Lin He, Hongchao Liu, Mingquan He, Ying Hoi Lai, Hongtao He, Gan Wang, Kam Tuen Law, Rolf Lortz, Jiannong Wang, and Iam Keong Sou. Two-dimensional superconductivity at the interface of a Bi_2Te_3/FeTe heterostructure. *Nature Communications*, 5(1):4247, sep 2014.

[77] G. Springholz and K. Wiesauer. Nanoscale Dislocation Patterning in PbTe/PbSe(001) Lattice-Mismatched Heteroepitaxy. *Physical Review Letters*, 88(1):015507, dec 2001.

[78] Daniel Walkup, Badih A. Assaf, Kane L. Scipioni, R. Sankar, Fangcheng Chou, Guoqing Chang, Hsin Lin, Ilija Zeljkovic, and Vidya Madhavan. Interplay of orbital effects and nanoscale strain in topological crystalline insulators. *Nature Communications*, 9(1):1550, dec 2018.

[79] Ilija Zeljkovic, Daniel Walkup, Badih A. Assaf, Kane L. Scipioni, R. Sankar, Fangcheng Chou, and Vidya Madhavan. Strain engineering Dirac surface states in heteroepitaxial topological crystalline insulator thin films. *Nature Nanotechnology*, 10(10):849–853, aug 2015.

[80] Nikesh Koirala, Matthew Brahlek, Maryam Salehi, Liang Wu, Jixia Dai, Justin Waugh, Thomas Nummy, Myung-Geun Han, Jisoo Moon, Yimei Zhu, Daniel Dessau, Weida Wu, N. Peter Armitage, and Seongshik Oh. Record Surface State Mobility and Quantum Hall Effect in Topological Insulator Thin Films via Interface Engineering. *Nano Letters*, 15(12):8245–8249, dec 2015.

[81] Y Tanaka, T Shoman, K Nakayama, S Souma, T Sato, T Takahashi, M Novak, Kouji Segawa, and Yoichi Ando. Two types of Dirac-cone surface states on the (111) surface of the topological crystalline insulator SnTe. *Physical Review B*, 88(23):235126, dec 2013.

[82] Junwei Liu and Liang Fu. Electrically tunable quantum spin Hall state in topological crystalline insulator thin films. *Physical Review B*, 91(8):081407, feb 2015.

[83] Jennifer E. Hoffman. Spectroscopic scanning tunneling microscopy insights into Fe-based superconductors. *Reports on Progress in Physics*, 74(12):124513, dec 2011.

[84] Yoshikazu Mizuguchi and Yoshihiko Takano. Review of Fe Chalcogenides as the Simplest Fe-Based Superconductor. *Journal of the Physical Society of Japan*, 79(10):102001, oct 2010.

[85] Yue Sun, Zhixiang Shi, and Tsuyoshi Tamegai. Review of annealing effects and superconductivity in $Fe_{1+y}Te_{1-x}Se_x$ superconductors. *Superconductor Science and Technology*, 32(10):103001, oct 2019.

[86] Dongfei Wang, Lingyuan Kong, Peng Fan, Hui Chen, Shiyu Zhu, Wenyao Liu, Lu Cao, Yujie Sun, Shixuan Du, John Schneeloch, Ruidan Zhong, Genda Gu, Liang Fu, Hong Ding, and Hong-Jun Gao. Evidence for Majorana bound states in an iron-based superconductor. *Science*, 362(6412):333–335, oct 2018.

[87] Natsumi Shimamura, Katsuaki Sugawara, Sukrit Sucharitakul, Seigo Souma, Katsuya Iwaya, Kosuke Nakayama, Chi Xuan Trang, Kunihiko Yamauchi, Tamio Oguchi, Kazutaka Kudo, Takashi Noji, Yoji Koike, Takashi Takahashi, Tetsuo Hanaguri, and Takafumi Sato. Ultrathin Bismuth Film on High-Temperature Cuprate Superconductor $Bi_2Sr_2CaCu_2O_{8+\delta}$ as a Candidate of a Topological Superconductor. *ACS Nano*, 12(11):10977–10983, nov 2018.

[88] Siyuan Wan, Qiangqiang Gu, Huazhou Li, Huan Yang, J. Schneeloch, R. D. Zhong, G. D. Gu, and Hai-Hu Wen. Twofold symmetry of proximity-induced superconductivity on $Bi_2Te_3/Bi_2Sr_2CaCu_2O_{8+\delta}$ heterostructures revealed by scanning tunneling microscopy. pages 1–10, dec 2019.

[89] J. G. Bednorz and K. A. Muller. Possible highT_c superconductivity in the Ba-La-Cu-O system. *Zeitschrift f r Physik B Condensed Matter*, 64(2):189–193, jun 1986.

[90] He Zhao, Zheng Ren, Bryan Rachmilowitz, John Schneeloch, Ruidan Zhong, Genda Gu, Ziqiang Wang, and Ilija Zeljkovic. Charge-stripe crystal phase in an insulating cuprate. *Nature Materials*, 18(2):103–107, feb 2019.

[91] Jungpil Seo, Pedram Roushan, Haim Beidenkopf, Y. S. Hor, R. J. Cava, and Ali Yazdani. Transmission of topological surface states through surface barriers. *Nature*, 466(7304):343–346, jul 2010.

[92] Siyuan Wan, Qiangqiang Gu, Huazhou Li, Huan Yang, J. Schneeloch, R. D. Zhong, G. D. Gu, and Hai-Hu Wen. Twofold symmetry of proximity-induced superconductivity in $Bi_2Te_3/Bi_2Te_3/Bi_2Sr_2CaCu_2O_{8+\delta}$ heterostructures revealed by scanning tunneling microscopy. *Physical Review B*, 101(22):220503, jun 2020.

[93] Igor Altfeder, Andrey A. Voevodin, Michael H. Check, Sarah M. Eichfeld, Joshua A. Robinson, and Alexander V. Balatsky. Scanning Tunneling Microscopy Observation of Phonon Condensate. *Scientific Reports*, 7(1):43214, dec 2017.

[94] D. Subramaniam, F. Libisch, Y. Li, C. Pauly, V. Geringer, R. Reiter, T. Mashoff, M. Liebmann, J. Burgdörfer, C. Busse, T. Michely, R. Mazzarello, M. Pratzer, and M. Morgenstern. Wave-Function Mapping of Graphene Quantum Dots with Soft Confinement. *Physical Review Letters*, 108(4):046801, jan 2012.

[95] Jonathan Reiner, Abhay Kumar Nayak, Amit Tulchinsky, Aviram Steinbok, Tom Koren, Noam Morali, Rajib Batabyal, Jung-Hyun Kang, Nurit Avraham, Yuval Oreg, Hadas Shtrikman, and Haim Beidenkopf. Spectroscopic Visualization of a Robust Electronic Response of Semiconducting Nanowires to Deposition of Superconducting Islands. pages 1–32, nov 2019.

[96] M. Amman, R. Wilkins, E. Ben-Jacob, P. D. Maker, and R. C. Jaklevic. Analytic solution for the current-voltage characteristic of two mesoscopic tunnel junctions coupled in series. *Physical Review B*, 43(1):1146–1149, jan 1991.

[97] P. Delsing, K. K. Likharev, L. S. Kuzmin, and T. Claeson. Effect of high-frequency electrodynamic environment on the single-electron tunneling in ultrasmall junctions. *Physical Review Letters*, 63(11):1180–1183, sep 1989.

[98] M. H. Devoret, D. Esteve, H Grabert, G.-L. Ingold, H. Pothier, and C. Urbina. Effect of the electromagnetic environment on the Coulomb blockade in ultrasmall tunnel junctions. *Physical Review Letters*, 64(15):1824–1827, apr 1990.

[99] Christophe Brun, Konrad H. Müller, I-Po Hong, François Patthey, Christian Flindt, and Wolf-Dieter Schneider. Dynamical Coulomb Blockade Observed in Nanosized Electrical Contacts. *Physical Review Letters*, 108(12):126802, mar 2012.

[100] I-Po Hong, Christophe Brun, Marina Pivetta, François Patthey, and Wolf-Dieter Schneider. Coulomb blockade phenomena observed in supported metallic nanoislands. *Frontiers in Physics*, 1(September):1–8, 2013.

[101] L. Serrier-Garcia, J. C. Cuevas, T. Cren, C. Brun, V. Cherkez, F. Debontridder, D. Fokin, F. S. Bergeret, and D. Roditchev. Scanning Tunneling Spectroscopy Study of the Proximity Effect in a Disordered Two-Dimensional Metal. *Physical Review Letters*, 110(15):157003, apr 2013.

[102] S. M. Girvin, L. I. Glazman, M. Jonson, D. R. Penn, and M. D. Stiles. Quantum fluctuations and the single-junction Coulomb blockade. *Physical Review Letters*, 64(26):3183–3186, jun 1990.

[103] Gert-Ludwig Ingold and Yu. V. Nazarov. Charge Tunneling Rates in Ultrasmall Junctions. pages 21–107. 1992.

[104] P. Joyez, V. Bouchiat, D. Esteve, C. Urbina, and M. H. Devoret. Strong Tunneling in the Single-Electron Transistor. *Physical Review Letters*, 79(7):1349–1352, aug 1997.